Chapter 2 Planar Oblique Fin Microchannel Structure

Keywords Planar oblique fin microchannel • Boundary layer • Secondary flow • Heat transfer • Pressure drop • Hotspot mitigation

2.1 Oblique Fin Concept and Motivations

In order to generate secondary flow in the conventional-sized passage, the louvred fin heat exchanger has the entire slit fins rotated 20°–45° relative to the airflow direction. On the other hand, Steinke and Kandlikar [1] suggested placing the smaller secondary channels at an angle between the main channels for microchannel application. The graphic representation of both concepts is illustrated in Figs. 2.1 and 2.2, respectively.

Both fin layouts share the same characteristics, where the secondary flow paths are rotated at an angle relative to the main flow paths, and these unique characteristics are adopted into the current microchannel heat sink design. The current heat sink design adopts sectional oblique fins to replace the conventional continuous fins in microchannel heat sink application [3]. Figure 2.3 illustrates the plan view of the proposed microchannel configuration along with the flow paths for the main flows and secondary flows.

In this design, oblique cuts are made along the fins to create smaller, branching secondary channels (named as oblique channel) with the intentions to (1) disrupt the thermal boundary layer development and (2) generate secondary flows. The current design would follow the recommendation by Suga and Aoki [4] that the ratio of fin pitch in the spanwise direction to the fin length has to be 1.5 times the tangent of oblique angle $(F_p/L_p=1.5\times \tan\theta)$ as shown in Fig. 2.1) to provide a good balance between heat transfer and pressure drop. The oblique angle that denotes the angle between the main channel and oblique channel is set as ~27°, which is within the range of louvre angles $(20^{\circ}-45^{\circ})$ that are frequently evaluated in the literatures. Instead of emulating the design by Steinke and Kandlikar [1], where the direction of secondary channels is alternated in the streamwise direction, the direction oblique channel remains consistent throughout the heat sink, following the louvred fin design. The concept of turnaround louvre is, however, not incorporated.

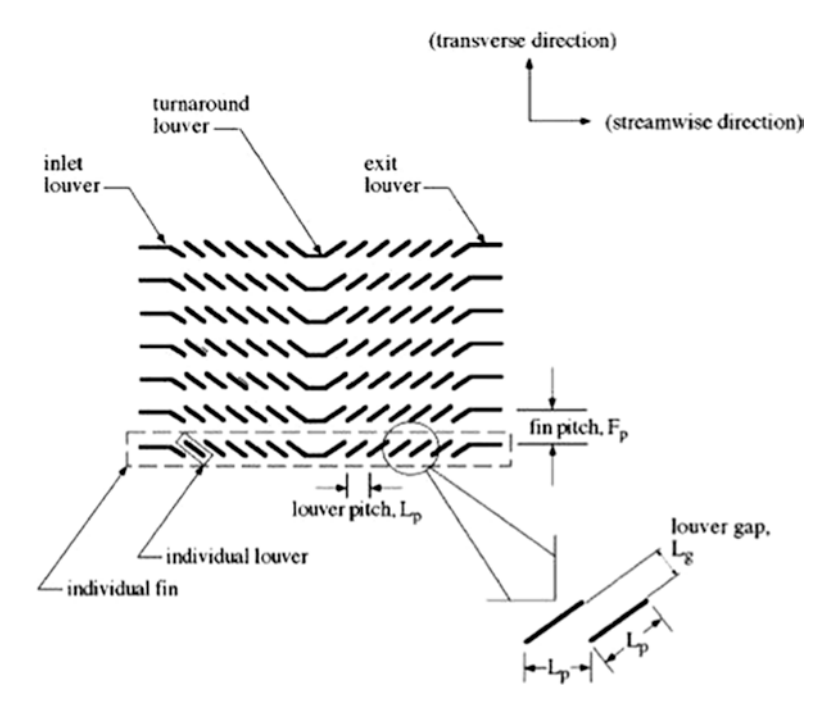


Fig. 2.1 Schematic of louvred fin arrays [2]

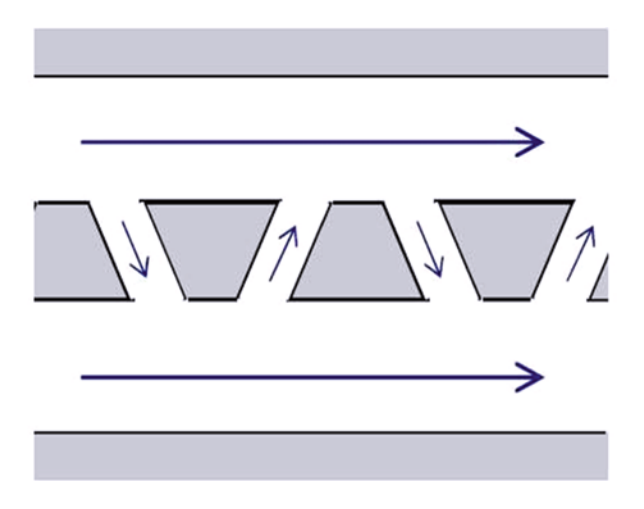


Fig. 2.2 Proposal by Steinke and Kandlikar to generate secondary flows [1]

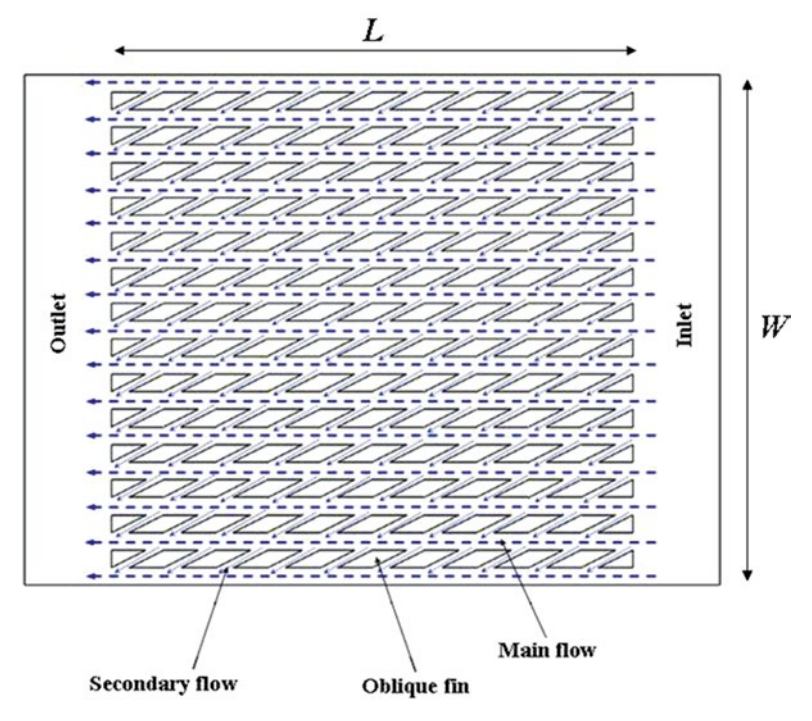


Fig. 2.3 Plan view of microchannel heat sink with oblique fins (not drawn to scale) (3D view) [3]

The width ratio of main channel to oblique channel is kept as 2:1, with the intention to reduce the amount of flow through secondary channel.

Although the current oblique fin design bears some resemblance to the louvred fin heat exchangers in the layout, the flow pattern in the enhanced microchannel with oblique fin array is designed to be different. Except at very low Reynolds number, the main flow within louvred fin arrays is nearly parallel to the louvres [5] and can be approximated as boundary layer flow, for which the Pohlhausen solution as flow over flat plate is applicable [6]. On the other hand, for the oblique fin array, the bulk of the flow remains in the main channel with only a small fraction of flow branching into the oblique openings (channels) and subsequently injected into the adjacent main channel, leading to generation of secondary flows which promote fluid mixing. For the sake of convenience and clarity, the microchannel with oblique fins in this chapter is addressed as enhanced microchannel.

2.2 Numerical Analysis: Simplified Model

The geometries for both the enhanced microchannel and conventional microchannel used in the simulation study are tabulated in Table 2.1. In order to facilitate a fair performance comparison, both heat sinks share the same channel aspect ratio, channel

Characteristic	Conventional microchannel	Enhanced microchannel
Material	Copper	
Footprint, width×length (mm)	25×25	
Main channel width, w_{ch} (µm)	500	
Fin width, w_w (μ m)	500	
Channel depth, $H(\mu m)$	1,500	
Aspect ratio, α	3	
Number of fin row, n	22	
Number of fin per row	_	12
Oblique channel width, w_{ob} (μ m)	_	250
Fin pitch, p (μm)	_	2,000
Fin length, l (μm)	_	1,450
Oblique angel, θ (°)	_	27

Table 2.1 Dimensional details for microchannel heat sinks for simulation [3]

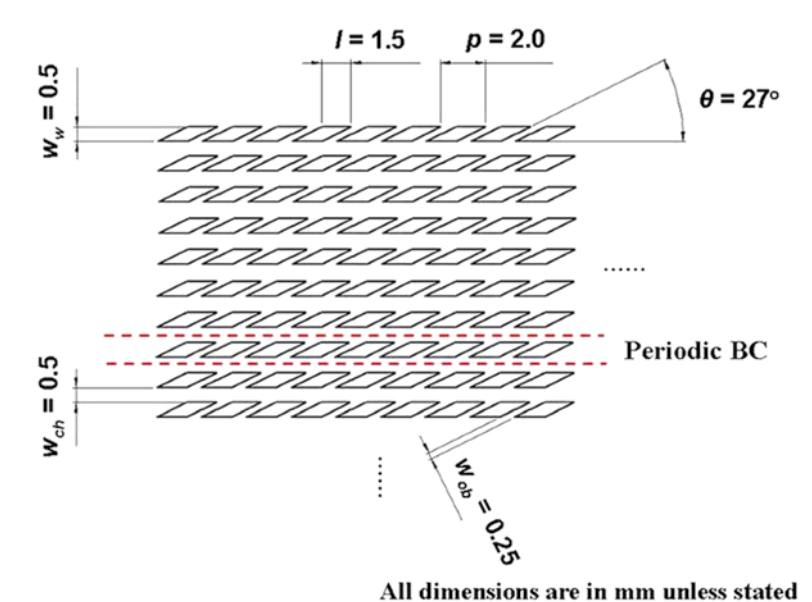


Fig. 2.4 Plan view of oblique fins with dimensions [3]

width, fin width and overall footprint. Apart from these common characteristics, the enhanced microchannel has openings that are obliquely cut at 27° from the main channel, at the pitch of 2 mm, with an oblique channel width of $250 \, \mu m$. The dimensions for the enhanced microchannel are shown in Fig. 2.4.

2.2.1 CFD Simulation Approach

Both simulation domains for enhanced microchannel and conventional microchannel are generated using GAMBIT v2.3. As evident from Fig. 2.4, the oblique fin structure exhibits spanwise periodicity if the edge effect is neglected. Thus, periodic boundary condition is assumed to reduce the computation domain to a channel-fin pair consisting of full width oblique fins and associated oblique channels in the middle and two half-width main channels at the sides. The flow at a periodic boundary is treated as though the opposite periodic plane is a direct neighbour to the cells adjacent to the first periodic boundary. Thus, when calculating the flow through the periodic boundary adjacent to a fluid cell, the flow conditions at the fluid cell adjacent to the opposite periodic plane are used [7]. The enlarged view of the computational domain for enhanced microchannel is showed in Fig. 2.5.

The top surface of the fins and channels are first meshed with quad-pave scheme, with a 25 μ m spacing spanwise and 25 μ m spacing streamwise. The volume mesh for the main channel, oblique fins and oblique channels are then generated with hex/wedge–cooper scheme with 25 μ m spacing in longitudinal direction. The volume for bottom substrate (heater) is subsequently created with hex/wedge–cooper scheme with 25 μ m spacing in longitudinal direction tracing the surface meshes from main channel, oblique fins and oblique channels at the interface. A total of 2,398,560 hexahedral cells are generated for the computational domain.

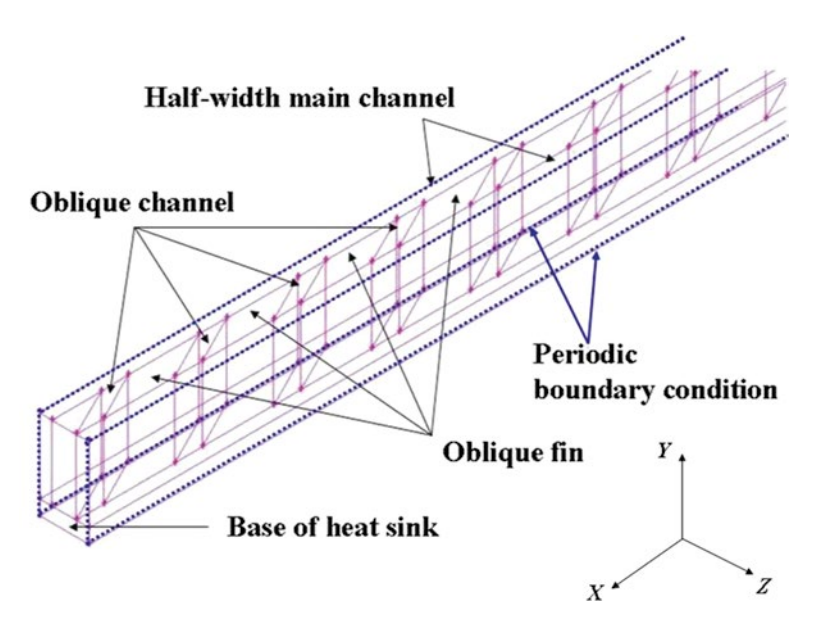


Fig. 2.5 Enlarged view of the computation domain for microchannel with oblique fins [3]

On the other hand, symmetry boundary condition is adopted at the centre of fin and channel for the conventional microchannel heat sink configuration, following the commonly used simplified boundary condition in the literature [8–10]. The symmetry boundary condition assumes that there is no fluid flow and heat transfer across the boundary surface. This effectively reduces the simulation domain to a half channel fin pair. The microchannel edges are then meshed by a 10 μm (spanwise)×20 μm (longitudinal)×50 μm (streamwise) spacing (50×90×500 cells). Both the fluid and solid regions are meshed with hex-map and hex-submap scheme, respectively, and a total of 2,250,000 hexahedral cells are generated.

The simulations are executed with the general purpose commercial CFD software, FLUENT v6.3, which solves the four governing equations numerically. These governing equations consist of continuity equation, momentum equation, energy equation for liquid and energy equation for solid listed as follows:

$$\nabla \cdot (\rho \vec{\mathbf{v}}) = 0 \tag{2.1}$$

$$\nabla \cdot (\rho \vec{v} \vec{v}) = -\nabla P + \nabla \cdot (\mu \nabla \vec{v})$$
 (2.2)

$$\nabla \cdot \left(\rho \vec{v} c_p T \right) = \nabla \cdot \left(k \nabla T \right) \tag{2.3}$$

$$\nabla \cdot (k \nabla T) = 0 \tag{2.4}$$

Upon exporting the mesh files to FLUENT, the 3D double-precision pressure-based solver is selected with standard SIMPLE algorithm as its pressure-velocity coupling method. Standard discretization scheme is used for the pressure equation, while second-order upwind discretization scheme is selected for both momentum and energy equations. Water liquid ($H_2O < I>$) is chosen as the working fluid, while copper (Cu) with constant thermal conductivity, k_{cu} =387.6 W/mK, is selected as fins and heat sink material. The density, specific heat capacity, thermal conductivity and dynamic viscosity of water are evaluated at the mean fluid temperature (average of the fluid inlet and outlet temperatures) using the following formulas [11]:

Density,

$$\rho(T) = \frac{a_0 + a_1 T + a_2 T^2 + a_3 T^3 + a_4 T^4 + a_5 T^5}{1 + bT}$$
 (2.5)

where

a_0 =999.8396	$a_4 = 1.49756 \times 10^{-7}$
$a_1 = 18.22494$	$a_5 = -3.93295 \times 10^{-10}$
$a_2 = -7.92221 \times 10^{-3}$	$b = 1.81597 \times 10^{-2}$
$a_3 = -5.54485 \times 10^{-5}$	T has the unit of °C

Specific heat capacity,

$$c_p(T) = 8,958.9 - 40.535T + 0.11243T^2 - 1.0138 \times 10^{-4}T^3$$
 (2.6)

Thermal conductivity,

$$k(T) = -0.58166 + 6.3555 \times 10^{-3} T - 7.9643 \times 10^{-6} T^{2}$$
 (2.7)

Dynamic viscosity,

$$\mu(T) = 2.414 \times 10^{-5} \times 10^{\left(\frac{247.8}{T - 140}\right)}$$
 (2.8)

For the calculation of specific heat capacity, thermal conductivity and dynamic viscosity, the temperature, T, should have unit of Kelvin (K). A residual of 10^{-6} is set as the convergence criterion for the continuity equation, x-velocity, y-velocity and z-velocity, while that for the energy equation is set as 10^{-9} .

The global coordinate system is defined such that X is in the axial direction (channel length), Y is in the longitudinal direction (channel depth) and Z is in the transverse direction (channel width). The local heat flux and local temperature distributions can be obtained from numerical simulations. With these quantities, the local convective coefficient, h(X), can be calculated using the following equation:

$$h(X) = \frac{1}{A(X)} \frac{q(X)}{T_w(X) - T_f(X)} \tag{2.9}$$

where A(X) and q(X) are the total local heat transfer area and total local heat input, respectively, defined as follows:

$$A(X) = \sum_{Y,Z} dA(X,Y,Z)$$
 (2.10)

$$q(X) = \sum_{Y,Z} q''(X,Y,Z) dA(X,Y,Z)$$
 (2.11)

 $T_w(X)$ and $T_f(X)$ on the other hand are local wall temperature and local fluid bulk-mean temperature given by

$$T_{w}(X) = \frac{\sum_{Y,Z} T_{w}(X, Y, Z) dA(X, Y, Z)}{\sum_{Y,Z} dA(X, Y, Z)}$$
(2.12)

$$T_{f}(X) = T_{f,\text{in}} + \frac{1}{\dot{m}C_{p}} \sum_{X,Y,Z} q''(X,Y,Z) dA(X,Y,Z)$$
 (2.13)

As for the enhanced microchannel heat sink, it is difficult to compute for the actual local heat transfer coefficient due to the discontinuity between fins. Thus, the computational domain is axially divided into small control volumes, and the heat transfer coefficient is computed as a local average. Adopting the formulas mentioned above, A(X), q(X) and $T_w(X)$ are the total heat transfer area, total heat input and area-weighted average channel wall temperature of the control volume. Fluid bulk-mean temperature of the control volume is calculated as

$$T_{f,ob}(X) = \frac{1}{2}(T_{f,in} + T_{f,out})$$
 (2.14)

where $T_{f,\text{in}}$ and $T_{f,\text{out}}$ are the bulk fluid temperature at the inlet and outlet of the control volume. The average Nusselt number for the microchannels can then be computed as the axially weighted average values of Nu(X) by

$$Nu_{\text{ave}} = \frac{\sum Nu(X)dL}{L} \tag{2.15}$$

For both cases considered, a fully developed velocity profile is assigned to the inlets following the finding by Lee et al. [12] that flow in microchannels is mostly thermally developing. An average velocity of 0.3 m/s is set at the entrance of the microchannel, which corresponds to 13.5 mL/min volumetric flow rate through one single channel, while the total volumetric flow rate through the heat sink is 311 mL/min. The resultant Reynolds number, Re, in the main channels (conventional and enhanced microchannel) is at 273. Pressure outlet boundary condition is assigned to the outlets, where the flow is assumed to reach atmospheric pressure at the outlet of the microchannels. A uniform heat flux of 65 W/cm² is supplied from the bottom of the substrates, while the top surface of the copper microchannel is assumed bonded with adiabatic cover for sealing purposes.

The meshes used in both the simulation studies for conventional and enhanced microchannel heat sinks are verified to result in grid-independent results. The resultant average Nusselt numbers from different meshes used are in close proximity to each other. For instance, average Nusselt numbers of 6.89, 6.88 and 6.88 were obtained with the mesh counts of $34\times60\times333$ cells, $50\times90\times500$ cells and $66\times120\times625$ cells, respectively, for the case of conventional microchannel. The average Nusselt number varies by 0.15 % from the first to the second mesh and only by 0.08 % upon further refinement to the finest grid. Thus, the intermediate grid $(50\times90\times500$ cells) was selected. On the other hand, average Nusselt numbers of 12.25, 11.93 and 11.84 were achieved with the mesh count of $25\times45\times625$ cells, $40\times72\times1,000$ cells and $50\times90\times1,250$ cells, respectively, for the case of enhanced microchannel. The variations in average Nusselt numbers are 2.61 % from the first to the second mesh and 0.75 % from second to the finest grid. Likewise, the intermediate grid $(40\times72\times1,000$ cells) was selected for enhanced microchannel.

2.2.2 Fluid Flow and Heat Transfer Characteristics

Simulations showed clear distinctions between the flow fields of conventional and enhanced microchannel. Figure 2.6a illustrates the mid-depth plane (Y=0.00075 m, Y'=0.5) velocity profile of water in the microchannels at X=0.0125 m (X'=0.5). Conventional microchannel shows consistent velocity contour throughout the channel with high velocity gradient from the channel wall to the fluid core. The consistent and parabolic velocity contour suggests that the hydrodynamic boundary layer is fully developed and merged at the centre of the channel.

On the other hand, the breakage of the continuous fin into sectional oblique fins disrupts the velocity profile and thus the hydrodynamic boundary layer development at the trailing edge of each oblique fin section. The discontinuity with the downstream fin causes the hydrodynamic boundary layer development to restart at the leading edge of the next downstream fin. In addition, the oblique fin is much shorter, which limits the development of boundary layer when compared to the long continuous fin of the conventional microchannel. Thus, the velocity profile is renewed each time the coolant flows passes an oblique fin. In addition, the introduction of oblique channels diverts a fraction of coolant from the main channel into it.

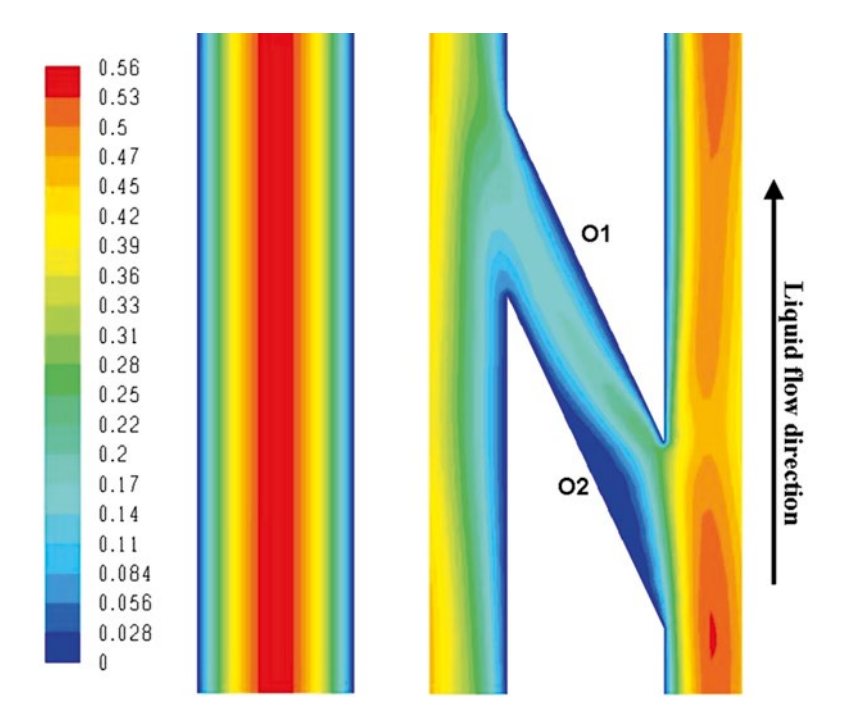


Fig. 2.6 Velocity contour (in m/s) of flow inside (a) conventional microchannel; (b) enhanced microchannel heat sinks at X' = 0.5 and Y' = 0.5 [3]

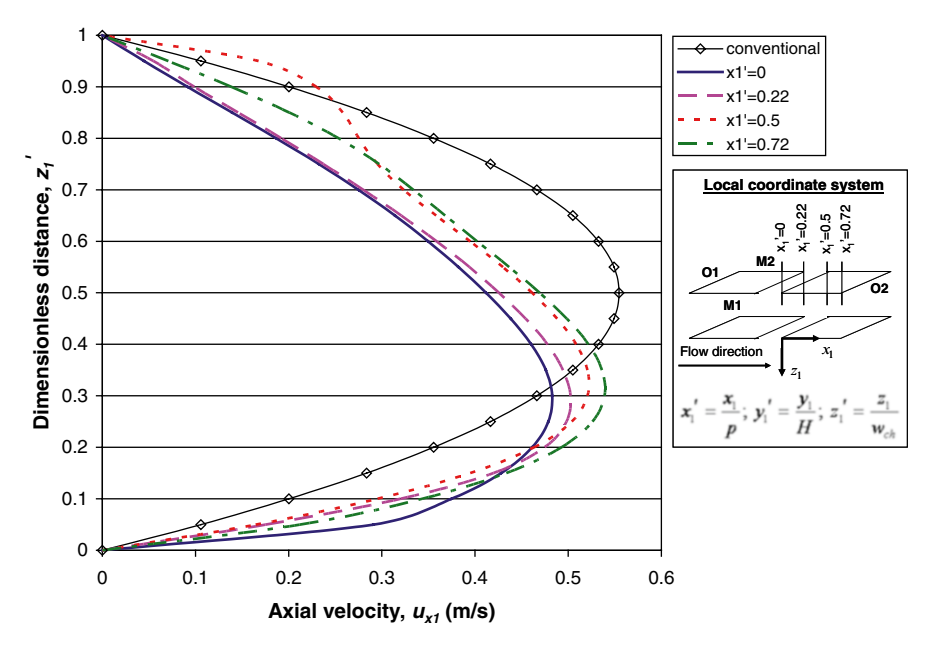


Fig. 2.7 Axial velocity profiles (in m/s) at the mid-depth plane of microchannel heat sinks at X' = 0.5 and Y' = 0.5 [3]

Owing to the axial flow momentum, the secondary flow created is brought closer to fin surface **O1**, as evident from the contour plot in Fig. 2.6b. The axial velocity profiles in Fig. 2.7, which are taken at the same position as in Fig. 2.6, reconfirm the thinning of boundary layer.

A local coordinate system is defined for the enhanced microchannel, originating from the tip of the oblique fin with x_1 lying along the main channel and z_1 in the transverse direction. Fin surfaces are also named specifically (M1, M2, O1 and O2). Uniquely skewed and asymmetrical velocity profile emerges in the main channel owing to the discontinuity between sectional fins and the asymmetry oblique channel arrangement. These axial velocity profiles of the enhanced microchannel skew towards fin surface M1 at $z_1'=0$ in the main channel compared to the fully developed velocity profile of conventional microchannel, which is symmetry at the centre line ($z_1'=0.5$). Consequently, the oblique fin surfaces M1 at $z_1'=0$ plane will have thinner boundary layer even though the average velocity in the main channel is lower compared to conventional microchannel. On the other hand, the oblique fin surfaces M2 on $z_1'=1$ plane have thicker hydrodynamic boundary layer.

As liquid coolant flows downstream to $x_1' = 0.22$, hydrodynamic boundary layer grows thicker at $z_1' = 0$ plane (fin surface M1), where velocity profile shifts upward towards the centre line, creating a more pointed profile. Between $x_1' = 0.22$ and $x_1' = 0.5$, the main channel receives additional liquid coolant (secondary flow) which is converging from the upstream oblique channel at $z_1' = 1$. Thus, the coolant veocity

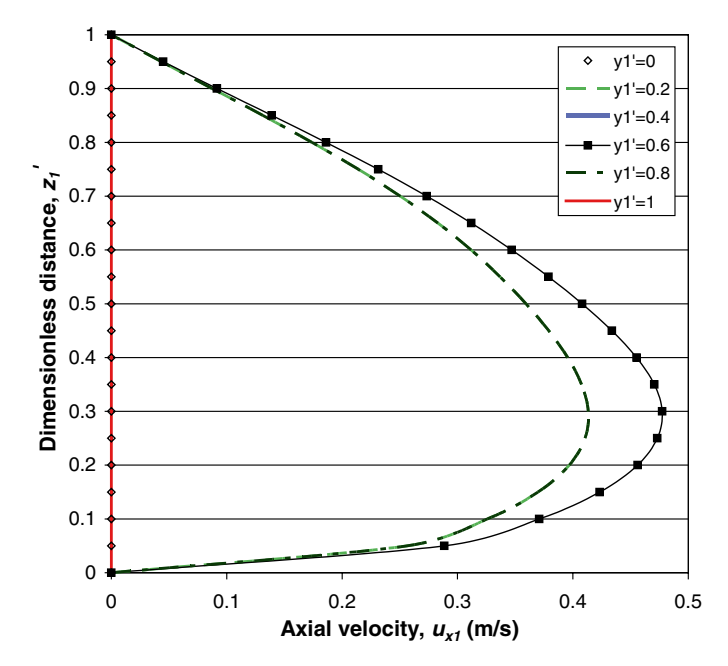


Fig. 2.8 Variation of velocity profiles (in m/s) in the longitudinal direction, y1' [3]

in the main channel for $x_1' = 0.5$ increases, especially in the region between $z_1' = 0.8$ and $z_1' = 1$, thinning the hydrodynamic boundary layer thickness at $z_1' = 1$ plane (fin surface M2) significantly, while boundary layer continues to grow at $z_1' = 0$ (fine surface M1). Subsequently, the coolant from oblique channel merges into the main channel flow smoothly leading to a skewed parabolic velocity profile as liquid coolant approaches $x_1' = 0.72$. A glance at the variation of velocity profile along the longitudinal direction, y_1' , in Fig. 2.8 shows that the velocity profiles are quite consistent where velocity is highest at the centre of the channel and slows down as it approaches the channel walls at $z_1' = 0$, $z_1' = 1$, $y_1' = 0$ and $y_1' = 1$.

Figure 2.9 continues to demonstrate the development of velocity profile along the fin. At $x_1' = 0.72$, coolant flow in the main channel encounters a diverging oblique channel at $z_1' = 0$. The presence of the smaller oblique channel induces a small fraction of the liquid in main channel into it and creates secondary flow. In this diagram, $z_1' > 0$ denotes main channel region and $z_1' < 0$ represents region in oblique channel. At $x_1' = 0.88$, coolant flows into the diffusive oblique channel at $z_1' < 0$ and shifts the velocity profile towards $z_1' < 0$. As a result of secondary flow generation, coolant velocity in the main channel decreases while coolant velocity in the oblique channel increases. In addition, liquid coolant in the diffusive oblique channel encounters adverse pressure gradient due to the sharp increase in flow area. The flow near the oblique fin surface **O2** no longer has energy to move into the higher-pressure region that is imposed by the decrease in velocity at the edge of the boundary layer [13], causing slight boundary layer separation or flow reversal in oblique channel.

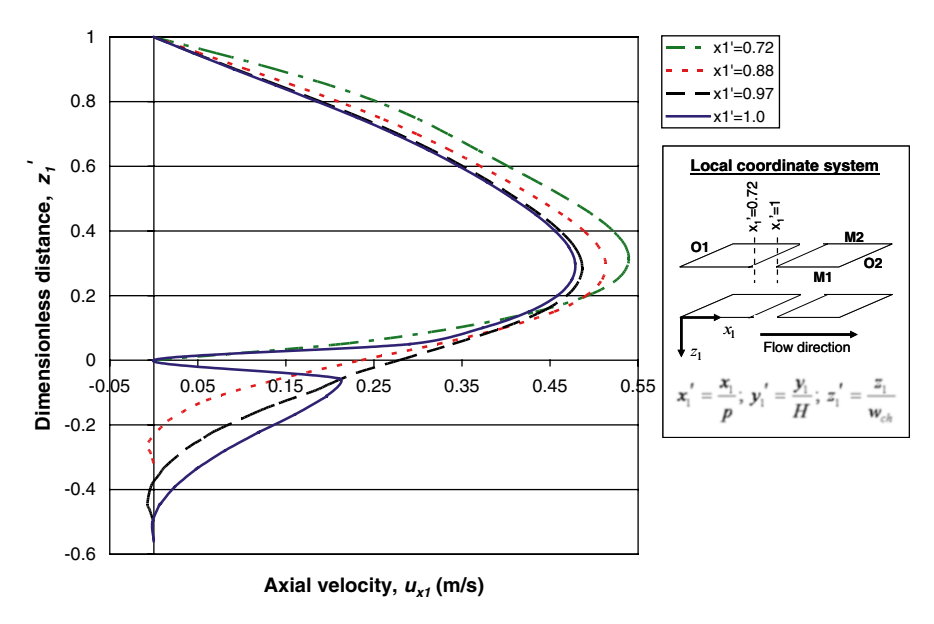


Fig. 2.9 Development of velocity profiles (in m/s) along the oblique fin [3]

Further downstream at $x_1' = 0.97$, velocity profile assumes a relatively symmetry parabolic curve at $z_1' = 0.3$ as coolant flows further into the oblique channel. Along with the secondary flow generation process, fluid particles with higher momentum are brought closer to fin surface M1 at $z_1'=0$ in the main channel. Finally as coolant reaches $x_1'=1$ (or $x_1'=0$ for downstream fin), shear stress halts the fluid particles that are in contact with the tip of downstream oblique fin at $z_1'=0$ (intersection of fin surface M1 and O1). However, liquid particles in the adjacent layers continue to flow with high velocity and create a skewed asymmetrical velocity profile with high near-wall velocity gradient in both main channel and oblique channel for fin surfaces M1 and O1 at $z_1' = 0$. It is observed that the velocity profile at $x_1' = 1$ (downstream of oblique fin) matches the velocity profile at $x_1'=0$ (upstream of oblique fin) very well, and this indicates that the velocity profile and boundary layer development is reinitiated as the coolant travels passed the oblique fins. Also, hydrodynamic boundary layer thickness at fin surface M1 at $z_1' = 0$ is consistently thinner than that of the conventional microchannel heat sink throughout the streamwise positions examined. Although fin surface M2 at $z_1' = 1$ displayed the opposite trend, its boundary layer thickness is significantly thinned down when surface M2 at $z_1' = 1$ receives the secondary flow injection from oblique channel at $x_1' = 0.5$. The effect from this series of velocity profile and boundary layer development on the overall heat transfer characteristic is discussed in the next section.

It is worth mentioning that the fluid flow characteristics of the current microchannel heat sink design are found to bear some similarities to that of fractal-shaped branching channel network. In the simulation results by Alharbi et al. [14], asymmetrical velocity profiles were present due to the asymmetric bifurcating angle in their

fractal-shaped microchannel. Besides, hydrodynamic boundary layer redevelopment after a bifurcation and slight flow reversal in the bifurcations were also noticed by Alharbi et al. [14] and Senn and Poulikakos [15].

The unique oblique fin design modulates the flow and creates a constantly renewed and developing flow field that is highly desirable for heat transfer applications. Periodically reinitialized hydrodynamic boundary layers coupled with the short section of fins would lead to thinner hydrodynamic boundary layers, where similar development could be predicted for the thermal boundary layer. The renewed thermal boundary layer at each oblique fin section is thinner than that of the conventional continuous fin which thickens continuously from the inlet to the outlet. Besides generating secondary flows, the oblique cuts (channels) that are laid along the main channels increase the convective heat transfer surface area for the enhanced microchannel heat sink. This supplementary heat transfer area at the base (unfinned area) and fin area in the oblique channels provides an additional ~25 % heat transfer area in comparison with the conventional microchannel. The secondary flows that travel along the oblique channel would promote additional heat dissipation from the oblique surfaces of the fins.

Figure 2.10a displays the significant water temperature difference from the fluid core to the channel wall, ranging from 20 to 63 °C for the case of conventional microchannel.

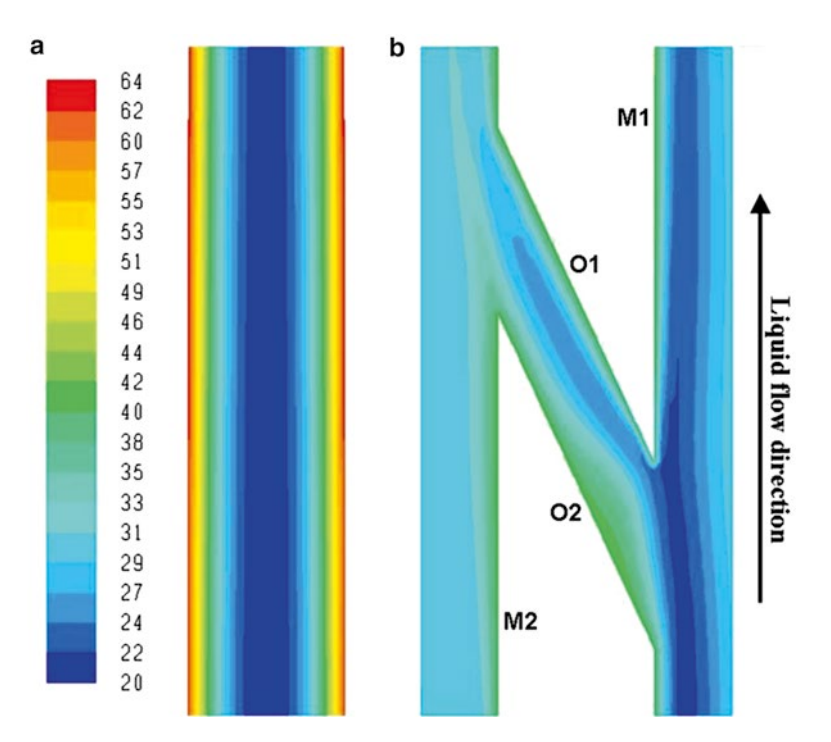


Fig. 2.10 Temperature contour (in °C) of flow inside (a) conventional microchannel; (b) enhanced microchannel heat sinks at X' = 0.5 and Y' = 0.5 [3]

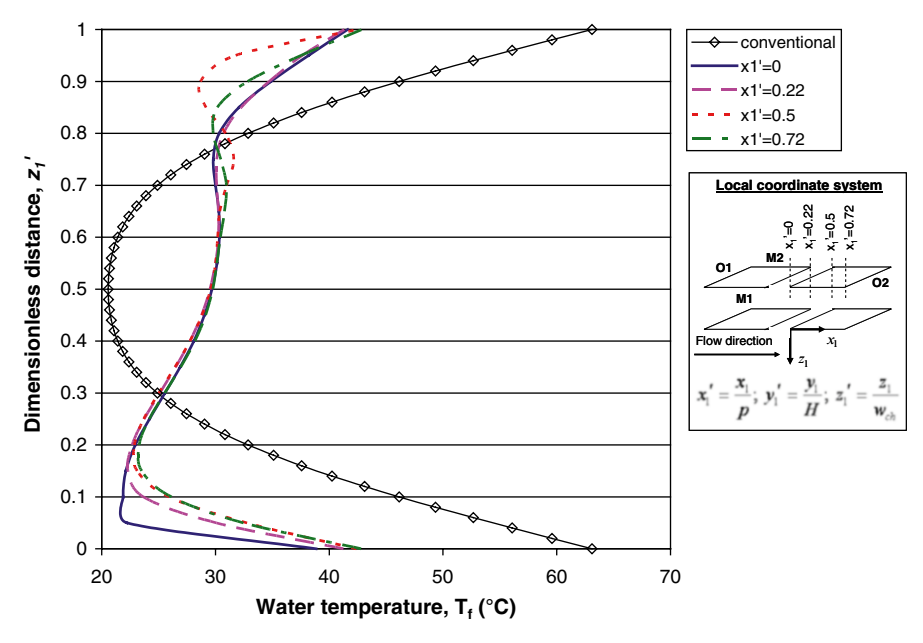


Fig. 2.11 Water temperature profile (in $^{\circ}$ C) at the mid-depth plane of microchannel heat sinks at X' = 0.5 and Y' = 0.5 [3]

As convection occurs, heat that is conducted from the channel wall into fluid particles at the wall propagates further into the fluid core through energy exchange with the adjoining fluid layer, causing the temperature gradients to develop in the fluid and thermal boundary layer to grow as coolant flows downstream. Continuous thickening of thermal boundary layer could lead to the deterioration of convective heat transfer and a further increase in wall temperature. In contrast, temperature contour of the coolant flow in the enhanced microchannel in Fig. 2.10b shows more uniform fluid temperature distribution in between 21 and 43 °C, as a result of better fluid mixing.

The water temperature profiles for both microchannel heat sinks are then compared in Fig. 2.11. Aligning with the skewed and asymmetrical velocity profile and the temperature contour showed previously, the temperature profiles of enhanced microchannel skew sharply to fin surface M1 at $z_1'=0$ planes. Comparing with the conventional microchannel, this fin surface M1 has much thinner thermal boundary layer with larger near-wall fluid temperature gradient. Thus, the combination of the entrance and secondary flow effects results in superior heat transfer performance, leading to lower wall temperature. Unlike Chandratilleke et al. [16] who employed high-frequency oscillating diaphragm that generates liquid jet to break up boundary layers and creates a steep temperature gradient, the current heat sink design achieved the similar feature through simple oblique fin design and does not require external power source.

Figure 2.11 also displays the development of temperature profiles along the fin. While the thermal boundary layer grows thicker along the fin with the near-wall fluid temperature gradients between water and channel walls are reducing, the injection of secondary flow into the main channel at $x_1' = 0.5$ at $z_1' = 1$ plane results in an opposite trend. The near-wall temperature gradient of fin surface M2 at $z_1'=1$ is observed to increase significantly as compared with the upstream position due to the coolant injection. Such thermal boundary layer thinning would improve the heat transfer performance for the fin surface M2 at the $z_1'=1$. As a result of secondary flow generation that promotes better fluid mixing, the water temperature profile of the enhanced microchannel is relatively flat compared with the parabolic curve of conventional microchannel. More importantly, the maximum fluid temperature and the range of fluid temperature in the enhanced microchannel are much smaller than those in the conventional microchannel, although both would share the same mass-weighted average temperature. For instance, water temperature adjacent to the fin surface of conventional microchannel can be as high as 63 °C while that of enhanced microchannel is drastically reduced to 43 °C. This demonstrates the importance of having well-mixed fluid, where the fin surface temperature can be lowered down substantially.

Figure 2.12 on the other hand shows the development in temperature profiles as coolant starts to diverge into oblique channel. The prominent finding from Fig. 2.12 is the emergence of the highly skewed temperature profiles for both fin surfaces M1 and O1 at $z_1' = 0$ as coolant reaches the next fin tip, which is aligned with the observation in the velocity profiles. The renewal of temperature profiles at $x_1' = 1$, recreating the significantly high temperature gradients or thinner thermal boundary layers

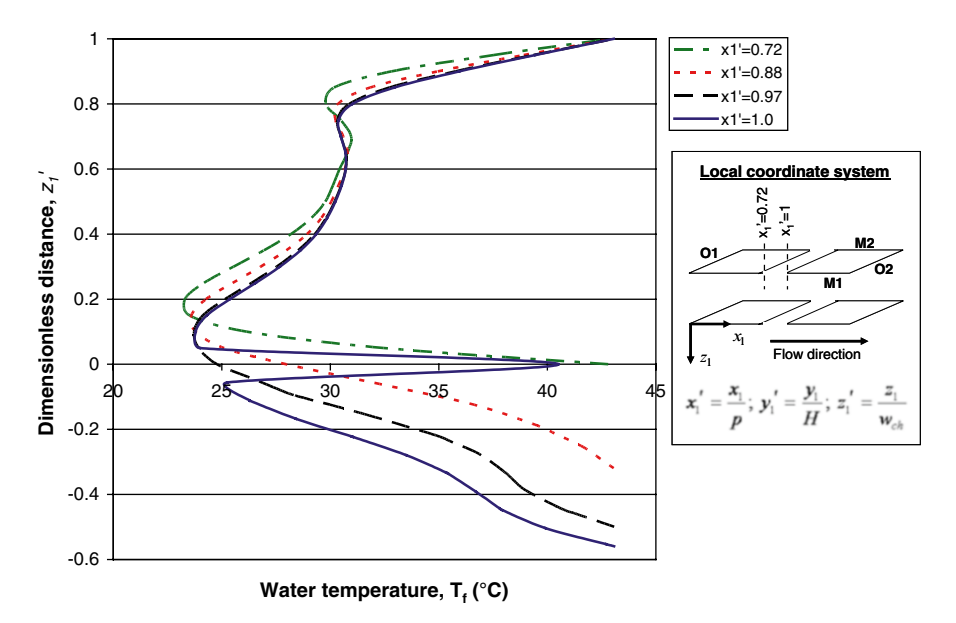


Fig. 2.12 Development of water temperature profile (in °C) along the oblique fin [3]

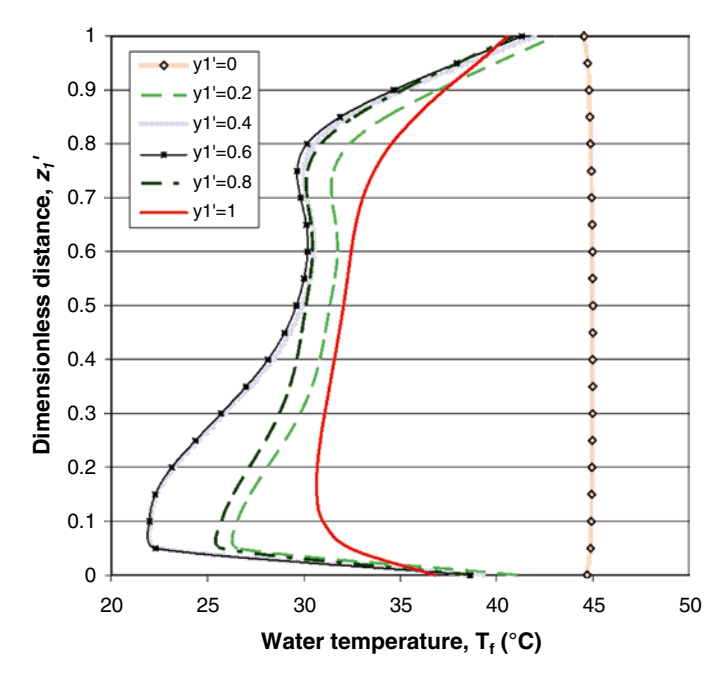


Fig. 2.13 Variation of water temperature profiles (in °C) with channel height at X' = 0.5 [3]

where they are closely resembling the one at $x_1' = 0$. Such phenomenon demonstrates the constantly renewal of thermal boundary layer at each oblique fin, keeping the thermal boundary layer thin for better heat transfer in comparison with conventional microchannel.

Variation of temperature profile with channel depth is then examined in Fig. 2.13. Except the bottom $(y_1'=0)$ and top surface $(y_1'=1)$ of microchannel, the other planes at various channel depth display a relatively consistent temperature profile among each other.

The combination of the boundary layers redevelopment and secondary flow effects results in superior heat transfer performance, leading to lower wall temperature compared to the conventional microchannel. Figure 2.14 shows that for the enhanced microchannel configuration, the maximum wall temperature is $T_{w,max} = 53.2$ °C, while the temperature gradient is $\Delta T_w = 13.7$ °C. The conventional microchannel heat sink, on the other hand, has a maximum wall temperature of 75.3 °C and a temperature gradient of 27.9 °C. Thus, the introduction of oblique fins resulted in the significant decrease of both the maximum wall temperature and temperature gradient of 22.1 and 14.2 °C, respectively.

In addition to the improvement in overall heat transfer performance, the presence of the oblique fins leads to significant local enhancement as illustrated in Fig. 2.15a. It is noticed that the initial heat transfer coefficient for conventional microchannel can be as high as ~15,000 W/m²K. However, it diminishes quickly as the boundary layer thickens when the fluid travels downstream and attains a fairly constant value

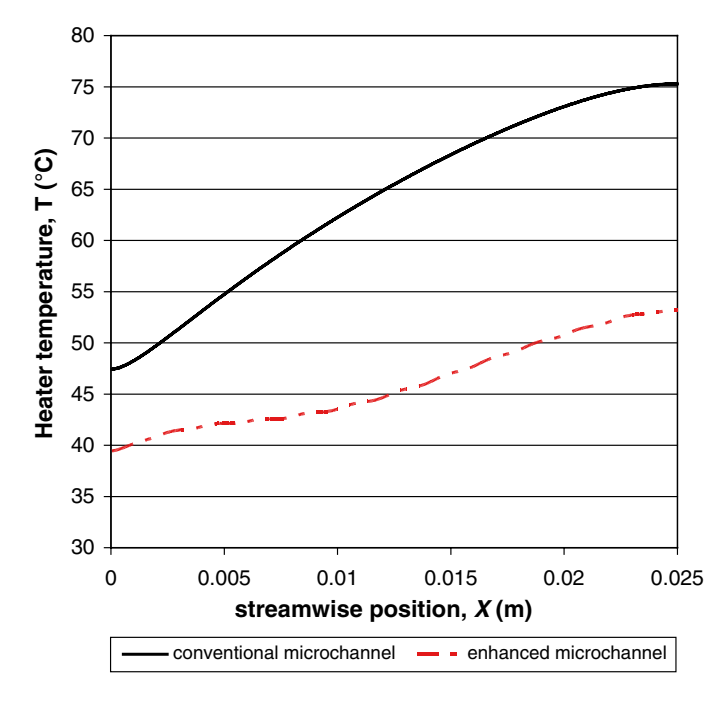


Fig. 2.14 Heater temperature profile for microchannel heat sinks [3]

at ~5,000 W/m²K, displaying a highly non-uniform heat transfer performance from the inlet to the outlet of the heat sink. In contrast, the variation of local heat transfer coefficients for the enhanced microchannel is smaller, with a higher averaged value of ~10,000 W/m²K. The local heat transfer coefficient is observed to increase 100 % almost everywhere. With the more effective heat transfer, 60 % more heat flux can be dissipated with the enhanced microchannel if the same maximum wall temperatures are maintained.

Moreover, it is observed that the level of heat transfer enhancement correlates closely with the percentage of secondary flows that are diverged through the oblique channel. Figure 2.15b illustrates the local heat transfer coefficient of the enhanced microchannel with the corresponding secondary flow percentage at each oblique channel branch. In this case, secondary flow rate percentage is defined as the proportion of coolant mass flux into oblique channel over coolant mass flux across the channel inlet. At the upstream of the microchannel heat sink, secondary flow rates are low and there is not much disruption to the coolant flow. Thus, heat transfer coefficient drops drastically from 15,000 to 8,000 W/m²K as thermal boundary layer develops. Subsequently, secondary flow that is diverted to flows into adjacent channel increases the transverse momentum of the coolant flow in the main channel and causes the secondary flow rate (or momentum) to build up and maintain at around 14 % for the downstream oblique channels. As a result, local heat transfer coefficient increases and hovers at a higher value at ~10,000 W/m²K.

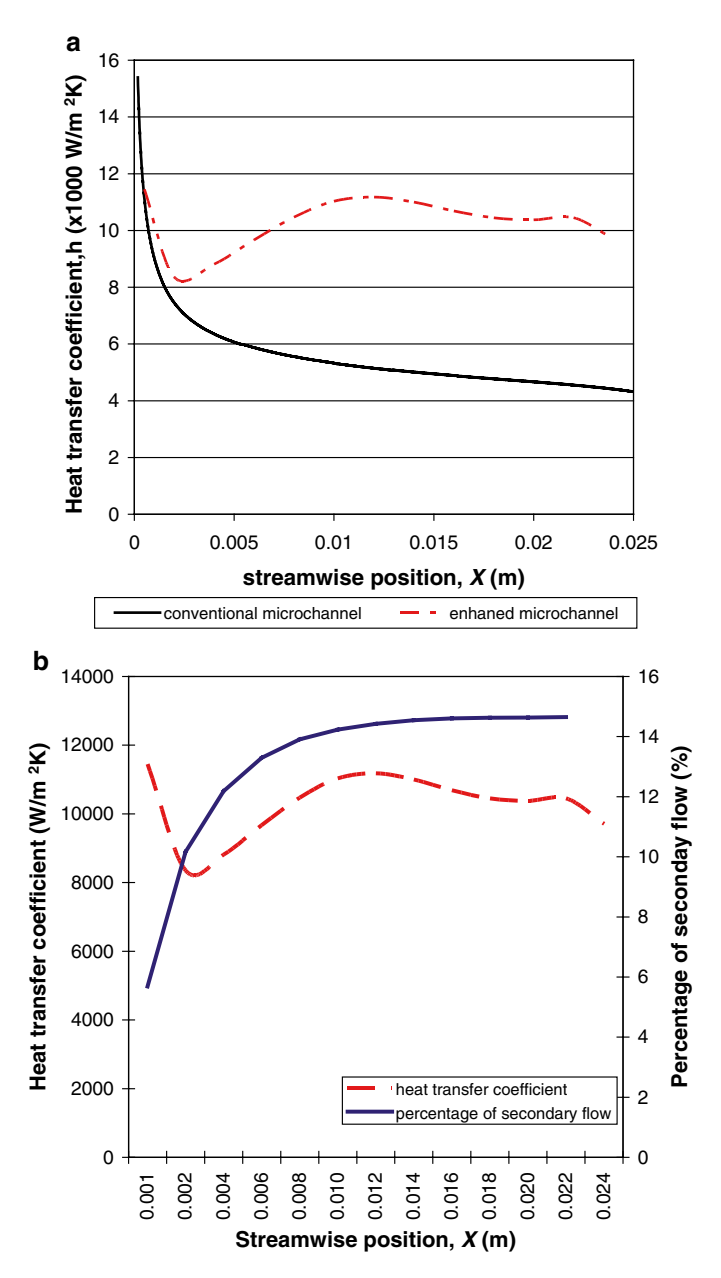


Fig. 2.15 Heat transfer coefficient profile for (a) comparison between microchannel heat sinks; (b) enhanced microchannel with percentage of secondary flows [3]

Steinke and Kandlikar [1] first proposed alternating the secondary channel direction in the streamwise direction with the intention to prevent flow migration. However, based on current simulation finding, it is highly possible that their configuration would not be able to generate sufficiently strong secondary flow as the transverse momentum in the flow is negated by the secondary flow in the opposite direction after each oblique channel branch. Sahnoun and Webb [17] developed the equations to predict flow efficiency in the louvred fin heat exchanger. In the context of louvred fin heat exchanger, flow efficiency is defined as the degree to which the flow follows the louvres, which is comparable to the percentage of secondary flow in the enhanced microchannel. Unfortunately, their equations cannot be adopted to predict the percentage of secondary flow for enhanced microchannel. The predicted secondary flow rate using the proposed equations by Sahnoun and Webb [17] is ~84 % compared to 14 % indicated in the simulation. The disparity is believed to be caused by the difference in the fin geometry in which oblique fin is much thicker than louvre fin. The thicker oblique fin reduces the oblique channel width significantly and results in much lower secondary flow percentage.

In comparison with enhanced microchannel, conventional microchannel experiences severe axial conduction or heat flux redistribution as a result of the non-uniform convective heat transfer performance as evident from Fig. 2.16. It is observed that channel walls at the inlet section dissipate 80 % more heat flux than the rest of the convective surfaces. Enhanced microchannel, on the other hand, dissipates 30 % more heat flux at the inlet region than the rest of heat transfer surfaces.

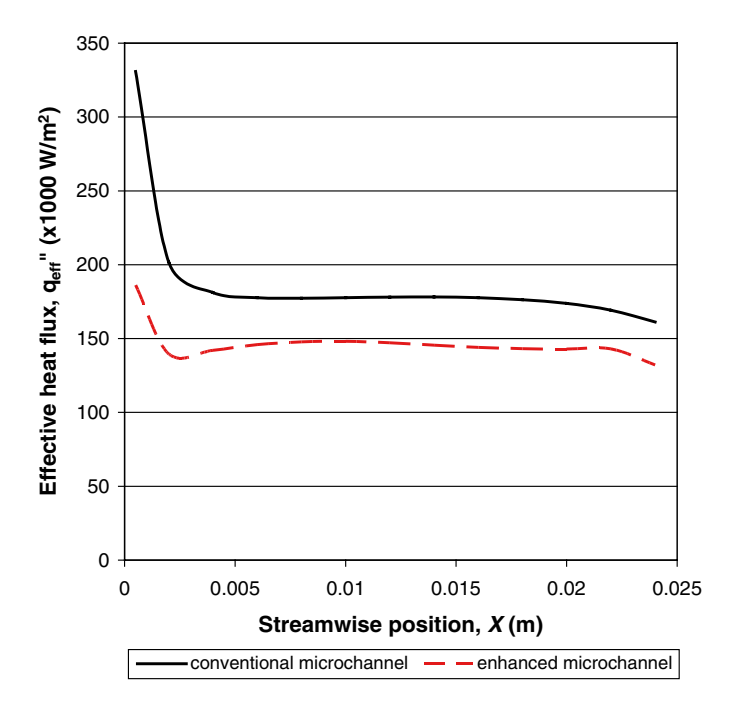


Fig. 2.16 Effective heat flux along microchannel heat sinks [3]

Such phenomenon leads to significantly higher temperature at the inlet region (as seen in Fig. 2.14) even though conventional microchannel exhibits comparable heat transfer coefficient as enhanced microchannel at the inlet. Owing to the larger heat transfer area, the average effective heat flux of enhanced microchannel is found lower than the one of convention microchannel.

Owing to the unique hydrodynamic and thermal boundary layer profiles in the enhanced microchannel heat sink, the amount of heat removed through each fin surface and the un-finned surface differs significantly, as shown in Fig. 2.17a.

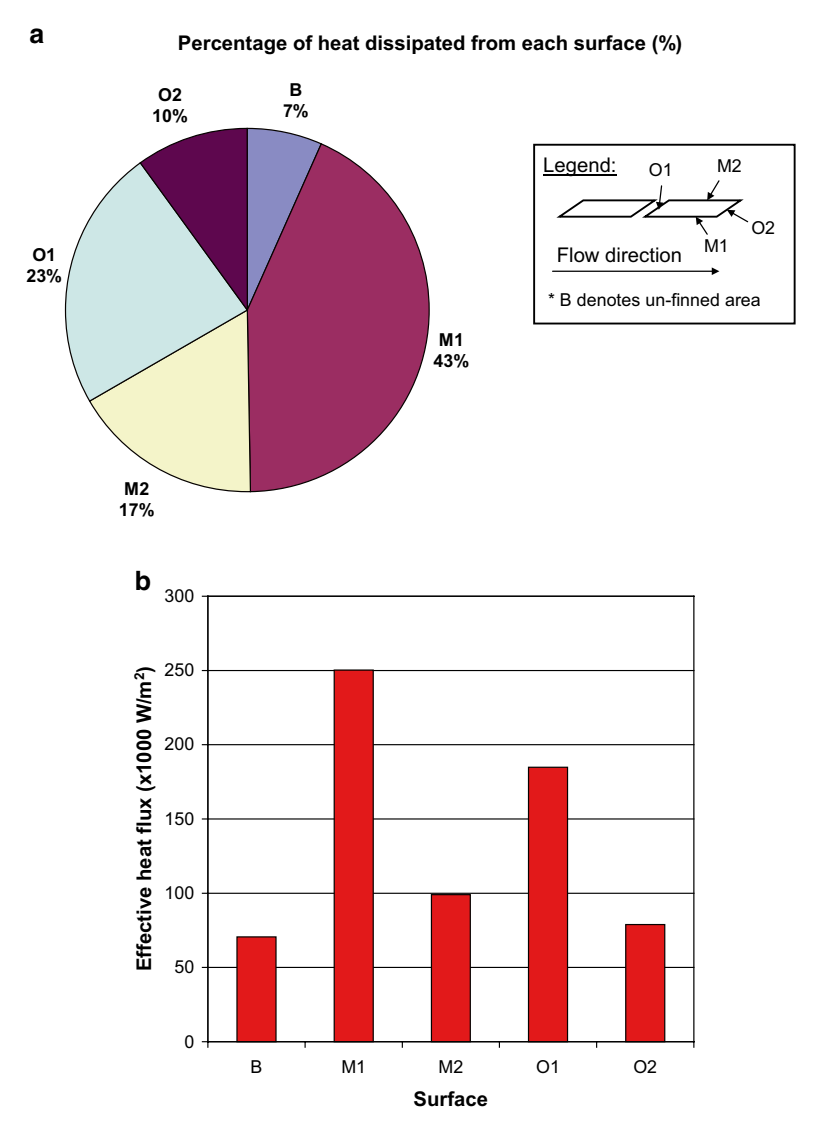


Fig. 2.17 (a) Percentage of heat dissipated from each surface; (b) effective heat flux dissipated from each surface [3]

Fin surfaces M1 and O1 record the highest percentage of heat removal with 43 and 23 % of total heat dissipated from each surface, respectively. Interestingly, surface M2, which is located alongside with surface M1 in the main channel (with equivalent heat transfer area and coolant mass flux), does not perform as good as surface M1. The fin surface M1 dissipates ~60 % more heat flux than surface M2. Moreover, surface O1 which has smaller heat transfer area and coolant mass flux (located in oblique channel) also removes heat more effectively compared with surface M2 (heat transfer area, M2: 25 %, O1: 18 %; average coolant mass flux, M2: 87 %, O1: 13 %). This phenomenon is mainly contributed by the skewed hydrodynamic and thermal boundary layer profiles as observed in Figs. 2.9 and 2.12. Surfaces M1 and O1 have much thinner boundary layer thickness compared with the rest of the fin surface and un-finned surface, thus managing to achieve highly augmented heat transfer. Figure 2.17b on the other hand displays the effective heat flux that is transferred through each surface, where surfaces M1 and O1 remove 250 and 190 kW/ m², respectively, while the rest of the surfaces dissipate less than 100 kW/m². This proves that surface M1 and O1, which are associated with thinner boundary layers than the rest of the surfaces, are the key surfaces in this passive heat transfer enhancement technique.

This novel idea for enhancing the heat transfer performance of microchannel heat sinks is attractive as the pressure drop penalty is small. As shown in Fig. 2.18, the pressure drop for the enhanced microchannel heat sink with oblique fins is only $\sim 10\%$ higher than that of a conventional microchannel heat sink. For the case of conventional microchannel, the pressure profile decreases linearly as the flow is

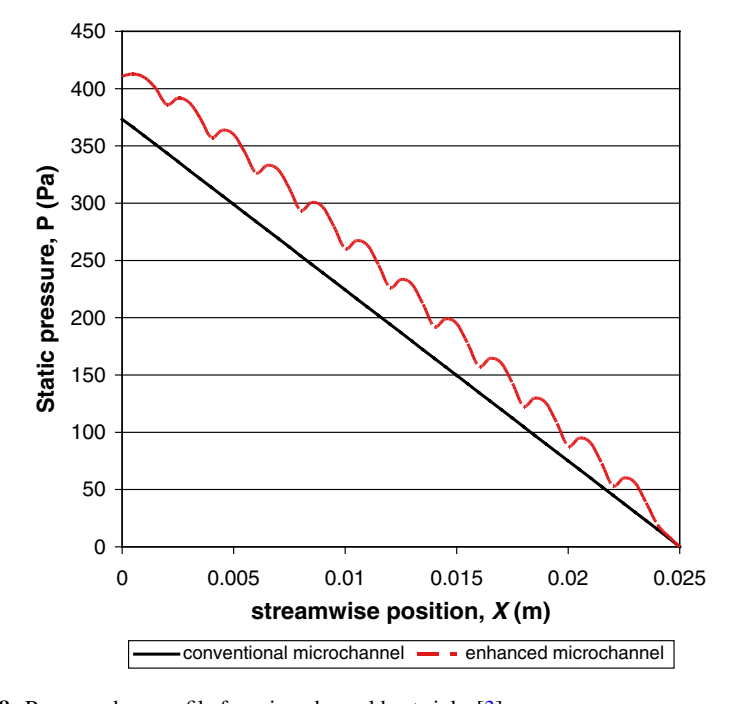


Fig. 2.18 Pressure drop profile for microchannel heat sinks [3]

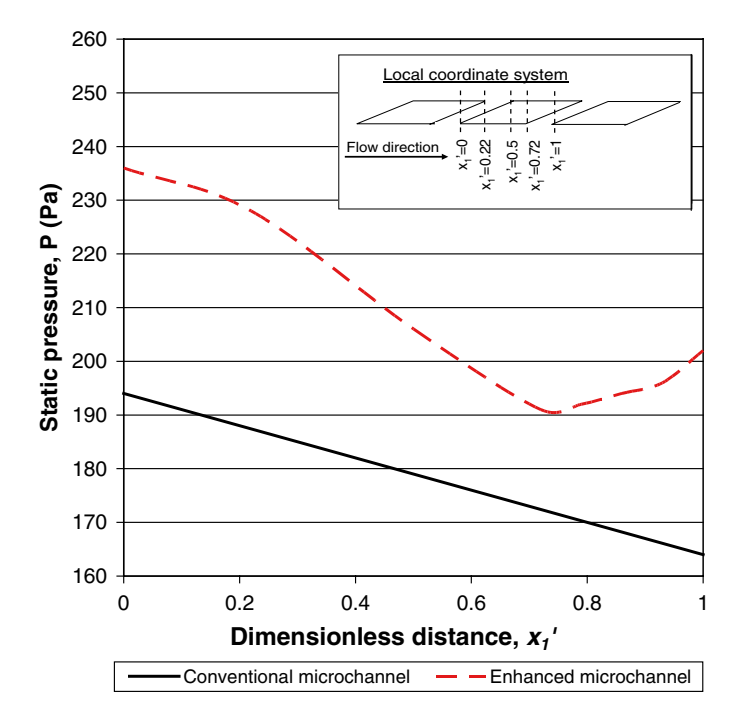


Fig. 2.19 Local pressure profile along the oblique fin [3]

fully developed hydrodynamically. On the other hand, the pressure profile for enhanced microchannel is characterized by local drops and recoveries.

Exploring further into the local pressure drop profile along the fin in Fig. 2.19 shows that pressure drop occurs for $x_1' < 0.72$ while pressure rise occurs for $x_1' > 0.72$. It is also noticed that the local pressure drop for the enhanced microchannel heat sink is steeper than that for the conventional microchannel. This could be due to the periodic redevelopment of hydrodynamic boundary layers which results in the thinning of the boundary layers. The local pressure drop is immediately followed by local pressure recovery when the flow from the main channel branches into the oblique channel.

This local pressure recovery was also observed by Alharbi et al. [14] in their numerical study on fluid flow through microscale fractal-like branching channel networks. They argued that the observed pressure recovery at each bifurcation may be due to the tapered increase in cross-sectional area similar to a "diffuser" following each bifurcation. The pressure recoveries compensate for the increased pressure drops, resulting in only a small overall pressure drop penalty. Similarly, Xu et al. [18, 19] observed the pressure recovery effect as coolant expands into the re-entrant chamber. The proposed oblique fin layout is different from the conventional passive heat transfer enhancement techniques, where there is a hefty trade-off in terms of pressure drop penalty that is always associated with the improved heat transfer.

For instance, pin-fin heat sinks achieved improved thermal performance over plate-fin heat sinks by hindering the development of the thermal boundary layer in a unidirectional flow at the expense of a significant pressure drop penalty [20].

2.3 Numerical Analysis: Full Domain Simulation

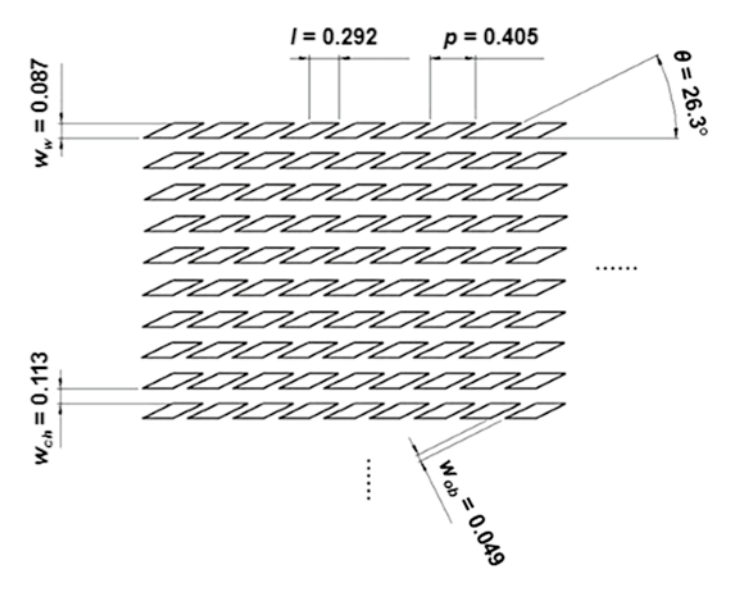
Numerical analysis employing full domain heat sink model is conducted to investigate the flow migration phenomenon and its effect on the overall fluid flow and heat transfer characteristics in the enhanced microchannel heat sink. A unique coolant distribution exists in the main channels and oblique channels as a result of continuous secondary flow generation and coolant migration. Simulation findings are in close proximity to that of the simplified numerical model for low flow rate case where both models display comparable fluid flow (velocity profiles) and heat transfer characteristics. However, it is also found that the simplified model, which assumes infinite span of oblique fins, over-predicts the heat transfer performance when the Reynolds number is higher.

2.3.1 Simulation Model

This full domain microchannel heat sink is modelled based on the actual siliconbased test vehicle used in experimental investigation [21] and incorporates inlet and outlet manifolds. Detailed geometries and the mesh intervals for the model are tabulated in Table 2.2, while Fig. 2.20 displays the sketch of oblique fin microchannel heat sink using oblique fins, where O1, O2, M1 and M2 are the different surfaces of oblique fin [22].

Table 2.2 Dimensional details of oblique fin microchannel heat sink model

Characteristic	Oblique fin microchannel
Material	Silicon
Heat sink footprint, width×length (mm)	12.7×12.7
Number of fin row, N	61
Main channel width, w_c (µm)	113
Fin width, w_w (µm)	87
Channel depth, H (μm)	379
Aspect ratio, α	3.35
Oblique channel width, w_{ob} (μ m)	49
Fin pitch, <i>p</i> (μm)	405
Fin length, <i>l</i> (μm)	292
Oblique angel, θ (°)	26.3
Mesh interval x, y, z (simplified model)	1,270×65×40
Mesh interval x, y, z (full domain model)	1,393×33×1,059



All dimension is in mm unless stated

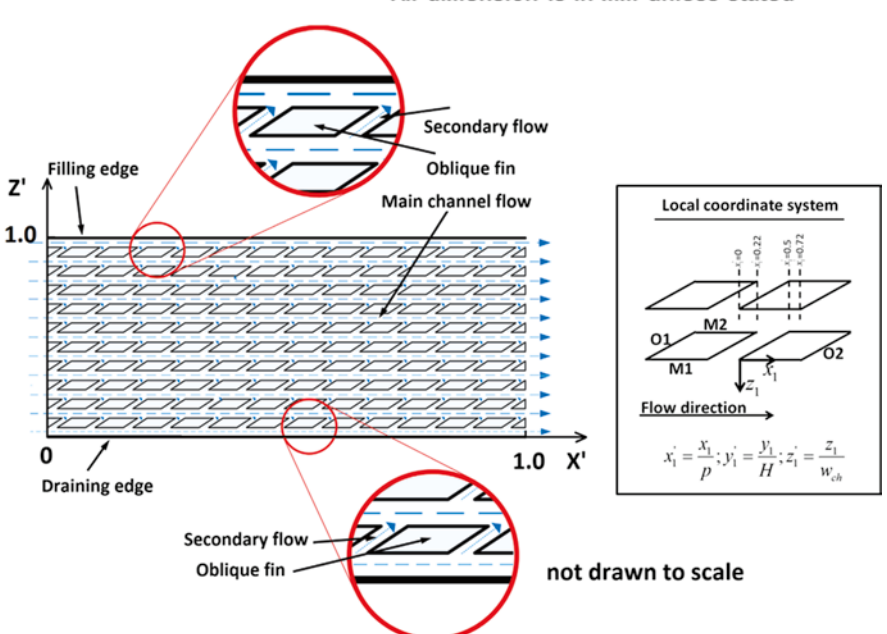


Fig. 2.20 Sketch of oblique fin microchannel heat sink

Emulating the silicon thermal test chips used in the experimental studies, the $12.7 \times 12.7 \text{ mm}^2$ microchannel heat sink model is divided into a cluster of 25 thermal test chips in a 5×5 grid array. Each thermal test chip is $2.54 \times 2.54 \text{ mm}^2$ with a heater measured at $2 \times 2 \text{ mm}^2$ located at the centre of silicon chip active surface.

Transient solver is adopted for full domain simulation as a result of the consideration of flow instability. The nature of flow in the oblique fin microchannel heat sink could be unsteady or periodic due to secondary flow generation and flow migration. The four governing equations solved in FLUENT v6.3 under transient solver consist of continuity equation, momentum equation, energy equation for liquid and energy equation for solid listed as follows:

$$\frac{\partial \rho}{\partial t} + \nabla \cdot (\rho \vec{v}) = 0 \tag{2.16}$$

$$\frac{\partial}{\partial t} (\rho \vec{v}) + \nabla \cdot (\rho \vec{v} \vec{v}) = -\nabla P + \nabla \cdot (\mu \nabla \vec{v})$$
 (2.17)

$$\frac{\partial}{\partial t} \left(\rho \vec{v} c_p T \right) + \nabla \cdot \left(\rho \vec{v} c_p T \right) = \nabla \cdot \left(k \nabla T \right) \tag{2.18}$$

$$\frac{\partial}{\partial t} (\rho c_p T) + \nabla \cdot (k \nabla T) = 0 \tag{2.19}$$

Different flow rates are set for the full domain model as compared with the data from experimental studies [21], while the analysis and comparison mainly focus on low flow rate setting, Re=250, and high flow rate setting, Re=660. For all cases considered, a uniform inlet pressure is assigned to the inlet. Inlet pressure is adjusted to achieve the targeted mass flow rate or Reynolds number. Furthermore, pressure outlet boundary condition is assigned to the outlet, where the flow is assumed to reach atmospheric pressure at the outlet of the heat sink. Each of the 25 heaters is supplied with heat flux at 274 W/cm² while the top surface of the silicon-based microchannel is assumed bonded with adiabatic cover for sealing purposes. Courant numbers for the low flow rate and high flow rate cases are 16.7 and 5.2, respectively. As the full domain simulation model adopts implicit unsteady formulation, a larger Courant number can be used to achieve fast convergence.

The current mesh count for full domain model of $1,393\times33\times1,059$ results in a total of 42,915,914 cells. The mesh interval for the full domain model is replicated into the simplified model to study the grid sensitivity [3]. The resultant mesh count in the simplified model is $1,058\times33\times17$, and the computed average Nusselt number is 18.48 when Re=660. The variations in average Nusselt numbers are 3.5% from the

mesh density for full domain model to the mesh interval selected for the simplified model. Although the mesh density is reduced to accommodate for the large full domain model simulation, the selected mesh interval still provides reasonable accuracy in prediction. In addition, the simulation results for the full domain model would be verified against the experimental findings for its validity.

2.3.2 Validation of Numerical Simulation

Figure 2.21 shows the total pressure drop and average Nusselt numbers comparisons with different Reynolds numbers for the oblique fin microchannel heat sink between results from full domain simulation model and experimental data [22]. It is found that the maximum deviation of total pressure drop between numerical and experimental results is less than 7 % under all Reynolds numbers. Unfortunately, the computed average Nusselt numbers for oblique fin microchannel after temperature correction are about 20 % lower than the predictions by full domain simulation model. This could be caused by the lack of information in the measurability of thermal sensors leading to an inaccurate temperature correction. A trial using –2.7 °C as the correction factor in computation results in Nusselt numbers that are closely imitating the simulation results. This indicates that the numerical simulation studies are validated by the experimental measurement.

2.3.3 Fluid Flow and Heat Transfer Characteristic

The main objective of the full domain simulation model is to scrutinize the coolant mass distribution and flow instability for oblique fin microchannel heat sink and its effect to fluid flow and heat transfer. In this section, the simulation results for the full domain model are discussed when Re is 250 and 660.

Figure 2.22 shows the flow distribution of coolant in every main channel along the streamwise direction when Re=250. At the upstream (X'=0.01) of the oblique fin microchannel heat sink, significant variation is observed for the mass flow rate in the main channel along the dimensionless heat sink width, Z'. Apart from the region between 0.4 < Z' < 0.8, which has a comparable mass flow rate at 4.1×10^{-5} kg/s, the mass flow rate is significantly higher in the main channels at Z' < 0.4 and lower in the main channels at Z' > 0.8. The highest mass flow rate occurs in the first main channel in the spanwise direction (Z'=0.02) at 5.9×10^{-5} kg/s, which is almost 44% higher than the nominal mass flow rate of the main channels. On the other hand, the lowest mass flow rate occurs in the last main channel in the spanwise direction (Z'=0.98) at 2.9×10^{-5} kg/s, a 29% off from the nominal main channel mass flow rate. This indicates that the coolant mass distribution is skewed towards Z'<0.5 in the heat sink for this upstream position. This phenomenon occurs due to the fact that the coolant mass is forced to redistribute in the inlet manifold in order to maintain a

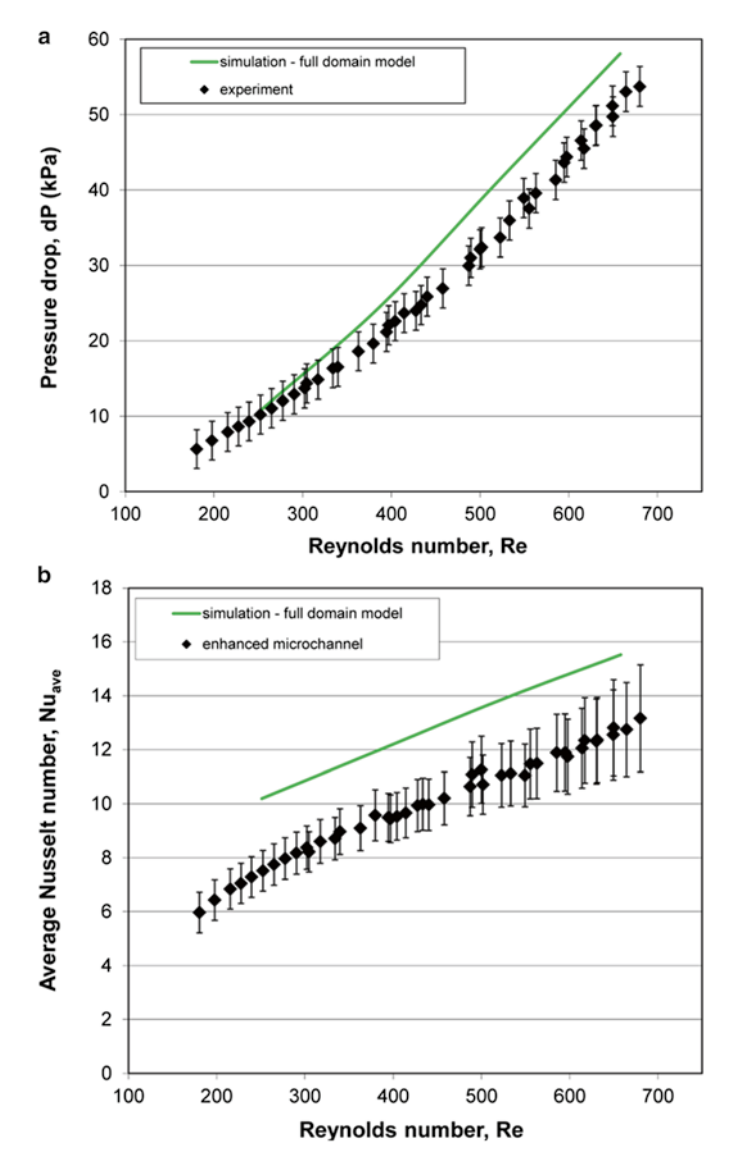


Fig. 2.21 (a) Total pressure drop comparisons and (b) average Nusselt number comparisons between numerical results and experimental data for the oblique fin microchannel heat sink

uniform pressure between the inlet and outlet as flow migration takes place within the heat sink. It is also noticed that except for Z' > 0.8, the mass flow rate in the main channel at X' = 0.01 is at least 10 % higher than that of the downstream locations. Low secondary flow rates in the oblique channels at X' = 0.01 is identified as the contributing factor and this will be elaborated further in the later section.

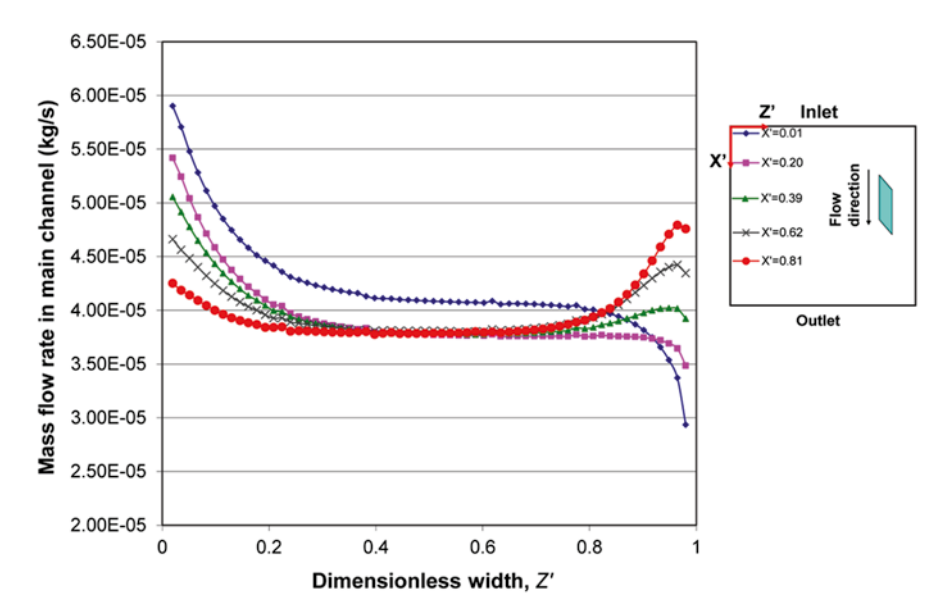


Fig. 2.22 Coolant mass flow rate distribution in the main channels of oblique fin microchannel heat sink when Re = 250

As coolant travels downstream, secondary flow generation and flow migration occur continuously. Mass flow rate in the main channels for Z' < 0.3 keeps reducing, while mass flow rate in the main channels for Z' > 0.7 rises consistently as it is illustrated in Fig. 2.22. This trend clearly demonstrates the coolant migration phenomenon. Coolant mass is observed to migrate from Z' < 0.5 half of the heat sink to Z' > 0.5 half of the heat sink as coolant flows downstream. Thus, small regions at Z' > 0.8 and X' < 0.2 with low coolant mass exist as a result of the coolant migration in the diagonal direction following the direction of secondary flow. Despite all the flow migration, the main channels located between Z' = 0.25 and Z' = 0.75 maintain a relatively consistent mass flow rate at all streamwise locations examined. This area constitutes 50 % of the heat sink and is influenced by the flow migration.

Examining Fig. 2.23 provides some insights to the coolant distribution in the oblique channels within the heat sink. Generally, the coolant flow rate in the oblique channels is an order of magnitude lower than that of the main channels. These oblique channels are sized such that they generate sufficiently strong secondary flows or momentums to disrupt the boundary layer development and promote fluid mixing, while avoiding unnecessary disturbance to the flow. The mass flow rate through the oblique channels at the upstream of the heat sink (X'=0.01) is significantly lower compared with other downstream locations. When the coolant first enters the oblique fin microchannel heat sink, it flows primarily in the streamwise direction and has a very limited transverse velocity component or momentum. Oblique channels on the other hand branch off from the main channels with their flow path swayed away from the streamwise direction. Thus, the fraction of coolant

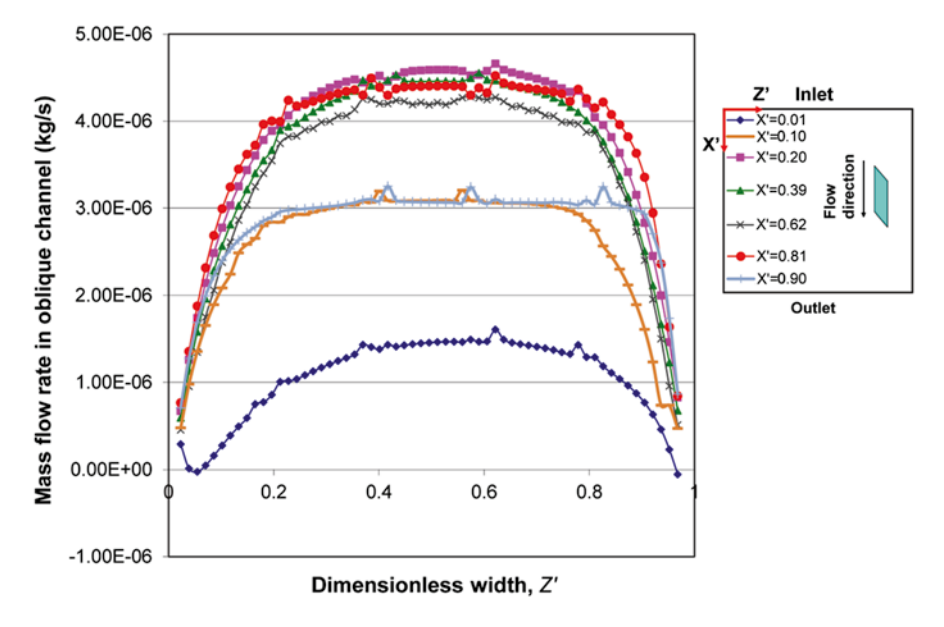


Fig. 2.23 Coolant mass flow rate distribution in the oblique channels of oblique fin microchannel heat sink when Re = 250

in the main channels that diverges into the oblique channels is limited at this upstream position. However, as the coolant flows downstream, the transverse velocity component and momentum build up as flow continues to divert into oblique channels, before being injected to the adjacent main channels. Consequently, secondary flow rates through the oblique channels elevate to a higher value (about 10 % of total coolant mass flow rate except in edge regions) and remain consistent throughout the heat sink from X' = 0.20 onwards. There is fluctuation in the secondary flows at different downstream locations, but the magnitude of the variation is not significant.

An "n" shape parabolic curve also indicates that secondary flow rates in the oblique channels located closer to the heat sink edge (Z' < 0.2 and Z' > 0.8) are lower than that of the oblique channels at the centre of the heat sink. Similar phenomenon is also observed by Dejong and Jacobi [2] in their flow visualization study on louvred fin heat exchanger. They concluded that wall effect existed on several fin rows next to the walls, where flow is characterized by lower flow efficiency (low secondary flow rate) and lower heat transfer. Low secondary flow rates in the oblique channels at the edge of the heat sink are also believed to result in lesser heat transfer enhancement compared with those at the centre of the heat sink in the context of enhanced microchannel. However, there is still at least 60 % of the total heat sink width having consistent secondary flow rates, and it will be explored further in the later sections whether this affects the heat transfer performance of the heat sink globally and locally.

Besides scrutinizing the macroscopic effect of the flow migration to the overall flow distribution, the full domain simulation highlights the development of local coolant velocity and temperature profiles at different spanwise and streamwise positions. Figure 2.24a displays the coolant velocity profiles at the mid-depth plane in multiple main channels at X' = 0.01 ($x_1' = 0$). Generally, developing velocity profiles emerge in the main channels at this upstream position of the heat sink just as

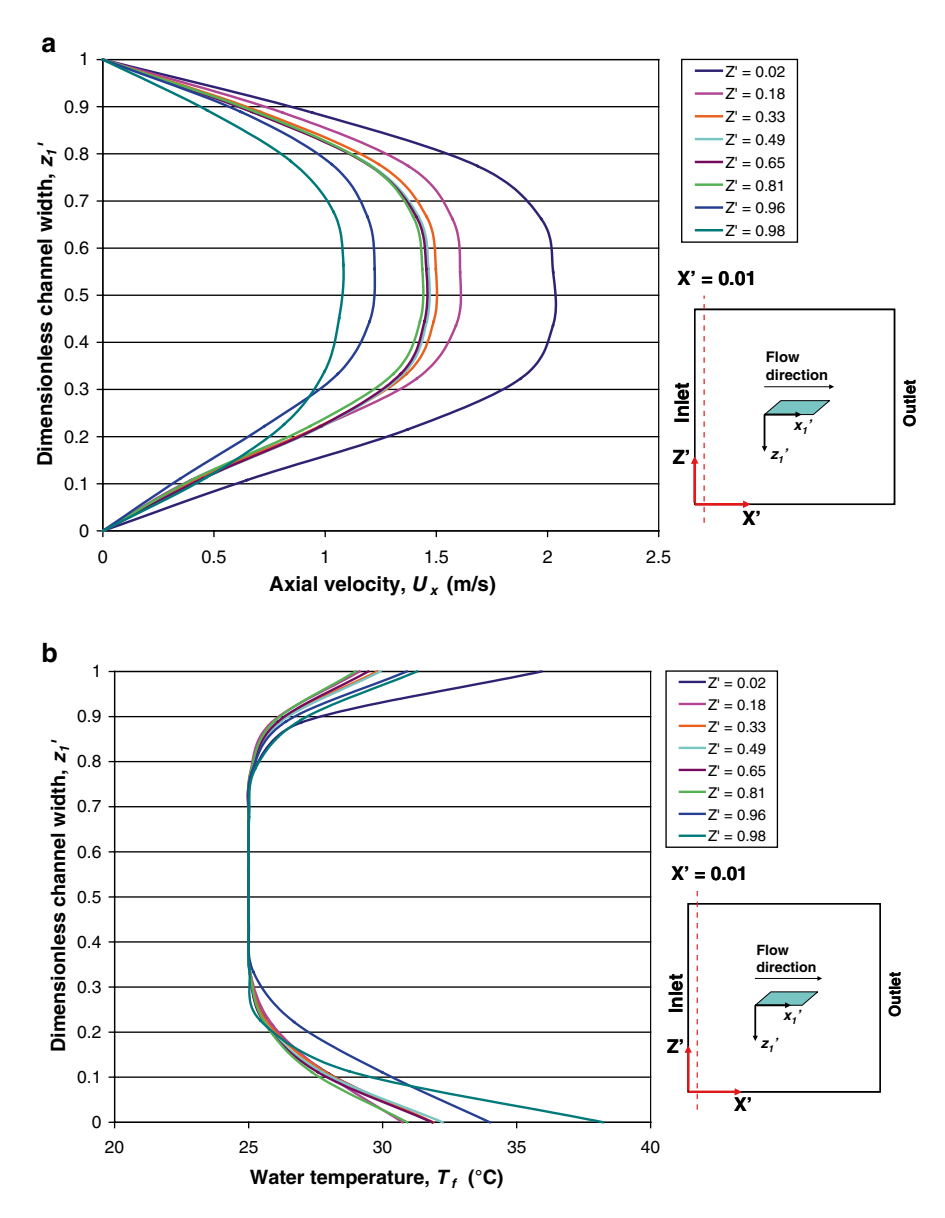


Fig. 2.24 Coolant (a) axial velocity and (b) temperature profiles in the main channels at X' = 0.01, Y' = 0.5, when Re = 250

coolant enters the heat sink. Velocity magnitudes are observed to reduce as Z' increases, aligning well with the observation from Fig. 2.3, where coolant mass is concentrated towards Z' < 0.5 half of the heat sink. As a result, velocity profiles skew slightly towards $Z_1' = 1$ in the main channels. However, the velocity profiles are almost symmetrical at the centre of the channels, as coolant flows primarily in the axial direction. The resultant coolant temperature profiles at the mid-depth plane are showed in Fig. 2.24b. Similarly, developing temperature profiles are displayed as most of fluid temperature remains at the inlet temperature. Coolant temperature in the main channel at Z' = 0.98 is significantly higher compared to the rest of the channels as this channel receives the least coolant mass among others.

As coolant travels downstream to X' = 0.20, velocity profiles continue to develop and become significantly different from that of X' = 0.01. Figure 2.25a displays the velocity profiles in the main channels where most of them skew towards $z_1'=0$ due to the divergence of fluid into oblique channels, which brings the fluid particles from the centre of the channel closer to fin surface M1 $(z_1'=0)$. As a result, plane $z_1' = 0$ (fin surface M1) has the thinner boundary layer thickness compared to plane $z_1'=1$ (fin surface **M2**). Details and discussions about the boundary layer development along the sectional oblique fin have been studied by present authors in [22]. Coolant in the main channels between 0.18 < Z' < 0.81 maintains a consistent velocity profile while the others display varying velocity profiles under the influent of flow migration and non-uniform secondary flow rate. On the other hand, the main channel at Z'=0.02 continues to show the highest axial velocity than the rest. Besides, the main channel at Z' = 0.02 together with those main channels at Z' > 0.9display a velocity profile that is more symmetry than those between 0.18 < Z' < 0.81as secondary flow rates are lesser in these regions. Consequently, coolant temperature profiles at the mid-depth plane are very different from each other as demonstrated in Fig. 2.25b. Generally, skewed coolant temperature profiles emerge in the main channels between 0.18 < Z' < 0.81 owing to the skewed velocity profiles that present in the channels. Water temperatures in this region are more uniform, and wall temperatures (temperature at $z_1' = 0$ and $z_1' = 1$) are also found to be lower than in the channels outside this region. This indicates that the fluid mixing and heat transfer from the channel surfaces between 0.18 < Z' < 0.81 is more efficient than the rest. The effect of the skewed coolant water temperature profiles to the heat transfer was discussed in detail in the previous publication [22]. Wall temperature is the highest on surface $z_1'=1$ and $z_1'=0$ for main channels at Z'=0.02 and Z'=0.98, respectively, as these two channels are located at the edge of the heat sink, where the heat dissipation is concentrated onto these surfaces.

Moving forward to X' = 0.62 in Fig. 2.26a, similar velocity profiles are observed for main channels within Z' = 0.18 and Z' = 0.81 with minimum change compared with those at the axial distance of X' = 0.20. However, the axial velocity in the main channel at Z' = 0.02 declines, while the axial velocity in the main channels at 0.96 < Z < 0.98 rises as coolant continues to migrate towards Z' = 1.

It has been demonstrated that the characteristic of secondary flow in oblique channels has great impact on the local, as well as global, heat transfer enhancement of the heat sink. Thus, it is important to examine the local coolant behaviour in the

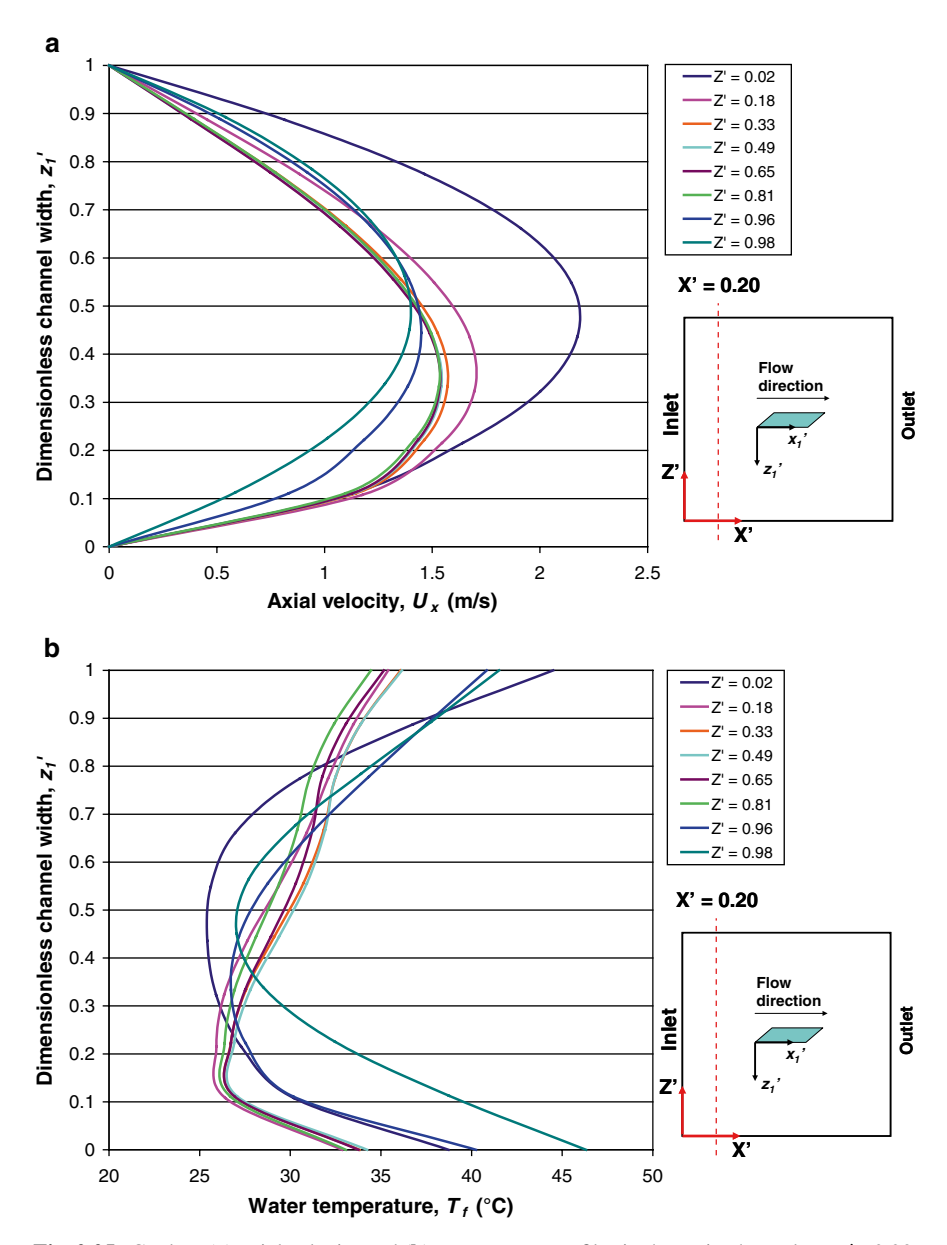
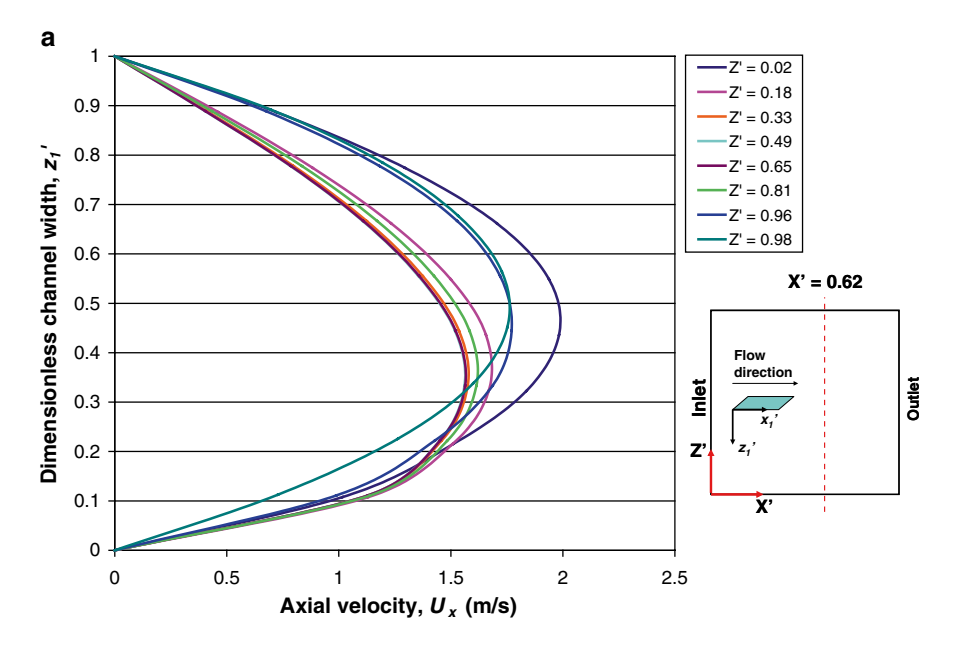


Fig. 2.25 Coolant (a) axial velocity and (b) temperature profiles in the main channels at X' = 0.20, Y' = 0.5, when Re = 250

oblique channels within the full domain heat sink. Figure 2.27a displays the coolant axial velocity profiles (mid-depth plane) in the oblique channels at different spanwise positions at the dimensionless axial distance of X' = 0.01. At this upstream



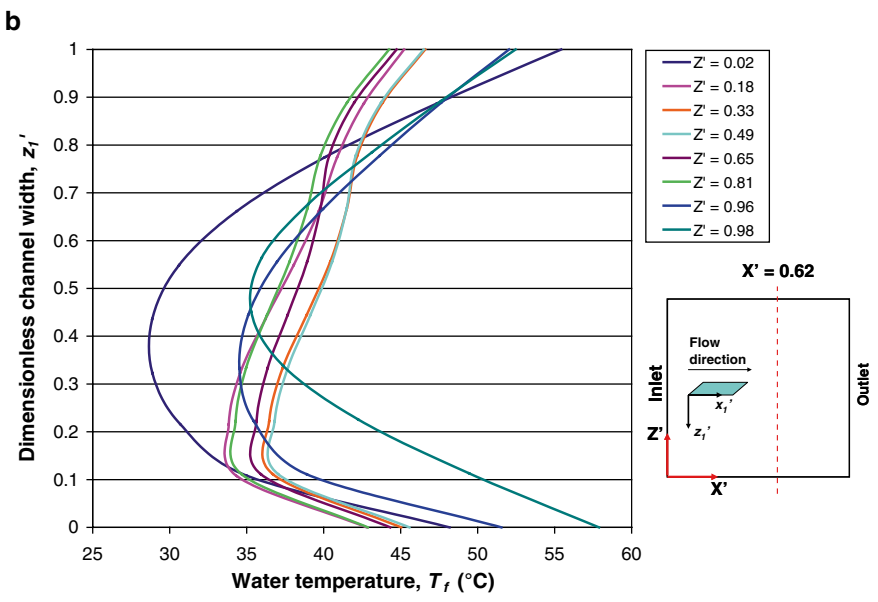


Fig. 2.26 Coolant (a) axial velocity and (b) temperature profiles in the main channels at X' = 0.62, Y' = 0.5, when Re = 250

position of the heat sink, there is a very limited amount of coolant mass diversion into the oblique channels. Axial velocity in most of the oblique channels is as slow as 0.1 m/s and displays a symmetrical profile at the centre of the channel.

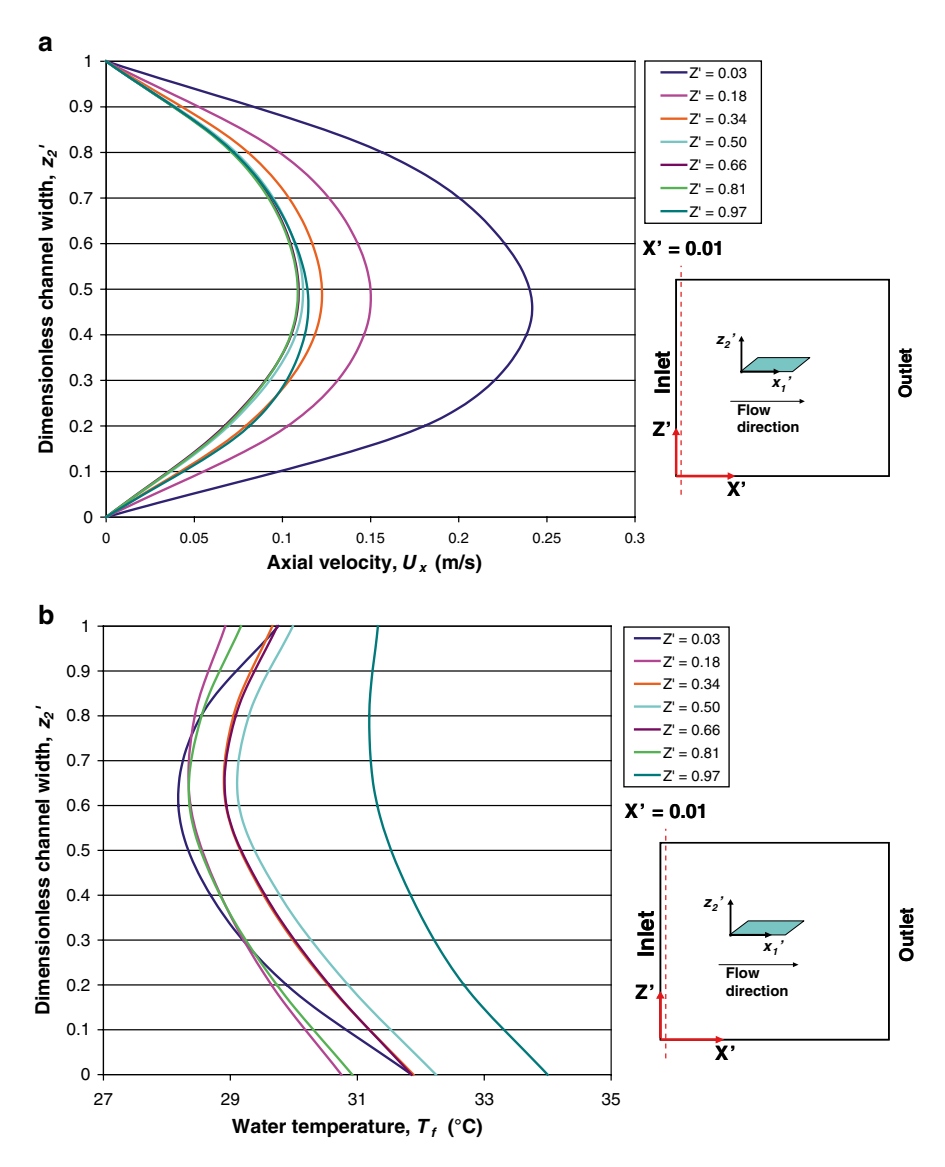


Fig. 2.27 Coolant (a) axial velocity and (b) temperature profiles in the oblique channels at X' = 0.01, Y' = 0.5 (*mid-depth plane*), when Re = 250

Despite the symmetry in velocity profiles in the oblique channels, water temperature profiles in Fig. 2.27b display highly asymmetric curves with the higher water temperatures occur for coolant at $z_2' < 0.5$ and higher wall temperatures for fin surfaces $z_2' = 0$ than those at $z_2' = 1$. This is possible because these two fin surfaces at $z_2' = 0$ and $z_2' = 1$ belong to different oblique fins. Fin surface $z_2' = 0$ is part of the downstream oblique fin that is located closer to the discrete heat source. Thus, more heat is expected to conduct into this fin and surface $z_2' = 0$ in comparison with surface $z_2' = 1$, which is one of the fin surfaces for the upstream fin.

As discussed earlier, significant changes occur to the velocity and temperature profiles in the main channels when coolant travels from X' = 0.01 to X' = 0.20. Thus, similar developments are expected for the profiles in the oblique channels. Except the two oblique channels that are located next to the heat sink edge (Z' = 0.03 and Z' = 0.97), the axial velocity in the oblique channels in Fig. 2.28a marks an appreciable rise. The magnitude of axial velocity increases with the distance from the

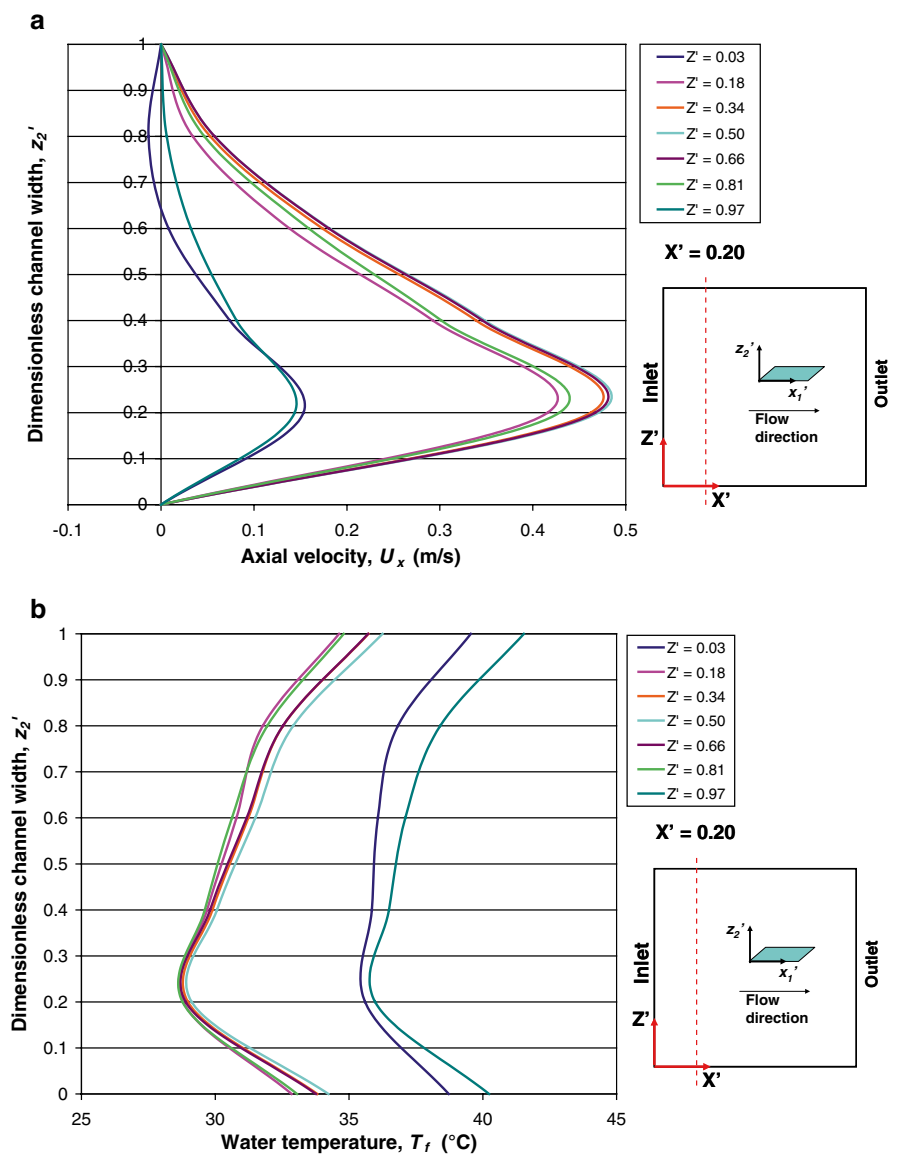


Fig. 2.28 Coolant (a) axial velocity and (b) temperature profiles in the oblique channels at X' = 0.20, Y' = 0.5, when Re = 250

heat sink edge, agreeing to the finding from Fig. 2.23. Therefore, coolant in the oblique channels between 0.18 < Z' < 0.81 has significantly lower water and wall temperatures than those receiving less coolant as demonstrated in Fig. 2.28b. It is also noticed in Fig. 2.28 that these velocity profiles skew towards $z_2' = 0$ (fin surface O1), which subsequently produce a thinner boundary layer thickness for fin surface O1 at $z_2' = 0$. Owing to the asymmetry of velocity profiles, temperature profile in the oblique channels displays the similar trend to that of the main channels, where the temperature profiles skew towards the fin surfaces with thinner hydrodynamics boundary layer. The thinner thermal boundary layer thickness on these fin surfaces results in superior heat transfer performance and also lower wall temperatures than the other fin surfaces. Detailed discussion on the heat transfer mechanism is present in the previous publication [22].

Comparable velocity and temperature profiles emerge further downstream in the oblique channels at X'=0.62 as both the velocity and temperature profiles are noticed to stabilize as coolant flows past X'=0.20. Again, the simulation findings show that flow migration affects the global secondary flow distribution within the heat sink but has little influence to the local velocity and temperature profiles. Apart from the channels that are located close to the heat sink edge, which is highly affected by flow migration and edge effect, channels within 0.18 < Z' < 0.81 demonstrate consistent local velocity and temperature profiles for all axial distances examined (Figure 2.29).

Unlike the simulation findings in the previous analysis, where oblique fin microchannel heat sink achieves steady state condition at Re=250, the simulation result shows signs of unsteadiness when Reynolds number is increased to Re=660. Fluctuations are observed in velocity profiles and also in the temperature profiles in the heat sink. Figure 2.30a, b displays the local velocity and temperature profiles of liquid coolant at the mid-depth plane of a channel located at X=7.81 mm, Z=8.28 mm (X'=0.61, Y'=0.5, Z'=0.65) when Re=250. Based on the plots, it is observed that both the velocity and temperature profiles at different time steps overlap each other, indicating that the flow regime is steady. On the contrary, when examining the local velocity and temperature profiles of liquid coolant at the middepth plane of a channel at X=7.81 mm, Z=4.19 mm (X'=0.61, Y'=0.5, Z'=0.33) when Re=660 in Fig. 2.30c, d the fluctuation appear.

2.3.4 Heat Transfer Performance

In order to further explore flow migration phenomenon, local and global heat transfer performance was investigated based on the full domain simulation for oblique fin microchannel heat sink when Re=250 and 660.

Figure 2.31 illustrates the temperature contour of heat sink (bottom wall) for the case Re=250, where the wall temperature increases with the flow length due to the sensible heat gain by coolant and the variation of heat sink cooling performance. As this silicon-based microchannel heat sink has multiple discrete heat sources, the

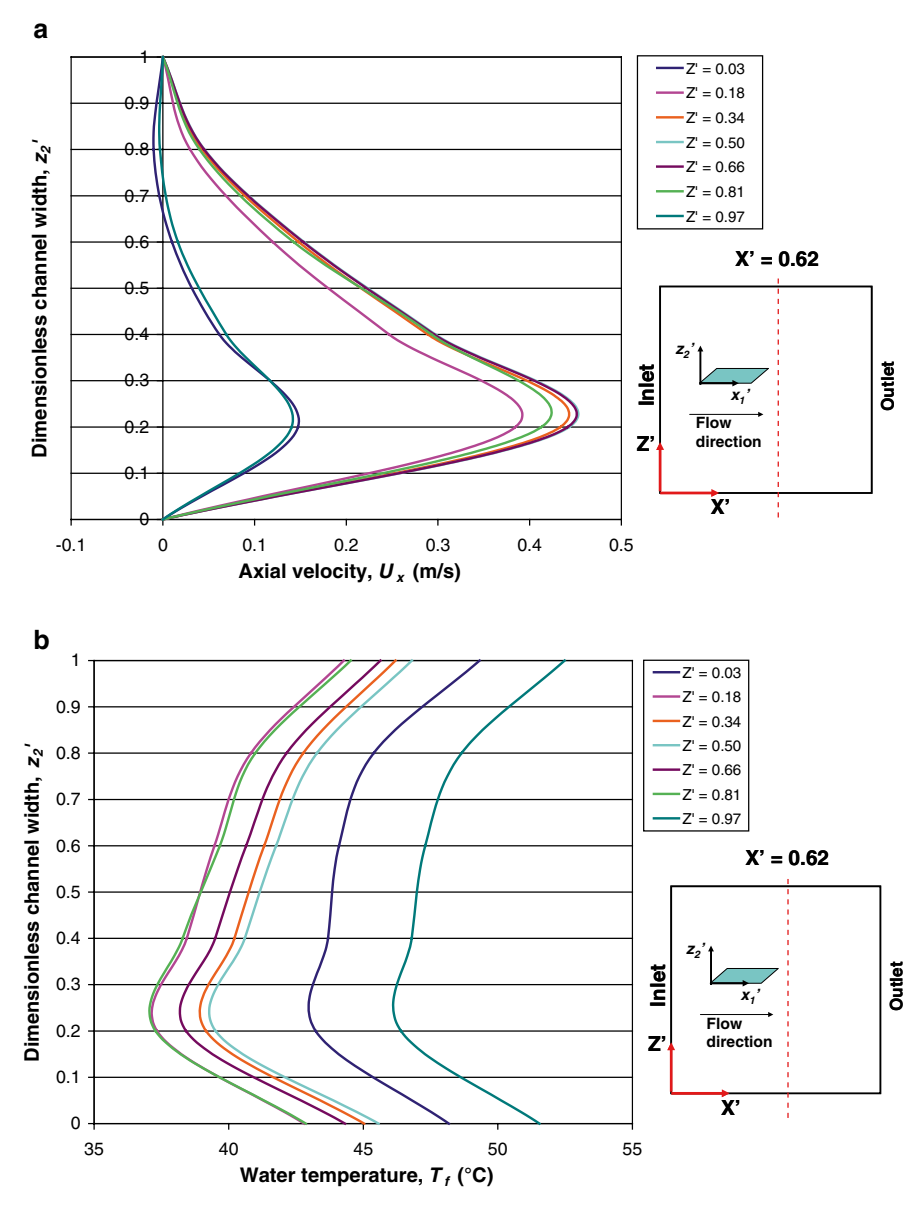
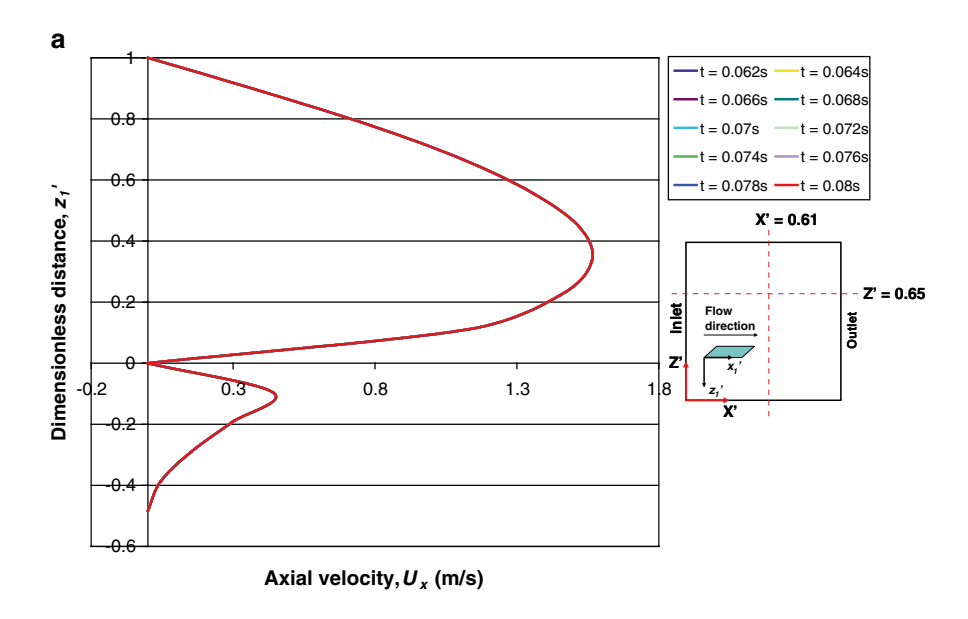


Fig. 2.29 Coolant (a) axial velocity and (b) temperature profiles in the oblique channels at X' = 0.62, Y' = 0.5, when Re = 250

highest temperature occurs within the heat source itself, and the wall temperature of non-heated area is obviously lower. It is also noticed that the maximum wall temperature of each individual heater is located slightly downstream from the centre of the heat source due to the combined effect of sensible heat gain by coolant, heat



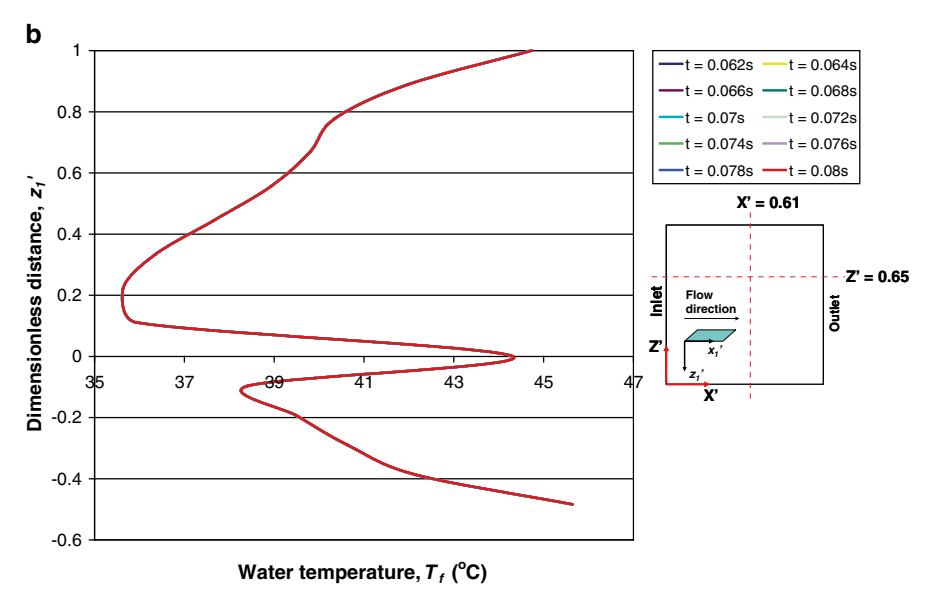


Fig. 2.30 Variation of (a) axial velocity profiles when Re=250, (b) water temperature profiles when Re=250, (c) axial velocity profiles when Re=660, (d) water temperature profiles when Re=660 in the mid-depth plane of channel within the oblique fin microchannel heat sink at different time steps

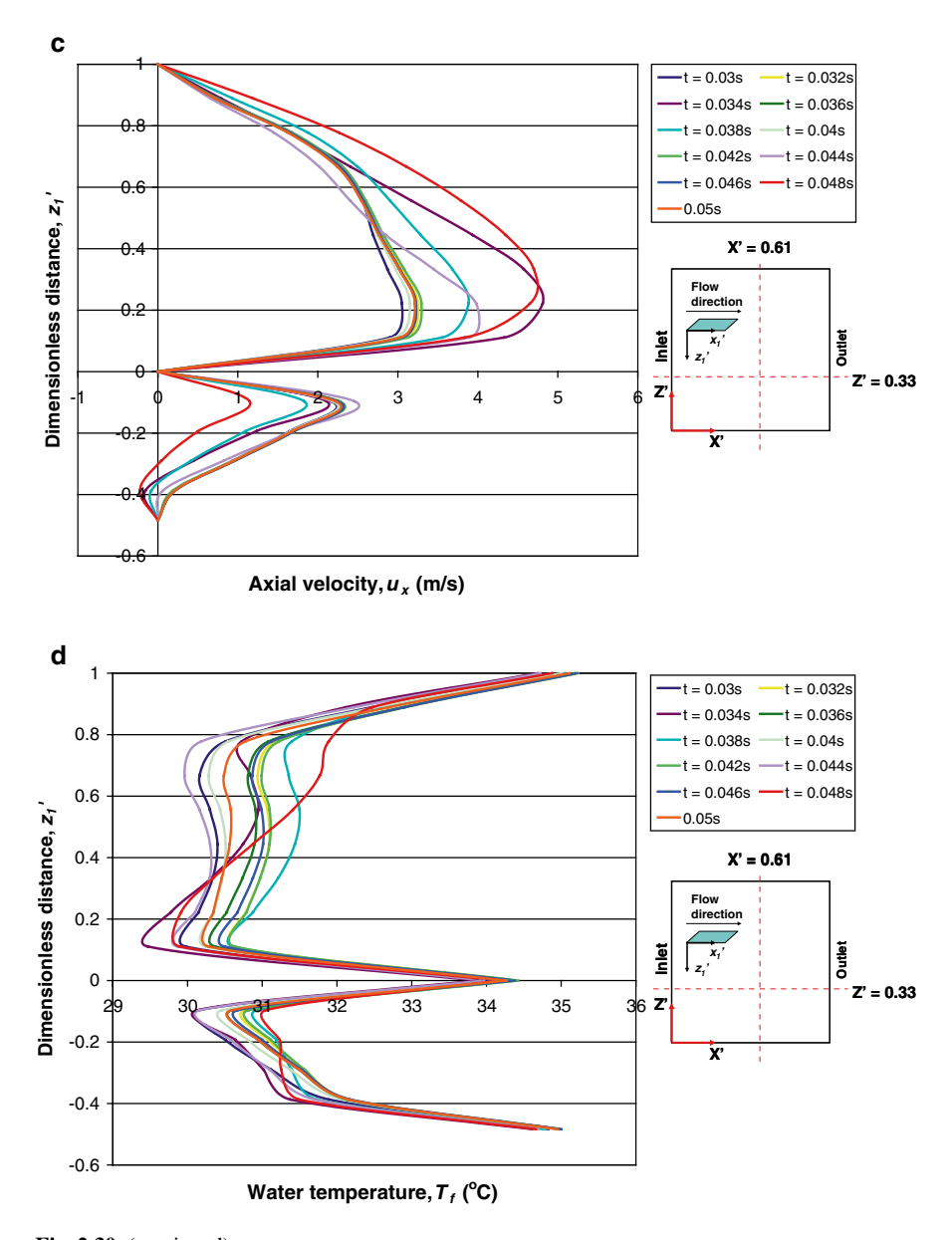


Fig. 2.30 (continued)

spreading and variation of heat transfer performance along the heat sink. Heaters on both edges of the heat sink (Z' = 0.1 and Z' = 0.9) also display higher wall temperatures than those at the centre of the heat sink. Similar trend is observed from Fig. 2.32, which plots the area-weighted average temperature of 25 heaters based on

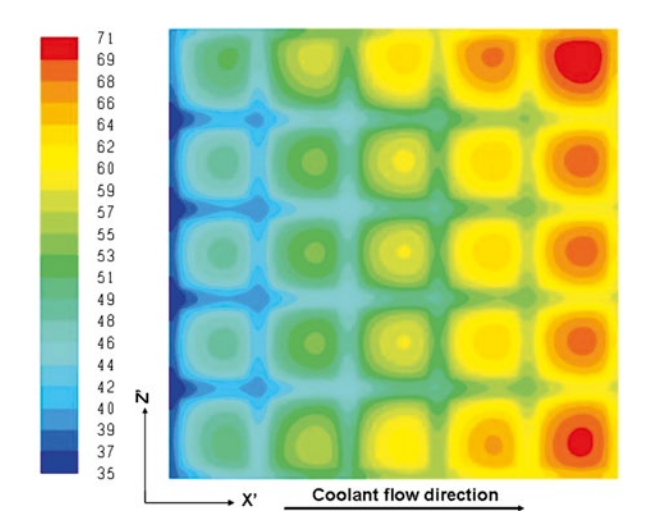


Fig. 2.31 Temperature contour (in °C) at the bottom wall of heat sink for Re = 250

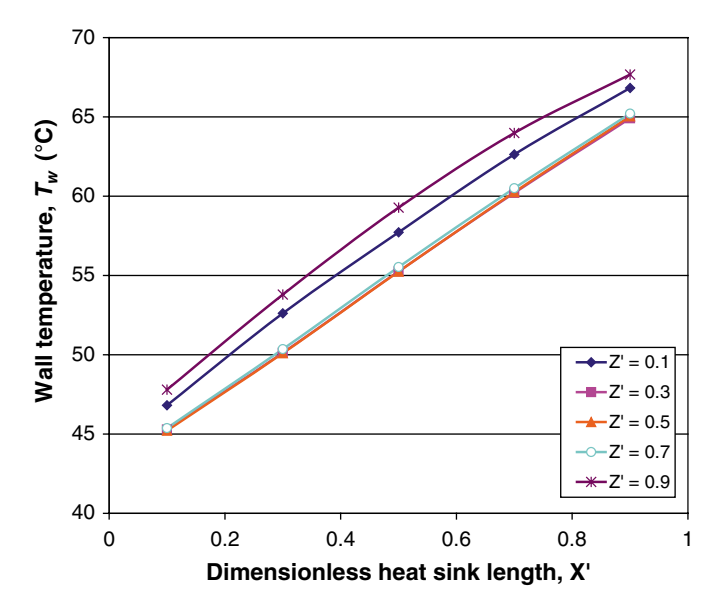


Fig. 2.32 Average heater wall temperature profiles in the oblique fin microchannel heat sink when Re = 250

the dimensionless heat sink width and axial distance. Wall temperatures are the highest for heaters at Z'=0.9, followed by Z'=0.1, while the lowest wall temperatures are recorded for heaters between 0.3 < Z' < 0.7 and they almost overlap each other. Several contributing factors to such heater temperature profile are identified as non-uniform secondary flow distribution, flow migration, edge effect and heat spreading effect.

Fig. 2.33 Local heat transfer coefficient profiles of oblique fin microchannel heat sink when Re = 250

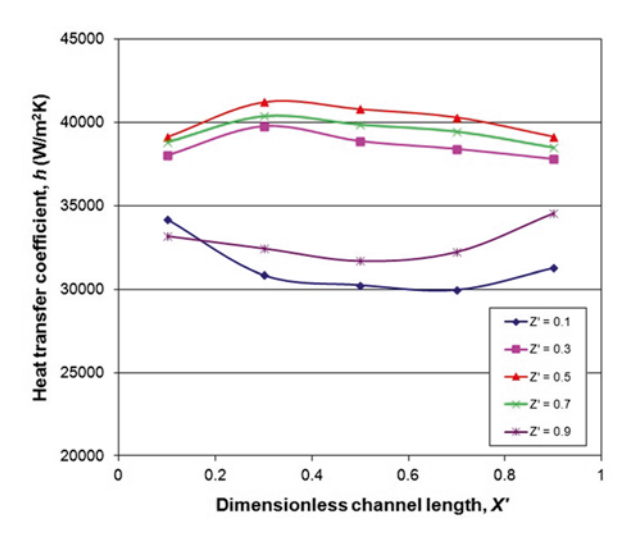


Figure 2.33 plots the local averaged heat transfer coefficients of the oblique fin microchannel heat sink in the streamwise direction for various spanwise positions when Re=250. The centre zone of the heat sink, Z'=0.5, shows the highest heat transfer coefficients, followed by Z'=0.7 and Z'=0.3. The heat transfer coefficients at both edges of the heat sink, Z'=0.1 and Z'=0.9, are significantly lower than the centre zones. The magnitude of secondary flow rate has a prominent effect to the heat transfer performance of the oblique fin microchannel heat sink and subsequently its temperature contour or profile.

Due to the fact that coolant mass flow rate in the main channels varies in both spanwise and streamwise direction, sensible heat gain by coolant results in different local coolant temperature rise as shown in Fig. 2.34. The highest coolant flow rate results in the lowest coolant temperature in Z' = 0.1, while the opposite is also true for Z' = 0.9. This might explain that the heat sink at zone Z' = 0.9 having higher wall temperature than zone Z' = 0.1 although both having comparable secondary flow rates, heat transfer coefficient and heat transfer area. Besides, the total heat transfer area of these two zones is ~5 % lower than the others due to the edge effect (thicker fin width at both edges), which might have also contributed to the elevated edge temperatures.

For the case Re=660, despite the unsteadiness in coolant flow, the bottom wall temperature of the heat sink is relatively consistent. Computed as an average temperature from 11 successive time steps, the maximum standard deviation of the heater temperatures is found at 0.15 °C. Figure 2.35 plots the area-weighted average heater temperature with the corresponding location on the heat sink. Compared with the average heater wall temperature profiles for low Reynolds number case shown in Fig. 2.36 where lowest coolant temperature occurs in Z'=0.1, heaters at both edges of the heat sink show higher wall temperature in the high Reynolds number case, which could be attributed to the severer flow migration. Subsequent heat transfer characteristics are also computed as an average of multiple time steps.

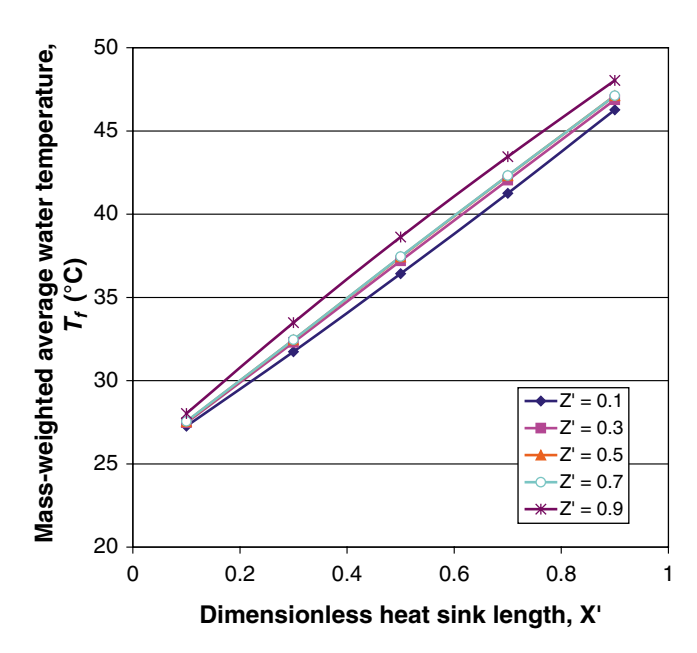


Fig. 2.34 Local coolant temperature in the oblique fin microchannel heat sink when Re = 250

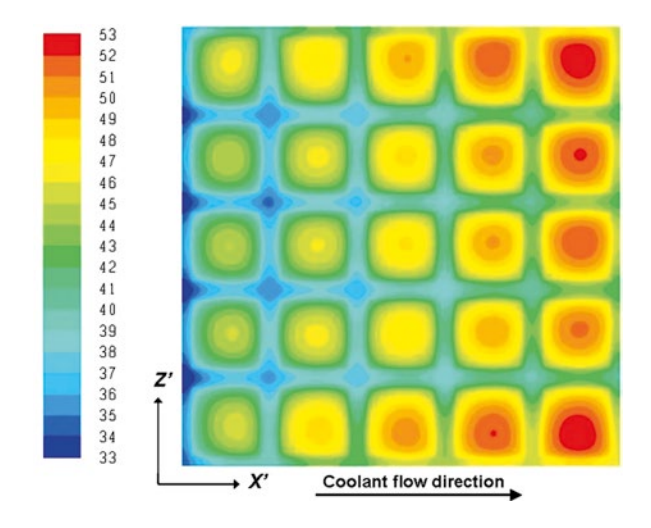


Fig. 2.35 Temperature contour (in $^{\circ}$ C) at the bottom wall of silicon-based oblique fin microchannel heat sink at Re=660

Local heat transfer coefficient is then computed, as shown in Fig. 2.37. Employing the oblique fin microchannel heat sink helps to keep a very uniform heat transfer coefficient throughout the heat sink, in contrast to the conventional microchannel, where convective heat transfer performance deteriorates in the streamwise direction

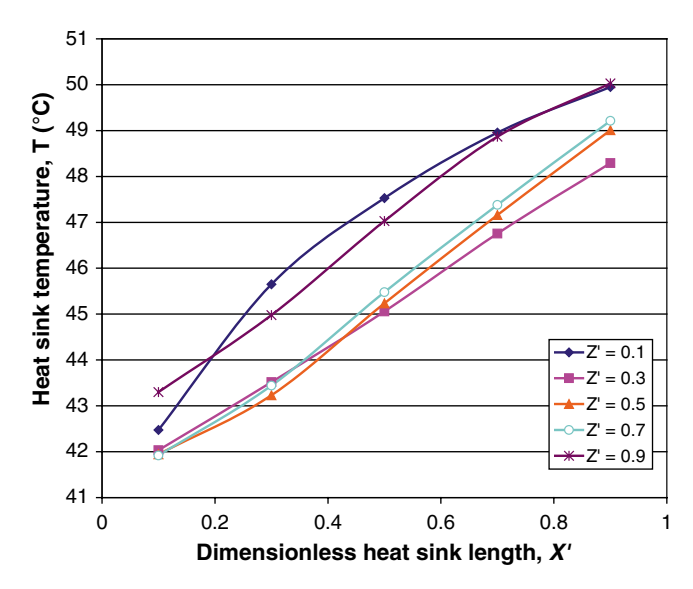


Fig. 2.36 Area-weighted average heater surface temperature when Re=660

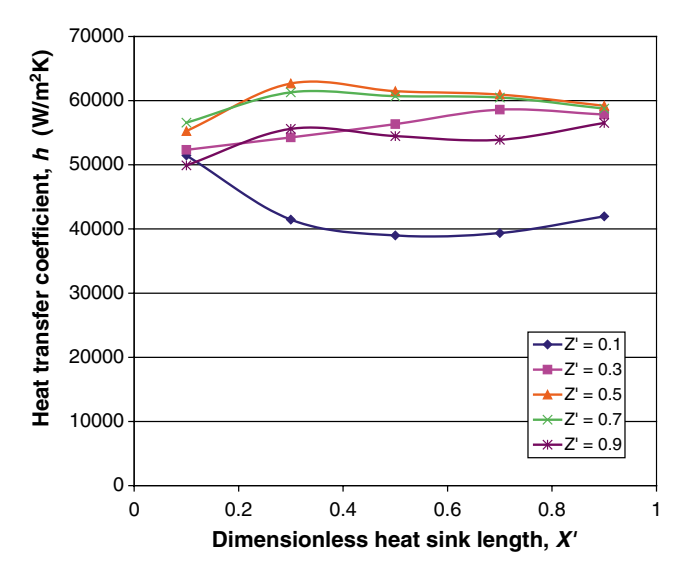


Fig. 2.37 Local heat transfer coefficients of oblique fin microchannel heat sink

due to boundary layer development [22]. Heat transfer coefficients for the oblique fin microchannel are kept within a narrow range for the high Reynolds number case, mostly between 50,000 and 60,000 W/m²K, which can be comparable to two-phase boiling process. Similar to the low Reynolds number case, heat sink edges Z' = 0.1

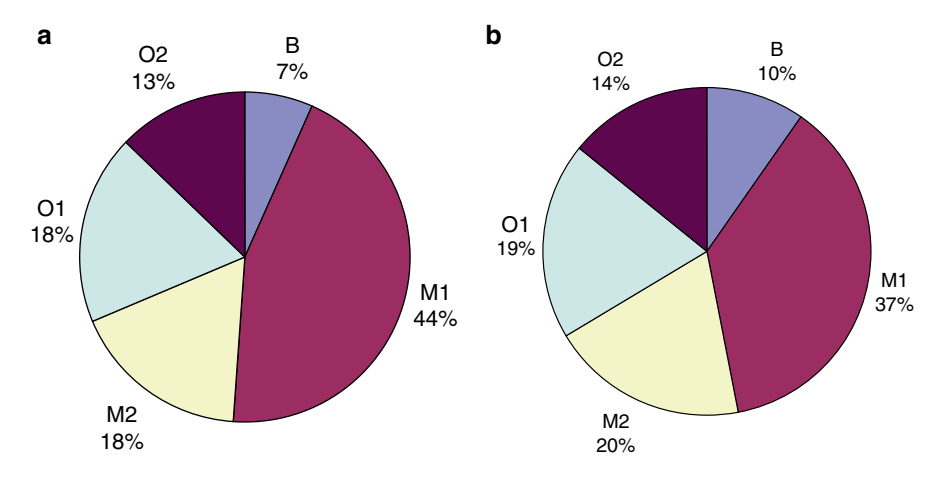


Fig. 2.38 Comparison of heat transfer rate between fin surfaces for (a) Re=250; (b) Re=660

still show lower heat transfer performance in comparison with the remaining part of the heat sink mainly due to significantly lower secondary flow generation. However, the local heat transfer performance in Z' = 0.9 is greatly enhanced due to the increased percentage of secondary flow rate.

The increment in Reynolds number elevates the secondary flow rate in oblique channels, affecting velocity profiles and subsequently heat transfer performance of each fin surface. Figure 2.38 compares the heat dissipation of each fin surface two cases considered in the study. Increment in secondary flow rate reduces the flow rate in the main channel. Thus, the effectiveness of fin surface M1 in dissipating heat is reduced. Higher secondary flow rate in the oblique channel improves the heat transfer performance in the oblique channel, as reflected by the increment in heat dissipation through surface O1 and O2. Subsequently, when secondary flow is injected to the adjacent main channel, higher fluid momentum thins the boundary layer at surface M2 further and improve the heat transfer of this fin surface.

2.4 Experimental Investigation: Average Performance

Simulation studies in the previous sections present a clear picture of the fluid flow characteristics and the heat transfer mechanism in the enhanced microchannel heat sink and the projected heat transfer augmentation. The focus of this section is shifted towards experimental investigation of the proposed heat transfer augmentation technique, using copper-based microchannel heat sinks. Both enhanced microchannel heat sinks of different materials and length scales demonstrate significant heat transfer improvement with negligible pressure drop up to a reasonably high Reynolds number (Re=400–500). The experiment also results in good agreement with the simulation predictions, validating the simulation model [23].

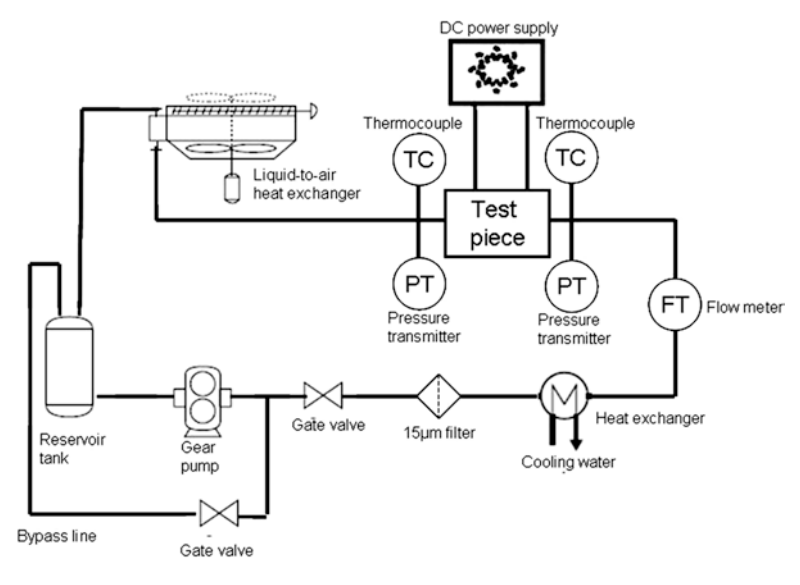


Fig. 2.39 Schematic for experimental flow loop [23]

2.4.1 Experimental Set-Up and Procedure

A schematic of the experimental flow loop is shown in Fig. 2.39. Deionized water from a reservoir tank is driven through the flow loop using a micro-annular gear pump. This pump forces the coolant through a 15 μ m filter and a flow meter before entering the microchannel test section. A heat exchanger (connected to water bath) is used to regulate the water temperature before coolant enters the test section. Pressure transmitters are attached to the manifolds immediately before and after the test piece to measure the pressure drop across the test section. The water temperatures immediately before, $T_{f,in}$, and after, $T_{f,out}$, the microchannel heat sink in the manifolds are also measured with two T-type thermocouples (copper—constantan). Heated water that exits the test section is cooled by passing it through a liquid-to-air heat exchanger before it returns to the reservoir tank.

After the test section is assembled and properly sealed, the gear pump is switched on and the desired flow rate through the flow loop is controlled with the digital control on the gear pump. As the flow rate is stabilized, the power supply to the heaters is switched on, and steady state is usually reached in 30–45 min. The power input to the heaters in the test piece is controlled by a DC power supply unit. The voltage across the heaters is measured directly, while the high current through the heaters is calculated from Ohm's law based on the voltage measured across a shunt resistor that is connected in series with the heater. Input power to the heaters is calculated as the product of measured voltage and calculated current. Steady-state readings from the thermocouples, differential pressure transmitter and others are recorded by data logger and stored in a computer throughout the duration of the experiment. Each steady state value was calculated based on the average of 100 readings sampled at 0.1 Hz.

Two sets of copper-based microchannel heat sinks with nominal main channel width of 300 and 500 μ m are included in the experimental studies. The measured geometrical dimensions for both sets of microchannel heat sinks are provided in Tables 2.3 and 2.4. In order to facilitate a fair performance comparison, both heat sinks are fabricated to a comparable channel aspect ratio, channel width, fin width and overall footprint. Measurement is performed with a 3-axis measurement microscope with 200× magnification at nine different points (3×3 grid) on the microchannel heat sink.

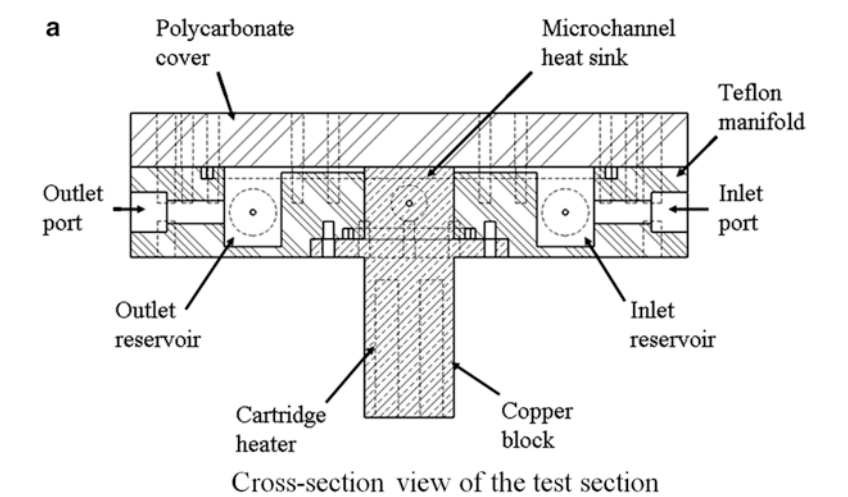
Details of the microchannel test section are shown in Fig. 2.40. The test section consists of a copper block, a Teflon manifold and a polycarbonate lid. The heat sink is machined from a square copper block of dimensions 25 mm×25 mm×70 mm. Microchannels are cut into the top surface by wire cutting, and the average surface roughness (Ra) measured using a white light interferometer surface profiler at the bottom wall of the channel is 1.81 μm. Holes are drilled into the bottom of the copper

Table 2.3 Dimensional details for microchannel heat sinks (300 um nominal channel wid	Table 2.3	Dimensional details	for microchannel b	neat sinks (300	um nominal channel width
--	-----------	---------------------	--------------------	-----------------	--------------------------

Characteristic	Conventional microchannel	Enhanced microchannel
Material	Copper	
Footprint, width×length (mm)	25×25	
Number of fin row, n	39	
Main channel width, w_c (µm)	355.2	360.2
Fin width, W_w (μ m)	245.8	245.2
Channel depth, <i>H</i> (μm)	1,153.1	1,174.0
Aspect ratio, α	3.25	3.26
Number of fin per row	_	20
Oblique channel width, w_{ob} (µm)	_	210.2
Fin pitch, <i>p</i> (μm)	_	1,164.5
Fin length, <i>l</i> (μm)	_	725.1
Oblique angel, θ (°)	_	26.6

Table 2.4 Dimensional details for microchannel heat sinks (500 µm nominal channel width)

Characteristic	Conventional microchannel	Enhanced microchannel	
Material	Copper		
Footprint, width×length (mm)	25×25		
Number of fin row, n	22		
Main channel width, w_c (µm)	547.0	539.3	
Fin width, <i>w</i> _w (μm)	458.5	465.2	
Channel depth, H (μ m)	1,482.2	1,487.1	
Aspect ratio, α	2.71	2.76	
Number of fin per row	_	12	
Oblique channel width, w_{ob} (µm)	_	298.0	
Fin pitch, p (μm)	_	1,995.2	
Fin length, l (μm)	_	1,331.2	
Oblique angel, θ (°)	_	26.4	



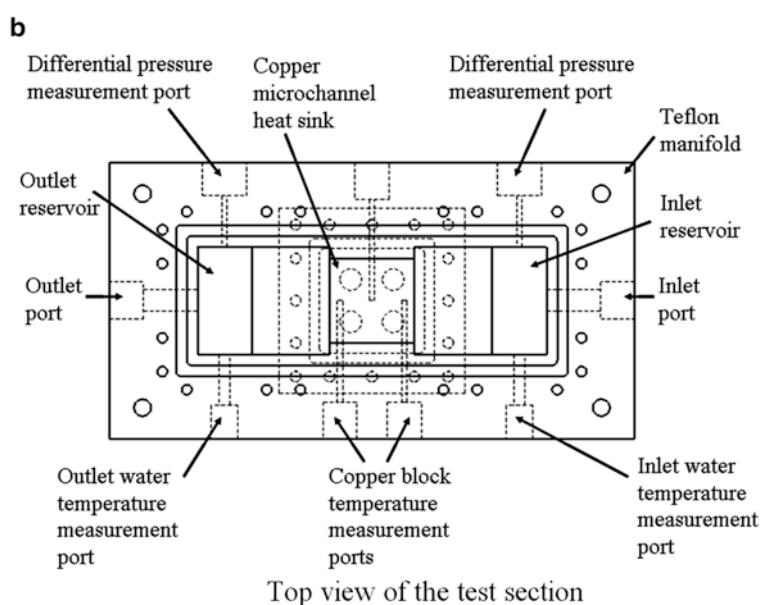


Fig. 2.40 Detailed drawings of the test section [23]. (a) Cross-section view of the test section. (b) Top view of the test section

block to accommodate four cartridge heaters that can provide a combined maximum power input of 1 kW. Three T-type (copper–constantan) thermocouple probes are positioned in the streamwise direction at a distance of 10 mm from the top surface of the copper block. The temperature readings from these thermocouple probes are extrapolated to provide an average bottom channel wall temperature of the heat sink.

This copper block is then mounted onto Teflon housing, where water tight seal (rubber O ring) is placed between the mating surfaces. The top surface of the copper

block and Teflon manifold is then sealed with the polycarbonate cover. A thin layer of silicone rubber (250 μ m) is laid between the microchannel heat sink and polycarbonate cover to ensure proper sealing.

The sensible heat gained by the coolant is determined from an energy balance:

$$q = \rho c_p Q \left(T_{f, \text{out}} - T_{f, \text{in}} \right) \tag{2.20}$$

It is found that more than 95 % of the heat input is transferred to the coolant across all the experimental runs, where the heat loss is deemed minimum or negligible. The heat flux into the test vehicles is calculated as the sensible heat gain into coolant over the area of copper block. An average heat flux at 100 W/cm² is maintained throughout the experiments for the copper-based microchannel heat sinks with 300 μm nominal channel width, while lower heat flux level at 65 W/cm² is supplied into heat sink with 500 μm nominal channel width in order to have the flow condition maintained in single phase flow throughout the experiment.

The average heat transfer coefficient can be then determined using the correlation:

$$h = \frac{q}{A_{\text{tot}} \left(T_{w} - T_{f,\text{ave}} \right)}$$
 (2.21)

where A_{tot} is total area of convective heat transfer surfaces. For conventional microchannel heat sink, total heat transfer area is evaluated as

$$A_{\text{tot}} = (N+1)L(w_{\text{ch}} + 2\eta H)$$
 (2.22)

On the other hand, total area of heat transfer for oblique finned microchannel heat sink is calculated as

$$A_{\text{tot}} = A_b + \eta A_{\text{fin}} \tag{2.23}$$

where A_b is the unfinned surface area at the bottom of the channels and $A_{\rm fin}$ is fin area.

 A_b = (Heat sink base area) – (Base area occupied by oblique fins)

$$A_b = WL - Nw_w l (2.24)$$

$$A_{\rm fin} = NHP \tag{2.25}$$

For microchannel configuration, fin efficiency is used to account for the drop in temperature along the fin. An adiabatic fin tip condition is assumed due to the insulative material of the manifold cover, and the corresponding fin efficiency is given as

$$\eta = \frac{\tan h \left(mH \right)}{mH} \tag{2.26}$$

where
$$m = \sqrt{\frac{hP}{k_{HS}A_c}}$$

As direct wall temperature measurement at the bottom of channel is not available, extrapolation from the temperatures measured by the thermocouples in the copper heat sink is performed by assuming 1-D heat conduction:

$$T_{w} = T_{HS} - \frac{sq''}{k_{uc}} \tag{2.27}$$

HS denotes heat sink. On the other hand, $T_{f,ave}$ is the average fluid temperature.

The corresponding Nusselt number is then calculated as $Nu = \frac{hD_h}{k_f}$, where D_h is

the hydraulic diameter of the channel and k_f is the thermal conductivity of water.

Total thermal resistance of the heat sink is defined as

$$R_{\text{tot}} = \frac{T_{\text{max}} - T_{f,\text{in}}}{a} \tag{2.28}$$

where T_{max} is the maximum measured temperature of the heat sink, T_f is the inlet coolant temperature and q is the heat supplied into the heat sink.

As for material properties, copper is assumed to have constant thermal conductivity, k_{cu} =387.6 W/mK. The density, specific heat capacity, thermal conductivity and dynamic viscosity of water are evaluated at the mean fluid temperature (average of the fluid inlet and outlet temperatures) based on the formulas stated in the previous section.

As the pressure transmitters are located at the manifolds, the pressure drop measurement represents the combined losses due to the frictional loss in microchannels and minor losses due to abrupt contraction and expansion at the inlet and outlet [24], which can be written as follows:

$$\Delta P = \Delta P_{c1} + \Delta P_{c2} + \Delta P_{ch} + \Delta P_{e2} + \Delta P_{e1}$$
 (2.29)

The pressure drop across microchannel can then be calculated as

$$\Delta P_{ch} = \Delta P - \left(\Delta P_{c1} + \Delta P_{c2} + \Delta P_{e2} + \Delta P_{e1}\right)$$

where ΔP_{c1} and ΔP_{c2} are the contraction pressure losses from the deep plenum to the shallow plenum and from the shallow plenum to the microchannel. These minor losses can be expressed as [25]

$$\Delta P_{c1} = \frac{1}{2} \rho_f \left(u_{p2,\text{in}}^2 - u_{p1,\text{in}}^2 \right) + \frac{K_{c1}}{2} \rho_f u_{p2,\text{in}}^2$$
 (2.30)

$$\Delta P_{c2} = \frac{1}{2} \rho_f \left(u_{\rm in}^2 - u_{p2,\rm in}^2 \right) + \frac{K_{c2}}{2} \rho_f u_{\rm in}^2$$
 (2.31)

where p1 and p2 denote the deep plenum and shallow plenum, respectively and K_{c1} and K_{c2} are the loss coefficients for the abrupt contractions. On the other hand, ΔP_{e2} and ΔP_{e1} express the pressure losses from the microchannel to the shallow plenum and from the shallow plenum to the deep plenum, which can be written as follows:

$$\Delta P_{e2} = \frac{1}{2} \rho_f \left(u_{p2,\text{out}}^2 - u_{\text{out}}^2 \right) + \frac{K_{e2}}{2} \rho_f u_{\text{out}}^2$$
 (2.32)

$$\Delta P_{e1} = \frac{1}{2} \rho_f \left(u_{p1,\text{out}}^2 - u_{p2,\text{out}}^2 \right) + \frac{K_{e1}}{2} \rho_f u_{p2,\text{out}}^2$$
 (2.33)

where K_{e1} and K_{e2} represent the loss coefficients due to the abrupt expansion. For the present heat sink test section geometry, the value of K_{c1} , K_{c2} , K_{e1} and K_{e2} is close to unity.

The associated friction factor is given by

$$f = \frac{\Delta P_{ch} D_h}{2\rho u_m^2 L} \tag{2.34}$$

The experimental investigation on heat sinks with 500 μ m channel width is conducted over the flow rates ranging from 375 to 950 mL/min, which correspond to Reynolds numbers of 325–780. Similar coolant flow rate was applied for heat sinks with 300 μ m channel width resulting Reynolds numbers from 260 to 640. Using $L/ReD_h > 0.05$ and $L/ReD_h > 0.05$ as the criteria for fully developed flow, all the data points fall into the thermally developing regime.

2.4.2 Microchannel Heat Sinks with 500 µm Nominal Channel Width

Figure 2.41 plots the average Nusselt number to Reynolds number for both conventional and enhanced microchannel heat sinks. Generally, the average Nusselt number for both configurations increases with Reynolds number as the thermal boundary layer thickness decreases with the increased fluid velocity. However, the heat transfer for the enhanced microchannel with oblique fins is significantly higher compared with conventional microchannel heat sink. At the lowest Reynolds number of 325, the average Nusselt number is increased by 57 %, from 9.1 to 14.3. This appreciable enhancement in heat transfer is due to the combined effects of thermal boundary layer redevelopment at the leading edge of each oblique fin and the secondary flows generated by flow diversion through the oblique channels. The current experimental results are in accordance with the findings from the simulation presented in the previous chapters.

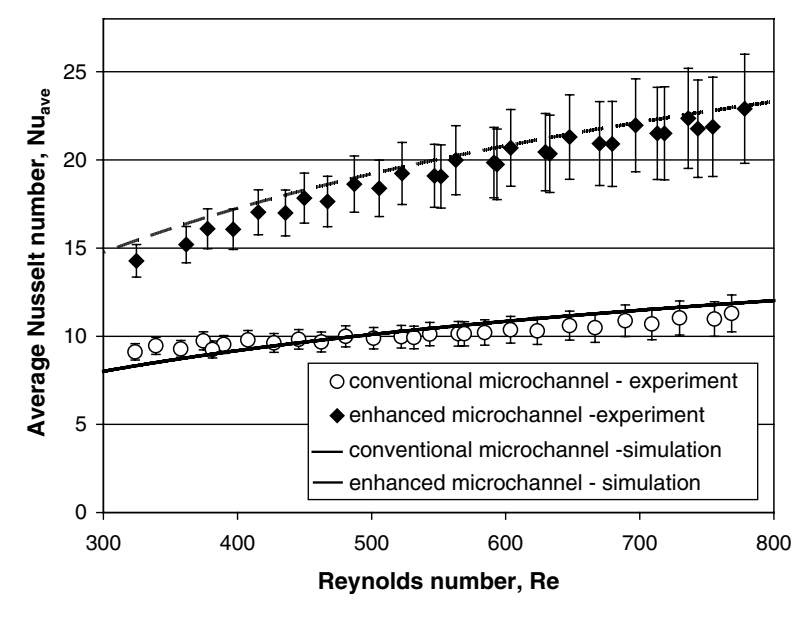


Fig. 2.41 Comparison of average Nusselt number for microchannel heat sinks (500 μ m nominal channel width) [23]

The percentage of heat transfer augmentation is observed to increase with Reynolds number. A heat transfer enhancement of 103 % is achieved at the highest Reynolds number of 780, when the average Nusselt number increases from 11.3 to 22.9. As flow rate is increased, the water coolant would flow with a higher velocity through the channels. Coupled with higher percentage of flow diversion from the main channel into the oblique channel, the resultant secondary flows would carry the higher momentum and further disrupt the thermal boundary layer development and better mix the fluid leading to higher heat transfer enhancement at larger Reynolds number. Besides experimental data, simulation results of both conventional and enhanced microchannel are plotted in Fig. 2.41 for comparison purpose. These simulations adopt the simplified model proposed in Sect. 2.2. Only a pair of fin-channel is simulated for both enhanced microchannel and conventional microchannel configurations, where the spanwise repeating channels/ fins are represented by either periodic or symmetry boundary condition. In fact, the simulation predictions are in good agreement with the experimental results, for both conventional and enhanced microchannel. It is noticed that all the experimental data falls within ±10 % of the predicted value, thus demonstrating the ability of the numerical models to predict the heat transfer performance especially for the enhanced microchannel heat sink, which adopted the simplified periodic boundary condition.

For predicting the heat transfer performance for louvred fin heat exchanger under constant heat flux condition, Aoki et al. [6] proposed an empirical correlation as below.

$$Nu_{ave} = 0.87 Re_L^{0.5} Pr^{1/3}$$
 (2.35)

This correlation yields an average Nusselt number that is merely 4 % lower than the Pohlhausen solution for laminar flow over a flat plate with constant heat flux. When this correlation is used on oblique finned microchannel heat sink, it over-predicts the heat transfer coefficient by averagely 44 %. Drastically different flow field between louvred fin heat exchanger and oblique finned microchannel heat sink is believed to be the source of discrepancy. As discussed in the previous sections, heat transfer efficiency through each oblique fin surface is significantly different from each other due to the asymmetrical coolant velocity and temperature profiles. In addition, the applicability of Pohlhausen solution in louvred fin heat exchanger shows that boundary layers are totally renewed at each louvre. The large distance between louvres promotes the thermal wake dissipation in the louvred fin heat exchanger [26], while oblique fins are closely packed and the wake dissipation is incomplete over the short wake length.

The experimental pressure drop data across microchannel heat sinks is presented in Fig. 2.42, alongside the simulation results, again showing very good agreement. It is interesting to note that the pressure drop across the enhanced microchannel is comparable to conventional microchannel for a Reynolds number below 400.

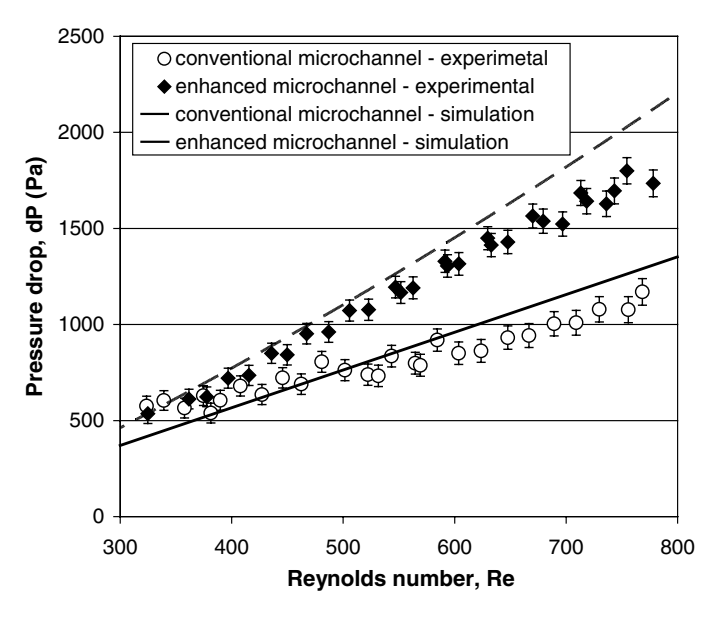


Fig. 2.42 Comparison of pressure drop across microchannel heat sinks (500 μ m nominal channel width) [23]

This suggests that the enhanced heat transfer can be achieved without incurring excessive pressure drop penalty. This phenomenon is possible due to the competing effects of the increased pressure drops (due to thinning of boundary layers and boundary layer separation) and pressure recoveries (due to flow bifurcations) [14]. However, as the Reynolds number increases beyond 400, a greater amount of the flow will be diverted into the oblique channels. This creates secondary flows with stronger momentum, which further augment the heat transfer but incur some pressure drop penalty. The pressure drop penalty, however, is small compared to the heat transfer enhancement factor.

Heat transfer enhancement factor (E_{Nu}) and pressure drop penalty (E_f) are defined as the average Nusselt number and friction factor of the present enhanced microchannels divided by that of conventional straight channels, respectively [27]. Similar performance factor was adopted by Sui et al. [28]. From Fig. 2.43, the advantage of oblique finned microchannel is clearly revealed where the heat transfer enhancement factor outweighs the pressure drop penalty. When pressure drop penalty is close to 1 (no additional pressure drop incurred), the heat transfer performance (in terms of Nusselt number) of the oblique finned microchannels is 50–60 % more than that of conventional microchannels. As the Reynolds number increases, the heat transfer enhancement factor may exceed 2 (100 % improvement) while incurring a smaller pressure drop penalty of 40–60 %. However, it should be noted that the magnitude of pressure drop penalty is less than 1 kPa, which is relatively low and should be manageable with the same pump.

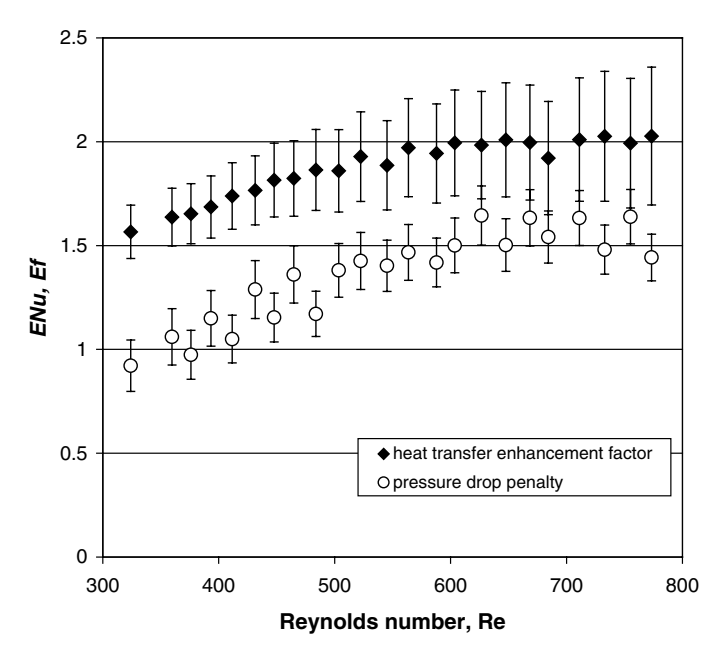


Fig. 2.43 Comparison of heat transfer enhancement factor and pressure drop penalty (500 μ m nominal channel width) [23]

2.4.3 Microchannel Heat Sink with 300 µm Nominal Channel Width

Experiment investigation into heat sinks with smaller nominal channel and fin width at 300 µm also indicates significant heat transfer augmentation. This shows the applicability of the proposed heat transfer enhancement technique on heat sinks with different fin-channel size, both larger and smaller fin-channel size. A 77 % improvement is realized at Reynolds number as low as 260, where the average Nusselt number is elevated from 6.6 of the conventional microchannel to 11.7. The heat transfer performance of the enhanced microchannel by 111 % over the conventional configuration when the Reynolds number is raised to 650. Figures 2.44 and 2.45 show the comparison for Nusselt number and pressure drop between the conventional microchannel and enhanced microchannel, respectively.

Unfortunately, the results are confounded by the occurrence of bent/burr at the edge of oblique fins that points towards the main channel as displayed in Fig. 2.46. According to Joshi and Webb [29] in their study on offset strip-fin heat exchanger, the "burred edge" of fins could lead to 10--20~% increment in friction factor and also adversely affect the heat transfer. For future research, better fabrication technique has to be identified for microchannel heat sink with fin width less than $500~\mu m$ to reduce burr at the fin edge that could affect the performance of heat sink.

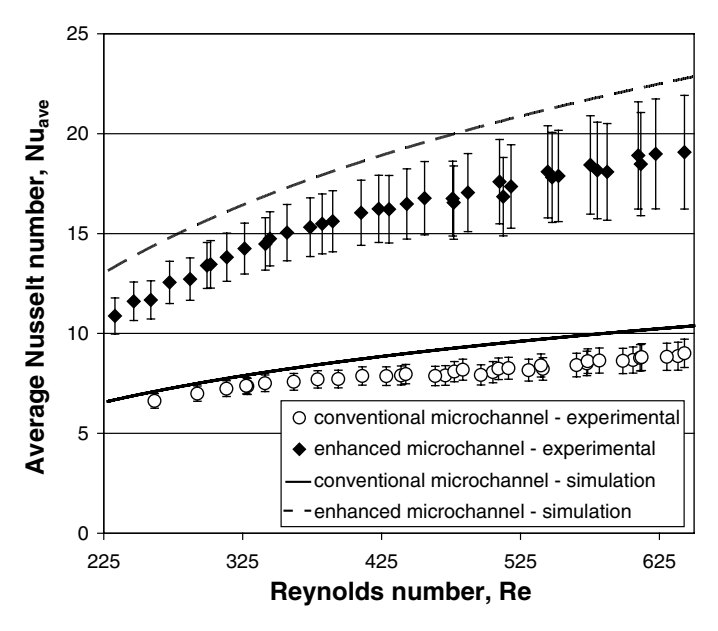


Fig. 2.44 Comparison of average Nusselt number for microchannel heat sinks (300 μ m nominal channel width) [23]

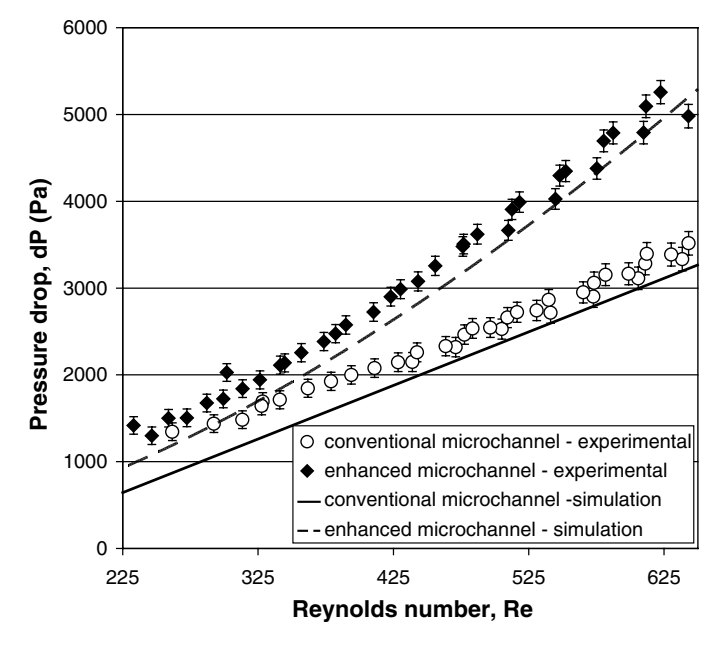


Fig. 2.45 Comparison of pressure drop across microchannel heat sinks (300 μ m nominal channel width) [23]

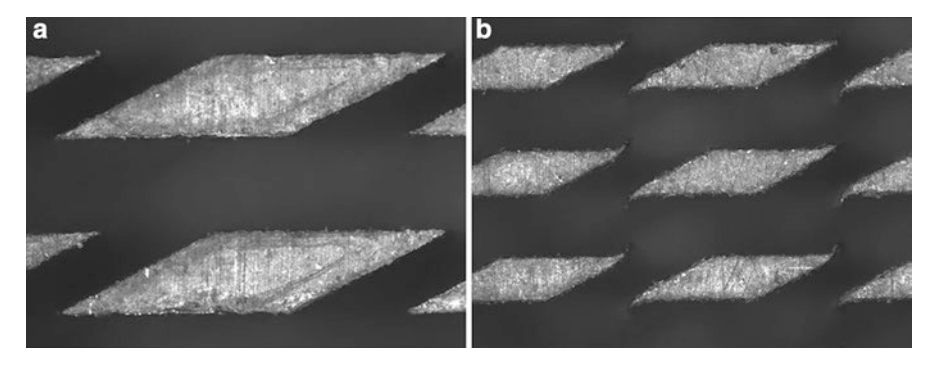


Fig. 2.46 Microscopic image of (a) enhanced microchannel heat sink with 500 μm nominal channel width (b) enhanced microchannel heat sink with 300 μm nominal channel width [23]

2.5 Experimental Investigation: Local Performance

The experimental investigation of copper-based oblique fin heat sink shows promising results. However in a recent review, Kandlikar et al. [30] observed that the heat transfer coefficients of these oblique finned copper microchannels were relatively low due to large hydraulic diameters and it will be interesting to see performance at smaller level [21].

2.5.1 Experimental Set-Up and Procedure

A similar set-up as used for the copper microchannel is used for the silicon-based microchannel heat sink. Here, silicon-based microchannel heat sinks are created on flip chip packages for experimental investigation. Channels are cut on the backside of the silicon thermal test chips using wafer dicing saw blades of different width. Measurement is performed with a 3-axis measurement microscope with 200× magnification at nine different points (3×3 grid) on the microchannel heat sink. The average surface roughness (Ra) measured at the bottom wall of the channel is 178 nm. Figure 2.47a displays the test section of microchannel heat sinks in this experiment. It consists of a polycarbonate manifold that is mounted onto a flip chip package, where the microchannels are laid. Each thermal test die is 0.1"×0.1" $(2.54 \text{ mm} \times 2.54 \text{ mm})$ in size and when diced in 5×5 grid array, this results in an overall footprint of 0.5" × 0.5" (12.7 mm × 12.7 mm) with 0.65 mm thickness for the current test vehicles. Each thermal test die has a heater (doped silicon well) at the bottom wall of the chip at 2 mm × 2 mm and a series of thermal sensors (five diodes connected in series), which enable independent heater control and local temperature measurement, providing greater insight into local heat transfer behaviour and the overall temperature mapping. The resistive heating of the silicon thermal test dies is accomplished by driving the current through the doped silicon well, where the input power is controlled by a DC power supply unit. Figure 2.47b, on the other hand, shows the test piece and the enlarged view of the 5×5 arrays of thermal test dies. A coordinate numbering scheme (X, Z) for thermal test dies identification is also indicated in the figure.

Temperatures on the thermal test chip are indicated as voltage drop across the thermal diode sensors. Prior to the experiment, the voltage-temperature response of these thermal diode sensors are established through calibration. The calibration is performed in a convection oven from 30 to 90 °C, in steps of 10 °C. Temperatures and voltage drop are then recorded when both temperatures of oven and thermal sensors reach steady state, typically in an hour time.

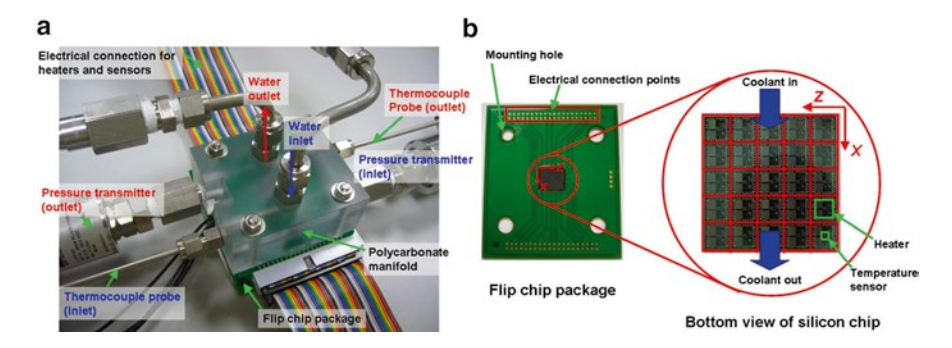


Fig. 2.47 (a) Microchannel test section; (b) test piece with 5×5 array of thermal test dies

2.5.2 Silicon-Based Microchannel Heat Sink with 100 µm Nominal Channel Width

The experiments are conducted over the flow rates ranging from 100 to 500 mL/min, which correspond to Reynolds numbers of 180–680. By employing silicon thermal test chip in these experiments, the local behaviour (local temperature and local heat transfer coefficient profiles) of the enhanced heat sink can be investigated. In this case, the performance of the enhanced microchannel heat sink with 100 μ m nominal width under the experimental conditions of 160 mL/min (Re=252) total coolant flow rate and total 273 W heater power of is presented.

The enhanced microchannel shows significant reduction in total thermal resistance compared to the conventional microchannel. The total thermal resistance comprises of conductive, spreading, convective and caloric thermal resistances. Generally, the conductive thermal resistance remains constant while spreading, convective and caloric thermal resistances reduce with the increasing Reynolds number, resulting in lower total thermal resistance. The improved heat transfer performance of the enhanced microchannel is demonstrated in Fig. 2.48, where the total thermal resistance of the enhanced microchannel heat sink is consistently lower than the conventional configuration in the range of Reynolds numbers studied. At low Reynolds number ~180, the total thermal resistance of the enhanced microchannel is 3 % (R_{tot} =0.234 °C/W) lower than that of the conventional microchannel (R_{tot} =0.242 °C/W). As Reynolds number rises, the effectiveness of enhanced microchannel increases, and the percentage of reduction in total thermal resistance quickly increases. The maximum total thermal resistance reduction achieved at Reynolds number ~690 is as much as 25 % (R_{tot,EM}=0.089 °C/W versus $R_{\text{tot},CM}$ = 0.119 °C/W). In the context of current experiment, the highest percentage of

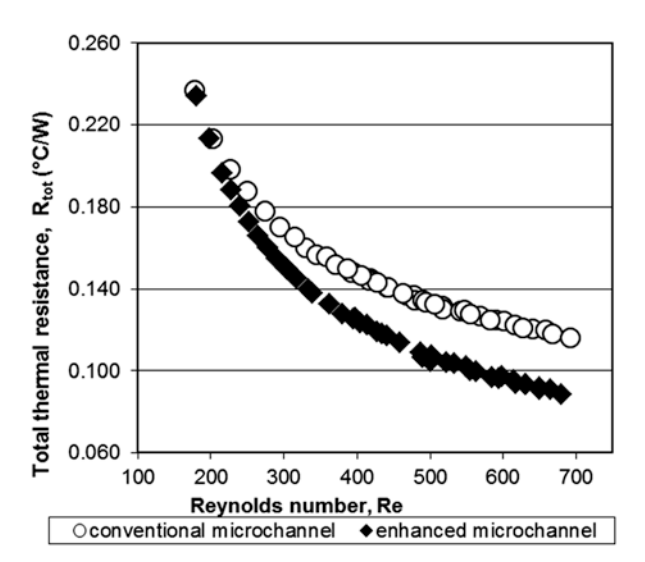


Fig. 2.48 Comparison of total thermal resistance between the microchannel heat sinks

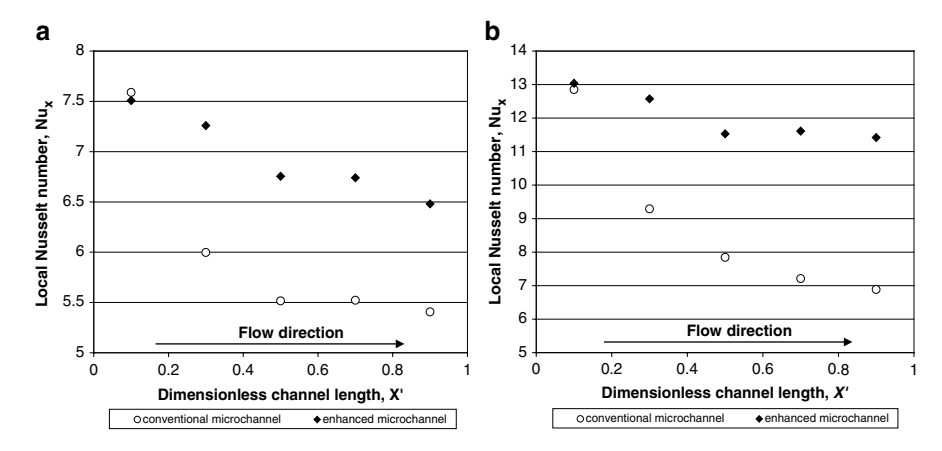


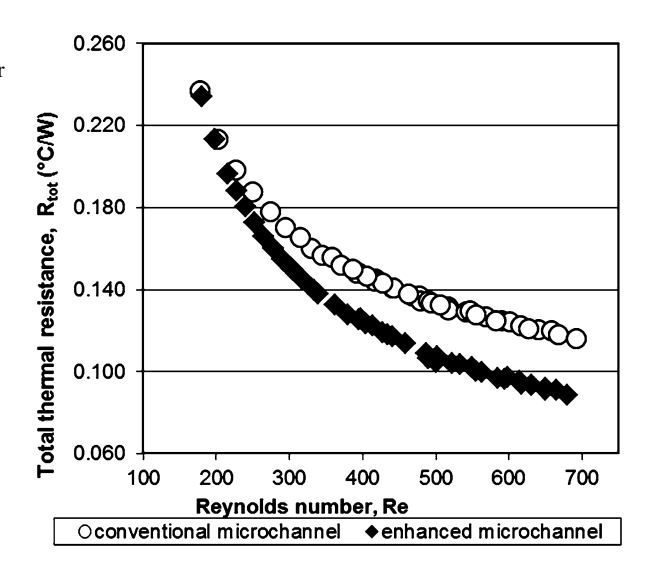
Fig. 2.49 Comparison of local heat transfer performance of microchannel heat sinks for (a) Re ~250; (b) Re ~680

total thermal resistance reduction translates to an 8.1 °C lower in maximum chip temperature for the enhanced microchannel heat sink ($T_{\text{max},EM}$ =50.5 °C versus $T_{\text{max},CM}$ =58.6 °C).

As discussed, the introduction of oblique fins and channels leads to a much uniform heat removal capability across the microchannel heat sink. Figure 2.49a, b illustrates the comparison of local heat transfer performance of microchannel heat sinks for two of the experimental runs at Re ~250 and Re ~680. The markers denote the location of thermal diode sensors on the silicon test chip in the streamwise direction, where the temperature measurement is made. It is noticed that both conventional and enhanced microchannel heat sinks display a relatively close Nusselt number at the upstream of the heat sink, X' = 0.1 when the boundary layers are thin. The distinguishing point for these two heat sinks is the development of the flow regime and boundary layers as coolant travels downstream. As boundary layers continue to thicken with the flow distance, heat transfer performance of the conventional microchannel deteriorates rapidly, as showed in the figures for both Reynolds number cases. A maximum 48 % drop in Nusselt number is observed between X' = 0.1and X' = 0.9, resulting in a highly non-uniform heat transfer performance within the heat sink. Instead of declining, the enhanced microchannel keeps the Nusselt number at a much elevated level and consistent across the enhanced microchannel heat sink. The profile of the streamwise local Nusselt number is very uniform, confined to a narrow range of 7.0-8.2 and 12.4-14.4 for both Reynolds number cases, respectively, from the inlet of the microchannel to its outlet. This phenomenon is highly due to the frequent re-initialization of thermal boundary layers and generation of secondary flows. This combination ensures that the flow is in a constant state of development thus having a sustainable performance close to that of the flow upstream.

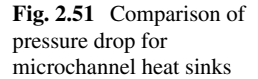
The average heat transfer performance of the microchannel heat sinks is plotted in Fig. 2.50. Generally, the average Nusselt number, Nu_{ave}, increases with Reynolds

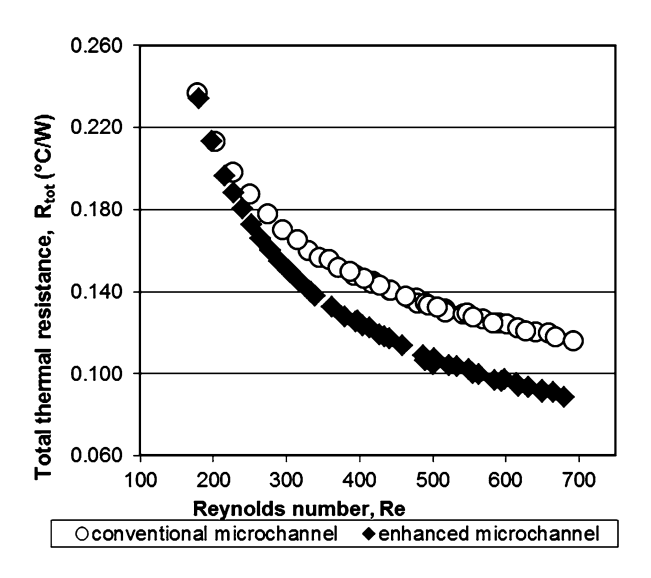
Fig. 2.50 Comparison of heat transfer performance for microchannel heat sinks



number as the thermal boundary layer thickness decreases with the increased fluid velocity. However, the heat transfer for the enhanced microchannel with oblique fins is highly augmented in comparison with conventional microchannel heat sink. At Reynolds number ~180, the average Nusselt number of the enhanced microchannel is 15 % higher than that of conventional microchannel. As Reynolds number rises, the Nusselt number increases by almost 47 %, from 9.0 to 13.2. The appreciable enhancement in heat transfer is due to the combined effects of thermal boundary layer redevelopment at the leading edge of each oblique fin and the secondary flows generated by flow diversion through the oblique channels. As the flow rate induced through the heat sink is increased, more fluid is diverted from the main channel into the oblique channel. This secondary flow thus carries higher momentum and further disrupts the boundary layers development and augments the heat transfer.

Nevertheless, the most interesting feature of the enhanced microchannel heat sink is that the significant heat transfer augmentation is achieved with small pressure drop penalty. The enhanced microchannel heat sink, which employs secondary flow to enhance its heat transfer, still managed a comparable pressure drop with the conventional microchannel heat sink for Reynolds number lower than 500, as displayed in Fig. 2.51. This distinguishes the proposed scheme from the conventional heat transfer enhancement scheme, where trade-off in terms of pressure drop penalty is inevitable. As the Reynolds number increases, a higher percentage of coolant will be diverted into oblique channels. This creates a secondary flow with stronger momentum, which further augments the heat transfer but incurs additional pressure drop penalty. Therefore, the pressure drop for enhanced microchannel starts to deviate and increases more than the conventional configuration. However, the magnitude of increment of pressure drop is considered manageable for the same micropump.





2.5.3 Parametric Study

There are a few key design parameters that greatly influence the heat transfer and pressure drop performance in oblique finned microchannels. As these parameters vary, the overall fin layout will change. This change has an enormous effect on the flow field and consequently it affects the performance of the heat sink. Therefore, a parametric study is essential to explore the outcome of varying these parameters. The two critical design parameters identified for the parametric study are oblique angle and oblique fin pitch. A total of seven configurations with three oblique angles $(15^{\circ}, 27^{\circ} \text{ and } 45^{\circ})$ coupling with three fin pitches $(400, 800 \text{ and } 1,500 \,\mu\text{m})$ are fabricated on silicon-based microchannel heat sink for the performance evaluation. The benchmarking is based on two conventional microchannel configurations, which have $100 \text{ and } 200 \,\mu\text{m}$ nominal channel width, respectively. Detailed dimensions of various microchannel heat sinks are tabulated in Tables 2.5 and 2.6. Microchannel heat sinks with a similar channel width, fin pitch but different oblique angles are grouped together to compare the effect of oblique angle variation, and it is vice versa when evaluating the effect of fin pitch variation.

While the combination of a different oblique angle and pitch can result in a wholly new enhanced microchannel heat sink layout, it also redistributes the fin and un-finned surface areas available for convective heat transfer. Table 2.7 compares the fin, un-finned and total surface areas available for convective heat transfer of different microchannel configurations. From Table 2.7, it is clear that the introduction of oblique fins and channels in microchannel heat sink increases the total heat transfer area by 5–30 % with smaller fin pitch and oblique angle leading to larger surface areas.

Characteristic	Conventional microchannel #1 (Con-100)	Enhanced microchannel #1 (27°—NP')	Enhanced microchannel #2 (45°—NP')
Material	Silicon		
Footprint, width × length (mm ²)	12.7×12.7		
Number of fin row, n	61		
Main channel width, w_c (µm)	115	113	110
Fin width, w_w (μ m)	85	87	91
Channel depth, <i>H</i> (μm)	387	379	351
Aspect ratio, α	3.37	3.35	3.19
Oblique channel width, w_{ob} (µm)	_	49	48
Fin pitch, <i>p</i> (μm)	_	405	400
Fin length, <i>l</i> (μm)	_	292	332
Oblique angel, θ (°)	_	26.3	45.0

Table 2.5 Dimensional details of microchannel heat sinks with 100 μm channel width

2.5.3.1 The Effect of Oblique Angle Variation

The effect of a change in oblique angle to heat transfer, and pressure drop performance, is diagnosed with three groups of microchannel heat sinks. The first group is three microchannel heat sinks with 100 µm nominal channel width, which consists of a conventional straight channel heat sink (Con-100) as benchmark and two enhanced heat sinks (~400 μm nominal fin pitch) with 27° and 45° oblique angles, respectively (27°—NP' and 45°—NP'). The experimental results of both heat transfer and pressure drop are presented in Fig. 2.52. Figure 2.52a compares the average Nusselt number of three microchannel heat sinks. It is observed that the average Nusselt numbers of Con-100 and 45°—NP' almost overlap each other, while that of 27°—NP' is significantly higher. This suggests that 45°—NP' is not as effective as 27°-NP' in augmenting heat transfer performance. In contrast, the heat transfer augmentation for 27°-NP' rises with Reynolds number. On the other hand, the pressure drop across Con-100 and 45°—NP' overlaps each other as they did in the Nusselt number plot, as shown in Fig. 2.52b. The 27°—NP' also displays a pressure drop that is comparable to the other two for Reynolds numbers lower than 500, signalling that the heat transfer enhancement can be achieved with negligible pressure drop penalty.

The second group of microchannel heat sinks for comparison has the same features as the first group, with exception that they are 200 µm in nominal channel width. In this group, conventional microchannel (Con-200) is adopted as the baseline for comparison with two enhanced microchannel heat sinks (~800 µm nominal fin pitch) with 27° and 45° oblique angles, respectively (27°—NP and 45°—NP). A similar trend is observed from the heat transfer and pressure drop performance of

⁻NP' denotes nominal pitch (~400 μm) for enhanced microchannel heat sink with 100 μm channel width

m channel width
_
0
2
Ö
with
-=
≥
×
_
. =
-
heat
7
icrochann
8
of 1
letails
0
Dimensional details of microchannel heat sinks
Ξ
\Box
9
able 2.6
-
~
9
ೌ

	Conventional	Enhanced	Enhanced	Enhanced	Enhanced	Enhanced
Characteristic	microchannel #2 (Con-200)	microchannel #3 (27°—NP)	microchannel #4 (45°—NP)	microchannel #5 (15°—LP)	microchannel #6 (27°—LP)	microchannel #7 (45°—SP)
Material	Silicon					
Footprint, width×length (mm ²)	12.7×12.7					
Number of fin row, n	30					
Main channel width, w_c (µm)	205	205	203	205	206	204
Fin width, w_w (μ m)	195	195	197	194	194	196
Channel depth, H (μm)	450	418	445	455	405	449
Aspect ratio, α	2.20	2.04	2.19	2.17	1.97	2.20
Oblique channel width, w_{ob} (µm)	I	104	103	101	103	103
Fin pitch, p (μ m)	I	783	800	1,502	1,536	400
Fin length, <i>l</i> (μm)	1	550	653	1,104	1,301	253
Oblique angel, θ (°)	I	27.1	45.0	14.9	26.3	45.0
000 / 1-7; 1-1;	pr 1	1	000 17.	1 144		

—NP denotes nominal pitch (~800 μm) for enhanced microchannel heat sink with 200 μm channel width —LP denotes large pitch (~1,500 µm) for enhanced microchannel heat sink with 200 µm channel width

⁻SP denotes small pitch (~400 µm) for enhanced microchannel heat sink with 200 µm channel width

Configuration	Oblique angle (°)	Fin pitch (µm)	Oblique fin perimeter (µm)	Fin area (mm²)	Un-finned area (mm²)	Total heat transfer area (mm²)
Con-100	_	_	_	609.5	90.6	700.1
27°—NP′	26.3	405	976.6	718.7	107.5	826.2
45°—NP′	45.0	400	919.8	635.6	98.1	733.7
Con-200	_	_	_	354.0	80.8	434.8
27°—NP	27.1	783	1,956.9	409.1	102.8	511.9
45°—NP	45.0	800	1,864.8	406.4	93.6	500.0
15°—LP	14.9	1,502	3,718.2	441.6	100.5	542.1
27°—LP	26.3	1,536	3,476.4	359.1	92.4	451.5
45°—SP	45.0	400	1,059.3	464.5	107.8	572.3

Table 2.7 Comparison of convective heat transfer areas for microchannel heat sinks

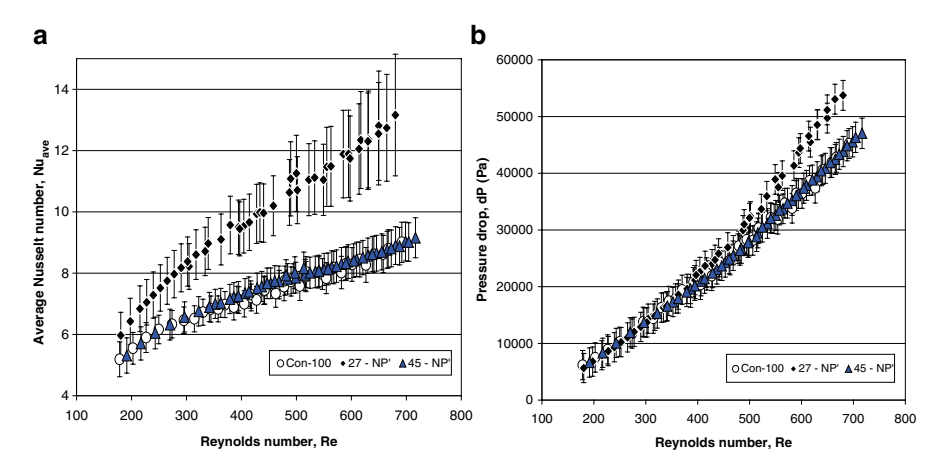


Fig. 2.52 Comparison of (a) average Nusselt number, (b) pressure drop for microchannel heat sinks with different oblique angles (100 μm nominal channel width and 400 μm nominal fin pitch)

this group, as displayed in Fig. 2.53 in comparison to the first group, which has 100 µm nominal channel width. Both Con-200 and 45°—NP result in comparable average Nusselt numbers and pressure drop for Reynolds number up to 1,000, while that of 27°—NP is consistently higher. This again indicates that smaller oblique angle is better for heat transfer enhancement. The gradient for 45°—NP in the average Nusselt number increases beyond Re 1,000, suggesting that this configuration can be more effective in heat transfer for higher Reynolds number.

From the assessment employing multiple microchannel groups, it is consistently demonstrated that a smaller oblique angle contributes to higher heat transfer performance, with a generally higher pressure drop. The smaller oblique angle results in lesser flow resistance than the larger oblique angle. Similar to liquid flow through a bend, loss coefficient increases for sharper bend as area of flow separation becomes extensive [23]. Thus, a smaller oblique angle helps to translate the diffusive oblique

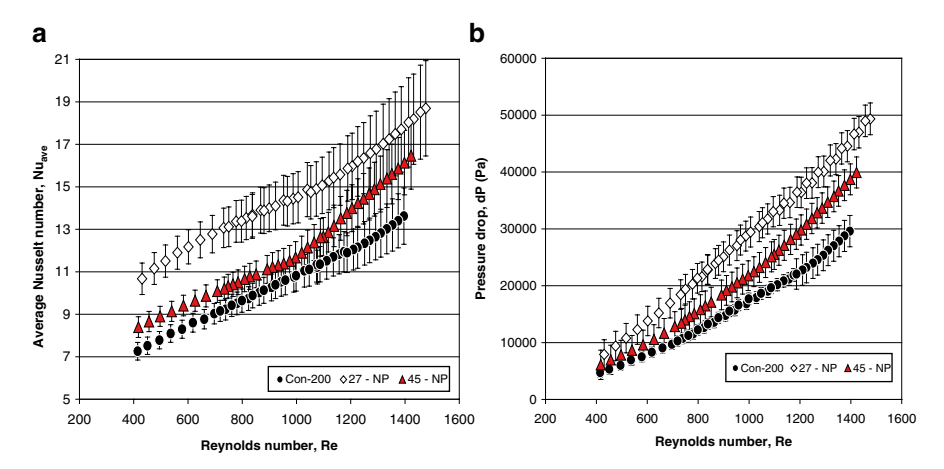


Fig. 2.53 Comparison of (a) average Nusselt number, (b) pressure drop for microchannel heat sinks with different oblique angles (200 μm nominal channel width and 800 μm nominal fin pitch)

channel into a smoother and smaller flow area expansion from the main channel. This can help to reduce the boundary layer separation that occurs in the oblique channel and increase the secondary flow generation. However, one should be aware that for a smaller oblique angle with similar fin pitch, oblique fins will become thinner, and this might compromise the structural integrity. In fact, the author has struggled to fabricate the enhanced microchannel heat sinks with 15° oblique angle through mechanical wafer cutting.

2.5.3.2 The Effect of Oblique Fin Pitch Variation

The impact of oblique fin pitch variation to the enhanced microchannel performance is evaluated in two groups of microchannel heat sinks, with 200 µm nominal channel width, by varying the oblique fin pitch while other parameters including oblique angle are fixed. The first group of microchannel heat sinks includes a conventional microchannel (Con-200) and two enhanced microchannel heat sinks (both have 27° oblique angle) with 800 and 1,500 μ m fin pitches, respectively (27°—NP and 27°—LP). The second group of microchannel heat sinks for comparison comprises of conventional microchannel (Con-200) and two enhanced microchannel heat sink (both have 45° oblique angle), with 400 and 800 μ m fin pitch (45° —SP and 45° —NP). The experimental heat transfer and pressure drop findings of the first group is presented in Fig. 2.54. The average Nusselt number is the highest for 27°—NP followed by 27°—LP while that of Con-200 is the lowest. It also suggests that the maximum temperature is lower than conventional microchannel. On the other hand, the pressure drop for 27°—NP is the highest while both 27°—LP and Con-200 display comparable pressure drop. This indicates that shorter fin pitch is beneficial for the heat transfer but incurs some pressure drop penalty.

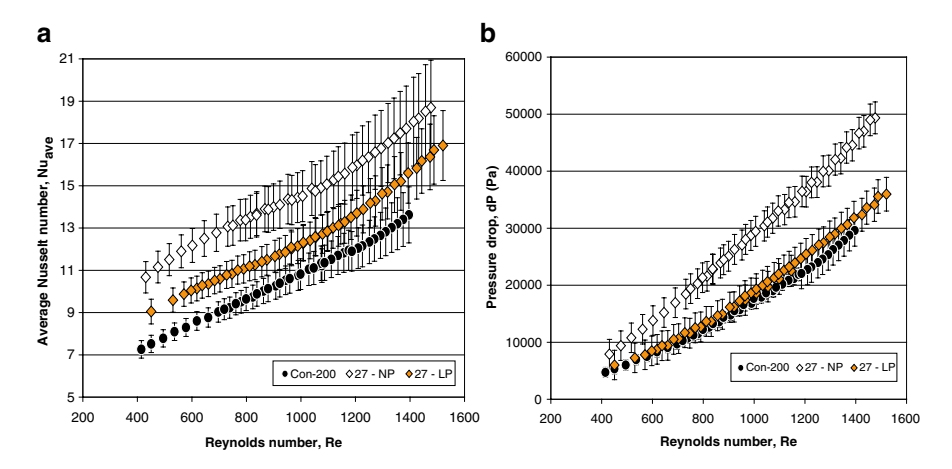


Fig. 2.54 Comparison of (a) average Nusselt number, (b) pressure drop for microchannel heat sinks (200 μm nominal channel width and 27° oblique angle) with different fin pitches

2.5.3.3 Overall Performance Comparison

Besides evaluating the heat transfer of microchannel heat sinks to the Reynolds number, the total thermal resistance of the individual heat sink is always compared between each other under the constant pressure drop and, also, pump power constraint, in the selection process to determine the best performing heat sink that meets the operating constraints. Figure 2.55 demonstrates the comparison of total thermal resistances of various microchannel heat sinks under the constraint of pressure drop. Among all the heat sinks tested, the enhanced microchannel with 100 μm channel width and 27° oblique channel (27°—NP') achieves the lowest total thermal resistance at the lowest pressure drop. This observation demonstrates the effectiveness of the enhanced microchannel through the integration of smaller channel size (hydraulic diameter) that has large surface area-to-volume ratio with short sectional oblique fins. For instance, the pressure drop that is required to achieve 0.119 °C/W employing conventional microchannel (Con-100) can be reduced by ~55 % (from 45 to 25 kPa) by adopting the enhanced microchannel (27°—NP').

A similar trend is observed for microchannel heat sinks with 200 μ m nominal channel width. 45°—SP and 15°—LP are the two microchannel configurations that record the lowest total thermal resistance, in comparison to other microchannel heat sinks with 200 μ m nominal channel width. This finding also points out the effectiveness of a smaller fin pitch and a smaller oblique angle in enhancing heat transfer performance. More importantly, these configurations perform better than conventional microchannel heat sink with 100 μ m nominal channel width at the similar pressure drop. By incorporating sectional oblique fins, both channel width and fin width of a microchannel heat sink can be relaxed, allowing a much simpler, and economical, fabrication process.

On the other hand, Fig. 2.56 compares the total thermal resistances to the pump power requirement. In this context, pump power is computed as the product of volu-

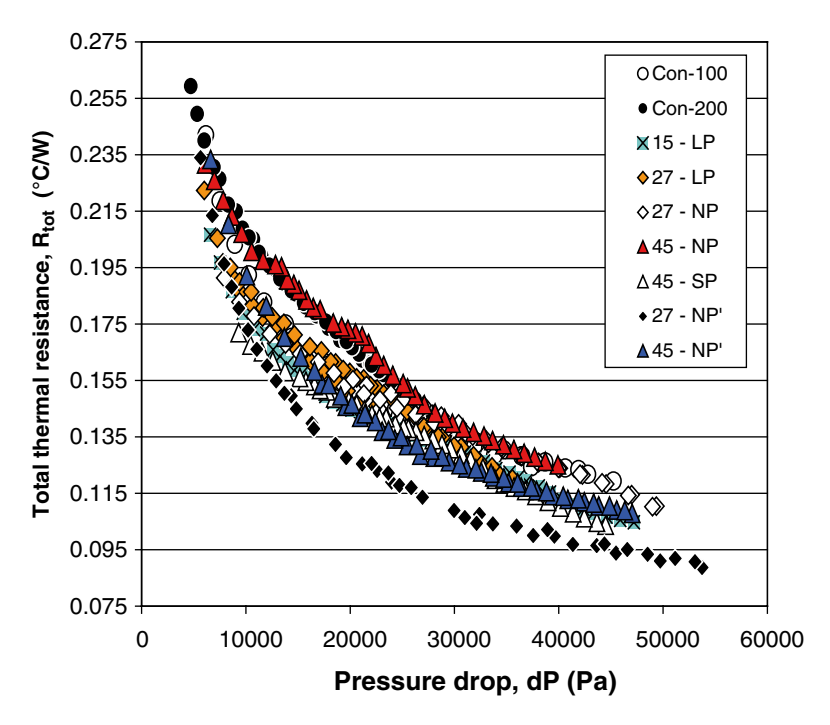


Fig. 2.55 Comparison of total thermal resistance to the pressure drop across microchannel heat sinks

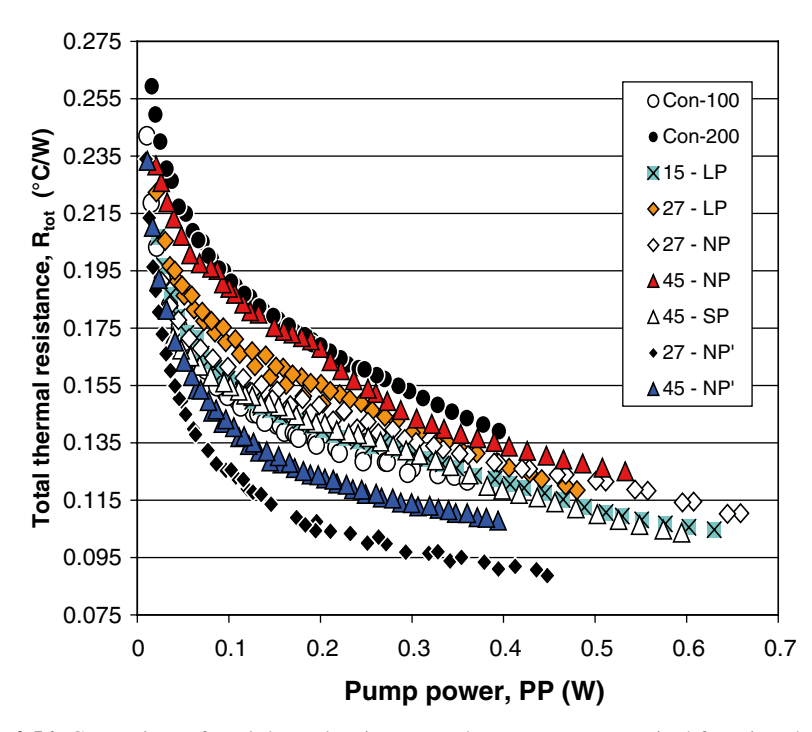


Fig. 2.56 Comparison of total thermal resistance to the pump power required for microchannel heat sinks

metric flow rate and pressure drop across the microchannel heat sink. Through this comparison, it is clear that enhanced microchannel heat sinks with 100 μ m nominal channel width dominate those with 200 μ m nominal channel width as the latter require much higher volumetric flow rate to achieve a comparable heat transfer performance. However, it is found that some enhanced microchannel heat sinks with 200 μ m nominal channel width, for instance, 45°—SP and 15°—LP, can perform as well as conventional microchannel heat sink with 100 μ m nominal channel width. This parametric study provides alternatives for the further performance improvement of larger size channel, should the fabrication present a constraint on the minimum channel size. In summary, the heat transfer of microchannel heat sinks can be ranked as follows under constant pressure drop or pump power constraint:

$$27^{\circ}$$
—NP'> 45° —NP'>Con-100, 45° —SP and 15° —LP> 27° —NP> 27° —LP> 45° —NP>Con-200

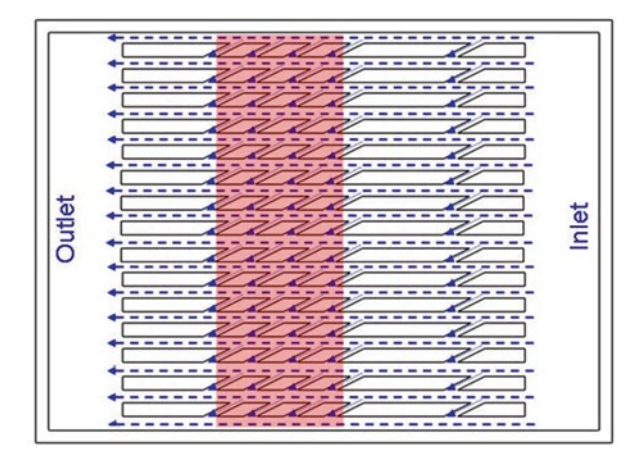
2.6 Hotspot Mitigation with Oblique Fin Microchannel Heat Sink

It has been demonstrated in the previous sections that enhanced microchannel with oblique fins can be employed to improve the heat transfer performance of microchannel heat sink under uniform heating conditions. However, it is desirable to propose a thermal management technique that can cater for highly non-uniform heat flux dissipation, which has become the trend of advanced electronics. This section examines the effect of selectively varying the oblique fin pitch in the microchannel heat sink. Numerical simulation shows that denser oblique fin cluster promotes higher occurrence of boundary layer redevelopment and secondary flow generation, resulting in local heat transfer enhancement, without the penalty of increased pressure drop. Subsequently, experimental investigation with two hotspot conditions is conducted to demonstrate and validate the feasibility of this concept.

2.6.1 Hotspot Mitigation Concept with Oblique Fins

There is an urgent requirement to introduce a new thermal management technique to cope with the hotspots on electronic devices, as the conventional cooling schemes, which are designed for uniform heat flux dissipation, are not effective in cooling hotspots [31]. Thus, this section explores the feasibility of adapting enhanced microchannel heat sink, with oblique fin, for electronic hotspot mitigation [32]. It would be interesting to examine the effect of selectively varying the oblique fin pitch based on the local heat flux level to control the occurrence of boundary layer redevelopment and secondary flow generation, which in turn tailor the required local heat transfer performance. This idea is inspired by Sui et al. [28], who proposed to vary the waviness of wavy channel based on local heat flux level to tailor the chaotic advection in the wavy channel.

Fig. 2.57 Plan view of variable pitch oblique finned microchannel heat sink with hotspot (red colour highlighted)



Shorter fin pitch leads to closely packed oblique fins and channels, where thermal boundary layer redevelopment and secondary flow generation would occur at higher frequency. Consequently, local heat transfer performance can be greatly enhanced. In contrast, longer fin pitch reduces the number of oblique fin, as well as the associated heat transfer enhancement. The combination of these features turns out to be ideal for hotspot thermal management, where denser oblique fin cluster provides effective heat removal for the extreme high heat flux, while sparser oblique fin cluster dissipates the background heat flux without overcooling the chip. A potential embodiment of variable pitch oblique finned microchannel heat sink is shown in Fig. 2.57. In addition, variable pitch oblique finned microchannel heat sink is expected to be effective especially for multiple hotspot configuration, where the denser fin clusters can be positioned directly on top of the hotspots without affecting the oblique fin characteristics in the neighbouring cluster.

2.6.2 Experimental Set-Up and Procedure

Two hotspot scenarios are considered in this experimental investigation; the first has a single hotspot at the centre of the thermal test chip, while the second has multiple hotspots over the entire chip. Three different heat sink designs, namely, conventional, constant pitch oblique finned and variable pitch oblique finned microchannel heat sink, are evaluated for their heat dissipating performance.

A similar experimental set-up that was employed in the study for enhanced microchannel heat sink with silicon thermal test chips in Sect. 2.4.1 is adopted for the investigation of electronic hotspot mitigation. An additional DC power supply and the associate current (power) measuring components (shunt resistor, voltage meter, etc.) are required to enable different level of heat supply into thermal test chip, to emulate the hotspot scenario. In these experiments, thermal test chips are supplied with two different heat fluxes: a background heat flux at the lower magnitude for most of the chip area and a significantly higher hotspot heat flux for small area of the chip area.

Two hotspot scenarios are considered in this experimental investigation; the first has a single hotspot at the centre of the thermal test chip, and the second has multiple hotspots over the entire chip. The same conventional microchannel and enhanced microchannel, with uniform fin pitch, are used for both experimental conditions. Separate enhanced microchannels with variable fin pitch are fabricated to tackle different hotspot conditions with local heat transfer performance tailoring. A cluster of oblique fins, with finer fin pitch, are placed on top of each hotspot with the intention of increasing both heat transfer area and cooling capability. The design for enhanced microchannel heat sinks with variable fin pitch is illustrated in Fig. 2.58a, b, where the red patches represent the location of the hotspot on the thermal test chip and the corresponding fin structure. Figure 2.59a, b shows the actual test vehicles of enhanced microchannel heat sinks with variable fin pitch.

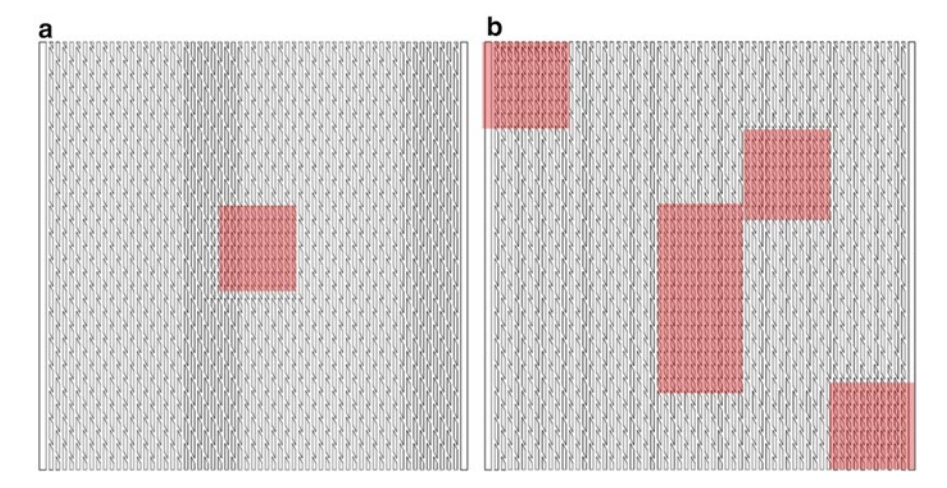


Fig. 2.58 Heat sink design for enhanced microchannel with variable fin pitch for (a) single hotspot condition and (b) multiple hotspot condition [32]

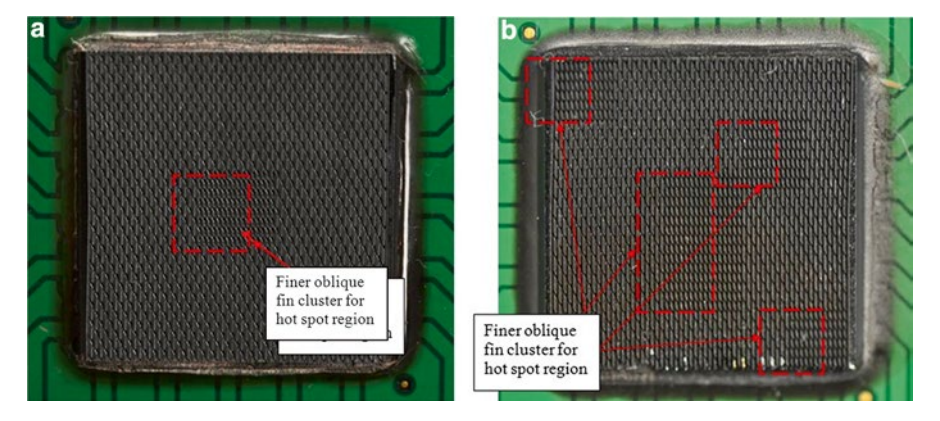


Fig. 2.59 Actual test vehicle for enhanced microchannel heat sink with variable fin pitch for (a) single hotspot and (b) multiple hotspots [32]

All the heat sinks are fabricated using laser machining, as the conventional fabrication methods such as wire cut and saw dicing are not able to produce oblique channel/fin at different pitch within a heat sink. Some important process parameters or settings for the laser machining are documented in Table 2.8.

The critical geometries are then measured with 3D profiler, and the data are tabulated in Table 2.9. Each characteristic is computed as an average value of 6 measurements across the heat sink. Furthermore, the fin channel profile in Fig. 2.60 shows that the channels are tapered at the bottom, as a result of the naturally pointed profile of a laser beam. Triangular channels are thus created instead of the rectangular channels achieved for the previous test vehicles. For a fair comparison, main channel width, fin width, oblique channel width, oblique channel angle and aspect ratio of different heat sinks are kept at a comparable range. The average roughness of the machined surfaces is measured at 0.91 μm .

Table 2.8 Process parameters for laser machining microchannel heat sinks

Characteristic	
Laser type	Nd: YAG
Laser power	150 μJ
Laser frequency	40 kHz
Wavelength	355 nm
Scanning lens	F-Theta
Travel speed	300 mm/s
Number of pass	40

Table 2.9 Dimensional details of test pieces used in the experiment [32]

	Conventional	Enhanced microchannel (uniform fin	Enhanced microchannel (variable fin pitch—single	Enhanced microchannel (variable fin pitch—multiple
Characteristic	microchannel	pitch)	hotspot)	hotspots)
Material	Silicon			
Footprint, width × length (mm ²)	12.7×12.7			
Number of fin row, N	61			
Main channel width, w_c (µm)	102	100	105	94
Fin width, w_w (μ m)	97	96	101	101
Channel depth, H (μm)	306	300	312	328
Aspect ratio, α	3.0	3.0	2.97	3.49
Oblique channel width, w_{ob} (μ m)	_	65	63	59
Fin pitch, p_L (μ m)	_	799	782	762
Fin length, l_L (μ m)	_	636	650	642
Fin pitch, p_s (μ m)	_	_	388	386
Fin length, l_s (μ m)	_	_	252	271
Oblique angel, θ (°)	_	26.7	26.8	27.4

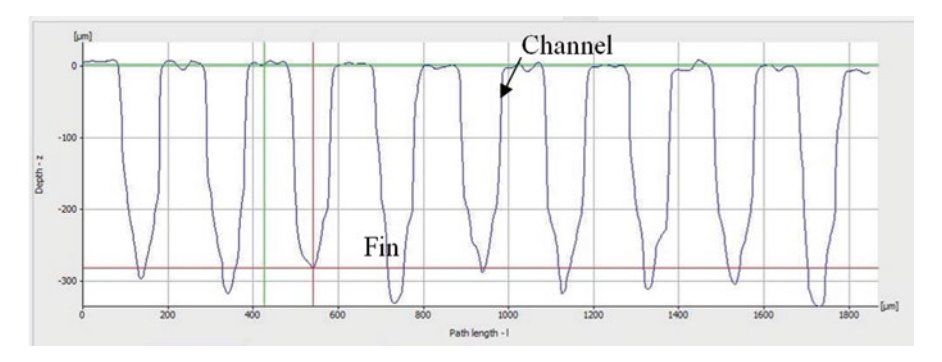


Fig. 2.60 Fin channel profile captured with 3D profiler [32]

A similar experimental procedure, as stated in Sect. 2.4.1, is adopted in this study. Total coolant flow rate across the heat sink is fixed at 200 mL/min for all the experimental runs, which corresponds to the Reynolds number of ~600. The background heat flux of the thermal test chip is set as 85 W/cm². On the other hand, hotspot heat flux for the single hotspot scenario is tuned to 400 W/cm², while that of the multiple hotspot scenario is at 300 W/cm².

The significant difference in the heat flux level between hotspots and remaining chip area would result in severe heat flux redistribution. 3D conduction occurs for the discrete heat fluxes applied at the bottom of chip towards the channel wall of the liquid passages. Unfortunately, local heat flux distribution at the channel wall is not measurable in the current experiment. Without this critical information, computation of local Nusselt number would be baseless. Due to this limitation, the discussion of the results is restricted to overall temperature contour, maximum temperature, temperature gradient and pressure drop across the heat sinks. Pressure drop across the microchannel heat sinks is reduced according to the method stated in Sect. 2.2.1.

2.6.3 Hotspot Scenarios

In this section, the experimental results of heat sink performance under single hotspot scenario are first discussed, followed by the findings of heat sink under multiple hotspot condition.

2.6.3.1 Single Hotspot Scenario

Comparisons between the maximum temperatures for the three heat sinks in Fig. 2.61 show that both enhanced microchannel heat sinks reduce the maximum chip temperature significantly. The maximum temperature of thermal test chip with conventional microchannel heat sink is at 77.6 °C, while that of the enhanced

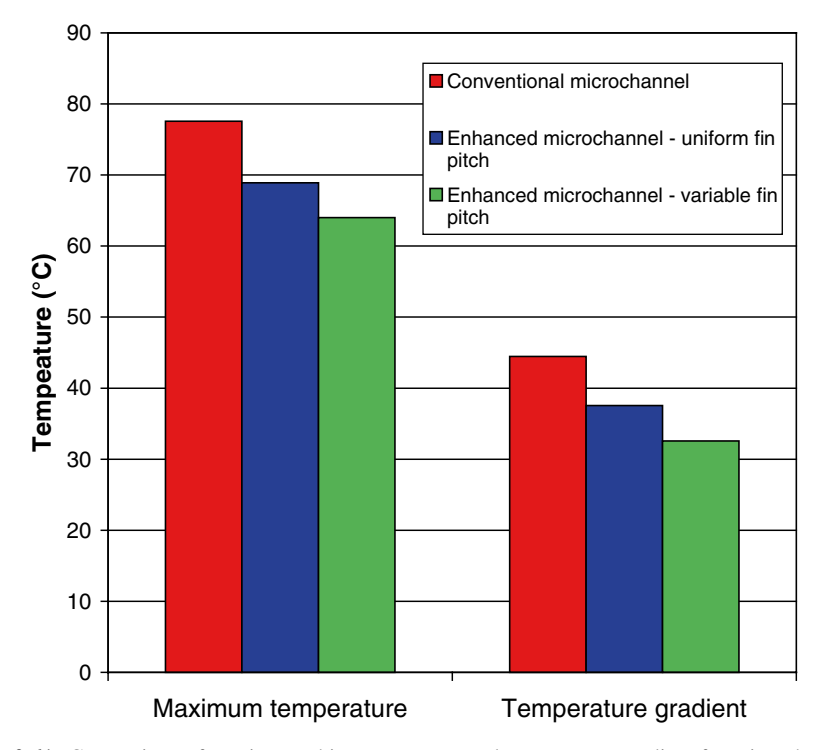


Fig. 2.61 Comparison of maximum chip temperature and temperature gradient for microchannel heat sinks [32]

microchannel with uniform fin pitch and variable fin pitch is reduced to 68.9 °C (8.7 °C reduction) and 64.0 °C (13.6 °C reduction), respectively. This shows that effective hotspot suppression can be achieved by employing sectional oblique fins. In the uniform oblique fin pitch configuration, the combined effect of thermal boundary layer redevelopment and secondary flow generation results in greater convective heat transfer performance, which lowers the chip temperature. On the other hand, variable oblique fin pitch configuration provides the opportunity to further improve the heat transfer performance locally on the hotspot. In addition to increasing the heat transfer area, clustering oblique fins with finer fin pitch leads to higher occurrence of thermal boundary layer redevelopment and secondary flow generation, which further elevates the heat transfer performance of the region. As a result, the maximum temperature of the hotspot is further lowered.

A similar trend is observed for the temperature gradient of thermal test chips. This is defined as the difference between local maximum and minimum temperature of the test chip, chip temperature gradient employing conventional microchannel heat sink, enhanced microchannel heat sink with uniform fin pitch and enhanced

microchannel heat sink with variable fin pitch, 44.5, 37.6 and 32.6 °C, respectively. The reduction in temperature gradient occurs as a result of significantly lower maximum chip temperature for the enhanced microchannel heat sinks. By achieving the lowest maximum chip temperature and temperature gradient among three cooling techniques, the enhanced microchannel heat sink with variable fin pitch demonstrates its capability as an effective solution in electronic hotspot mitigation by flexibly adapting to the heating condition.

Figure 2.62a–c illustrates the detailed chip temperature distribution for each silicon chip based on the temperature measured from all 25 temperature sensors (in 5×5 grid array) within the thermal test chip. Generally, hotspots with maximum temperatures occur at the centre of the thermal test chip, where the hotspot heat flux (400 W/cm^2) is significantly higher than the background heat flux (85 W/cm^2) . As discussed, conventional microchannel heat sink results in the highest hotspot temperature followed by enhanced microchannel with uniform fin pitch and enhanced microchannel with variable fin pitch. Beyond the hotspot, chip temperature is reduced but the region located downstream to the hotspot tends to have higher temperature compared to its surrounding at the same axial distance due to the larger sensible heat gain as coolant travels past the hotspot. In addition, it is noticed that the temperature contour is rather "squarish" in shape, possibly due to the limited 25 data points available in square grid array.

At a similar background heat flux at 85 W/cm², the enhanced microchannel heat sink with uniform fin pitch lowers the temperature of the entire chip by at least 5 °C compared with conventional microchannels. The heat transfer augmentation, brought forth by the oblique fins/channels, is uniform across the test chip. A temperature spike at the hotspot is also milder for enhanced microchannel, where the temperature difference between the hotspot and the surroundings is reduced. As for the enhanced microchannel with variable fin pitch, chip temperature for regions under the background heat flux is maintained at an almost identical value of the enhanced microchannel with uniform fin pitch, while the maximum temperature at the hotspot is further reduced leading to a much more uniform temperature contour. Such design not only suppresses electronic hotspot but also avoids the overcooling of remaining chip area, which is the critical criterion of a hotspot mitigation scheme [31]. If oblique fins with finer fin pitch are laid across the entire heat sink, it is highly possible that maximum hotspot temperature would remain the same while both temperature gradient and pressure drop across the heat sink will be increased.

Examining pressure drop across the microchannel heat sinks shows that pressure drop for conventional microchannel is the lowest among the threes. Although the pressure drop for both enhanced microchannel is higher, the difference is not significant. From Fig. 2.63, the pressure drop for both enhanced microchannel heat sinks is about 10–20 % higher than that of the conventional microchannel. This shows that by adopting an effective thermal management scheme, heat transfer performance can be augmented significantly, with affordable pressure drop penalty.

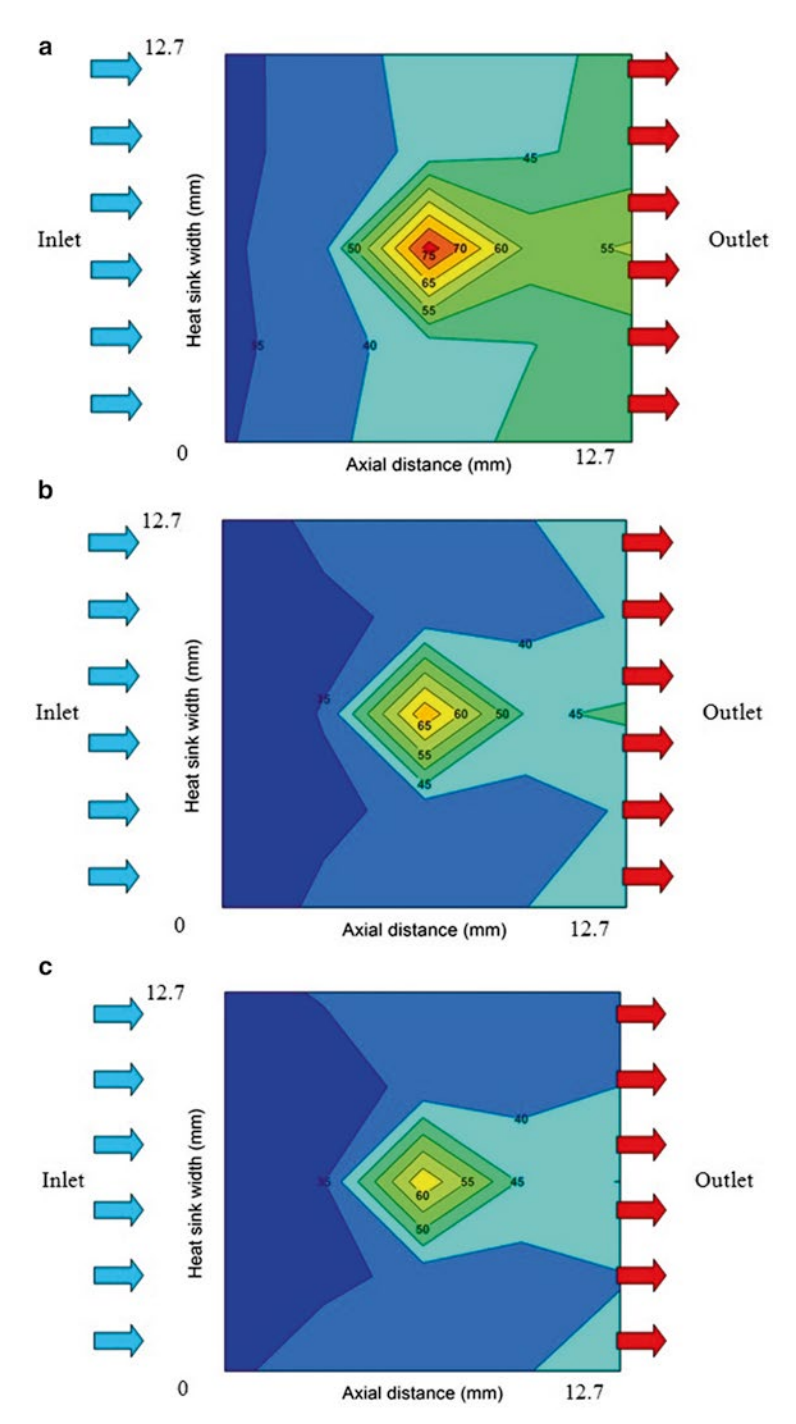


Fig. 2.62 Temperature distribution for single hotspot scenario for (a) conventional microchannel, (b) enhanced microchannel with uniform fin pitch, and (c) enhanced microchannel with variable fin pitch [32]

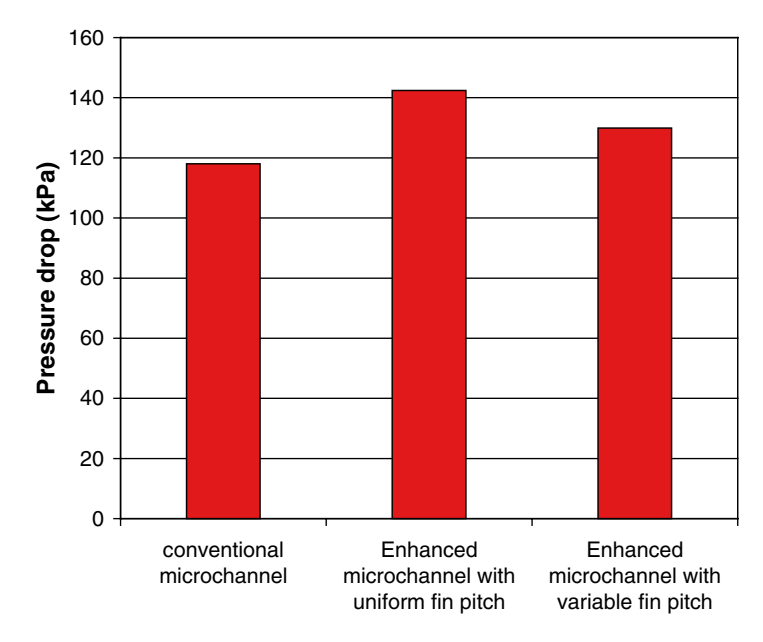


Fig. 2.63 Comparison of pressure drop across microchannel heat sinks [32]

2.6.3.2 Multiple Hotspot Scenario

A total of five hotspots, each dissipating 300 W/cm² heat flux, are emulated on the thermal test chip, with a background heat flux of 85 W/cm². The hotspots are positioned on the chip as illustrated in Fig. 2.59b, with two of hotspots placed adjacent to each other. As a result, the temperature contour of the thermal test chip becomes more complex compared to the single hotspot scenario. Figure 2.64a illustrates the temperature distribution of the chip with conventional microchannel heat sink under the multiple hotspot scenario. The occurrence of multiple hotspots in the chip changes the chip temperature contour completely. Despite showing a general trend of progressive temperature increment in the axial direction, temperature spike at each hotspot is clearly observed. The maximum hotspot temperature can be as high as 75 °C, and the temperature spike at the hotspots is generally 20–25 °C hotter than the surrounding area that is just a few millimetres away. Such a high temperature gradient within a short distance in electronic chip is highly undesirable as it exerts additional thermal stress to the chip. This situation seems unavoidable as multiple functional modules with different level of power consumption being packed within a small chip as the industry move towards "more-than-Moore" technologies [33].

Nevertheless, this condition can be improved by adopting the better thermal management scheme. Figure 2.64b illustrates the temperature distribution of the

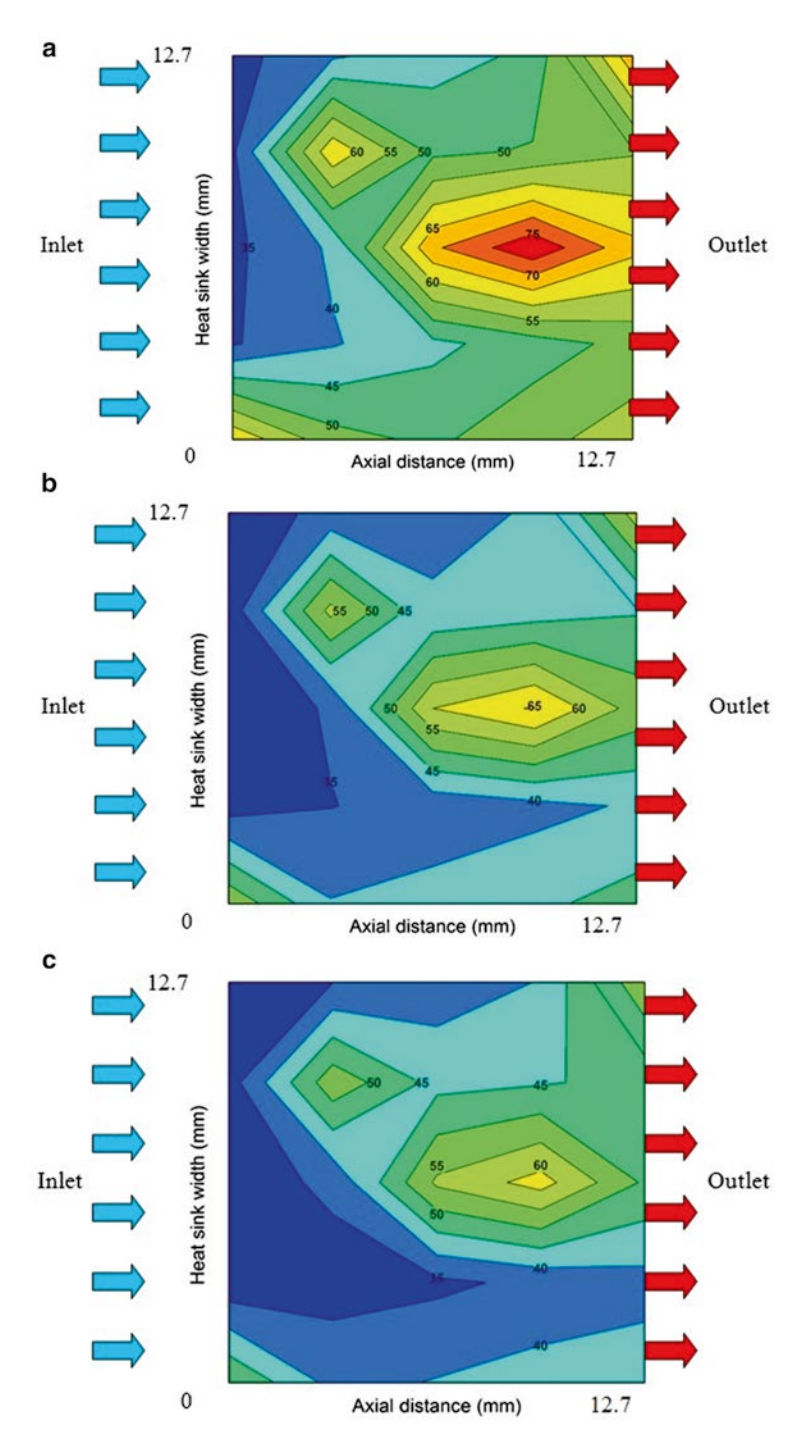


Fig. 2.64 Temperature distribution for multiple hotspot scenario for (a) conventional microchannel, (b) enhanced microchannel with uniform fin pitch, and (c) enhanced microchannel with variable fin pitch [32]

thermal test chip employing the obliquely finned microchannel heat sink with uniform fin pitch. Significant drop in temperature is observed across the entire chip, especially the hotspot region. A comparison between the temperature distributions for both heat sinks also shows that the enhanced microchannel heat sink is more effective in relieving the hotspot situation at the downstream of the heat sink. The magnitude of temperature reduction for hotspots at the upstream of the heat sink is ~5 °C, while that for the downstream of the heat sink can be larger than 10 °C. This can be attributed to the unique feature of the enhanced microchannel heat sink in maintaining a uniform heat transfer performance in the axial direction. While heat transfer performance deteriorates in the axial performance for a conventional microchannel, the enhanced microchannel exhibits the higher, yet uniform, heat transfer coefficient owing to the thermal boundary layer redevelopment and secondary flow generation that occur throughout the heat sink. This combined effect creates a constantly renewed flow field that is beneficial, especially for easing off the hotspots downstream of the heat sink.

Figure 2.64c, on the other hand, displays the temperature contour of a chip employing the enhanced microchannel heat sink with variable pitch. The temperatures are generally similar to that of the enhanced microchannel with uniform fin pitch except the hotspots, where the temperatures are further lowered. By adopting finer fin pitch for hotspots and coarser fin pitch for other regions with lower background heat flux, the heat sink performance can be tailored based on the heat flux level. Thus, the region with the higher heat flux dissipation will always have the higher heat removal capability and lower hotspot temperature, regardless of its location on the chip. As a result, a much more uniform temperature distribution can be created across the entire chip with this performance tailoring technique, rendering it as an effective thermal management scheme for electronics with hotspots.

For a hotspot mitigation scheme to be successful, the hotspot suppressing feature must be placed close to the hotspot. Thus, it is most effective if variable pitch oblique finned microchannel heat sink is integrated onto the silicon chip. A separate heat sink on a device with hotspots will see its advantage of local heat transfer performance tailoring be neutralized by the spreading and contact resistances.

The comparison for the maximum temperature and temperature gradient of the chips with different heat sinks is shown in Figure 2.65, which clearly demonstrates the reduction in maximum temperature and temperature gradient of the chip from conventional microchannel to enhanced microchannel with uniform fin pitch and variable fin pitch.

Figure 2.66 displays the pressure drop across the microchannel heat sinks for the multiple hotspot scenario where similar trend is observed compared with the single hotspot experimental condition. Conventional microchannel heat sink records the lowest pressure drop among the three, while that of the enhanced microchannel heat sinks are 10-20~% higher.

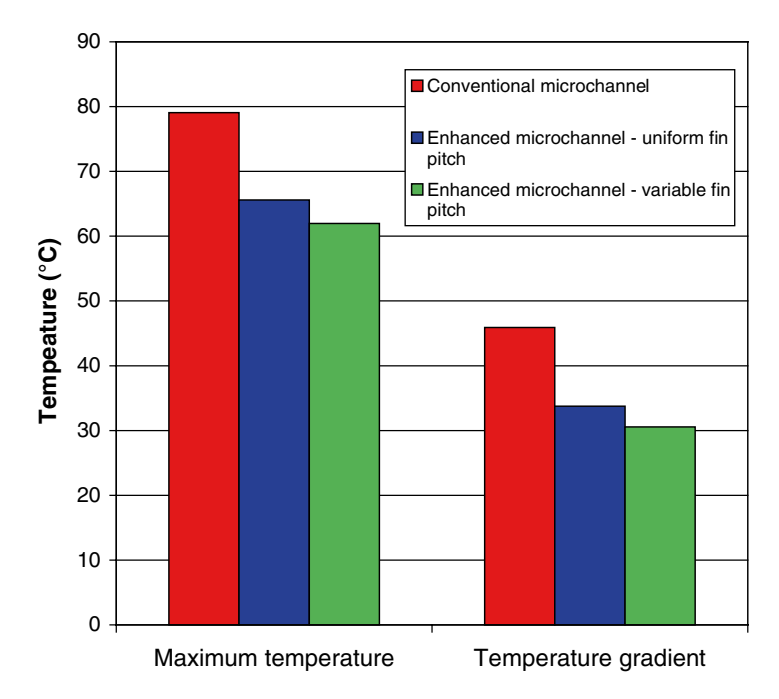


Fig. 2.65 Comparison of maximum chip temperature and temperature gradient for microchannel heat sinks [32]

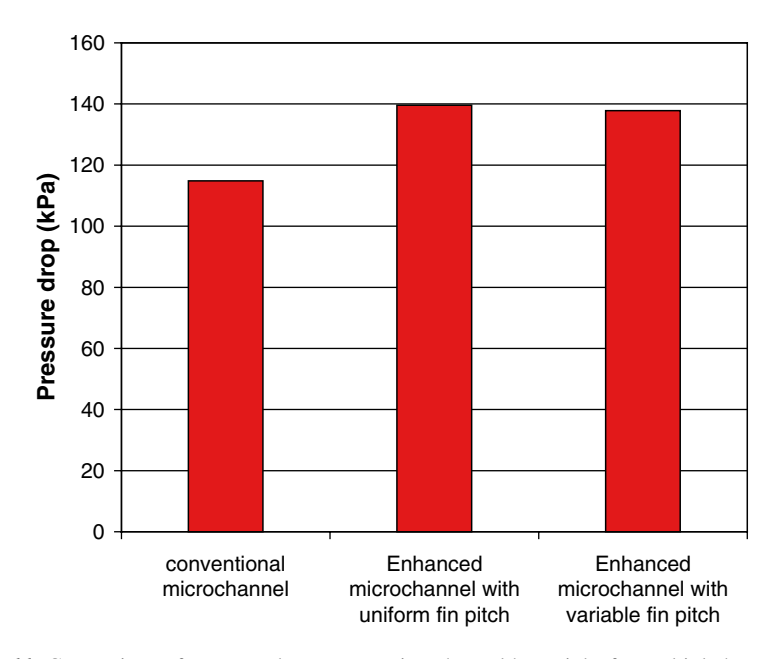


Fig. 2.66 Comparison of pressure drop across microchannel heat sinks for multiple hotspot scenario [32]

References

 Steinke ME, Kandlikar SG (2004) Single-phase heat transfer enhancement techniques in microchannel and minichannel flows. In: Proceedings of the ASME 2nd international conference on microchannels and minichannels (ICMM 2004), Rochester, New York, USA, paper no-2328, pp 141–148, 17–19 June 2004

- DeJong NC, Jacobi AM (2003) Localized flow and heat transfer interactions in louvered-fin arrays. Int J Heat Mass Transfer 46:443–455
- Lee YJ, Lee PS, Chou SK (2013) Numerical study of fluid flow and heat transfer in the enhanced microchannel with oblique fins. J Heat Transfer 135:041901. doi:10.1115/1.4023029
- Suga T, Aoki H (1991) Numerical study on heat transfer and pressure drop and pressure drop in multilouvered fins. In: Lloyd JR, Kurosake Y (eds) Proceedings of 1991 ASME/JSME joint thermal engineering conference, vol 4, ASME, New York, p 361–368
- Davenport CJ (1980) Heat transfer and fluid flow in the louvered-fin heat exchanger. Ph.D. Thesis, Department of mechanical Engineering, Lanchester Polytechnic, UK
- Aoki H, Shinagawa T, Suga K (1989) An experimental study of the local heat transfer characteristic in automotive louvered fins. Exp Therm Fluid Sci 2:293–300
- FLUENT 6.3 user's guide (2006) Chapter 7: cell zone and boundary conditions, FLUENT Inc., Lebanon, NH
- Li J, Peterson GP (2007) 3-Dimensional numerical optimization of silicon-based high performance parallel microchannel heat sink with liquid flow. Int J Heat Mass Tranfer 50:2895–2904. doi:10.1016/j.ijheatmasstransfer.2007.01.019, http://dx.doi.org
- Ryu JH, Choi DH, Kim SJ (2002) Numerical optimization of the thermal performance of a microchannel heat sink. Int J Heat Mass Tranfer 45:2823–2827. doi:10.1016/ S0017-9310(02)00006-6, http://dx.doi.org
- Lee P-S, Garimella SV (2006) Thermally developing flow and heat transfer in rectangular microchannels of different aspect ratios. Int J Heat Mass Transfer 49:3060–3067. doi:10.1016/j. ijheatmasstransfer.2006.02.011
- Incropera FP (1999) Liquid cooling of electronic devices by single-phase convection. Wiley, New York, NY, pp 262–263
- Lee P-S, Garimella SV, Liu D (2005) Investigation of heat transfer in rectangular microchannels. Int J Heat Mass Transfer 48:1688–1704. doi:10.1016/j.ijheatmasstransfer.2004.11.019
- 13. Douglas JF, Gasiorek JM, Swaffield JA, Jack LB (2005) Fluid mechanics, 5th edn. Pearson, Harlow, UK, p 389
- Alharbi AY, Pence DV, Cullion RN (2003) Fluid flow through microscale fractal-like branching channel networks. J Fluids Eng 125:1051–1057
- Senn SM, Poulikakos D (2004) Laminar mixing, heat transfer and pressure drop in tree-like microchannel nets and their application for thermal management in polymer electrolyte fuel cells. J Power Sources 130:178–191
- Chandratilleke TT, Jagannatha D, Narayanaswamy R (2010) Heat transfer enhancement in microchannels with cross-flow synthetic jets. Int J Therm Sci 49:504–513
- Sahnoun A, Webb RL (1992) Prediction for heat transfer and friction for the louver fin geometry. J Heat Transfer 114:893–900
- Xu JL, Gan YH, Zhang DC, Li XH (2005) Microscale heat transfer enhancement using thermal boundary layer redeveloping concept. Int J Heat Mass Transfer 48:1662–1674
- Xu JL, Song YX, Zhang W, Zhang H, Gan YH (2008) Numerical simulations of interrupted and conventional microchannel heat sinks. Int J Heat Mass Transfer 51:5906–5917
- 20. Kim SJ, Kim D, Oh HH (2008) Comparison of fluid flow and thermal characteristics of platefin and pin-fin heat sinks subjects to a parallel flow. Heat Transfer Eng 29:169–177
- 21. Lee YJ (2014) Fluid flow and heat transfer investigations on enhanced microchannel heat sink using oblique fins with parametric study. Int J Heat Mass Transfer (submitted)
- 22. Mou N (2014) Numerical investigations on fluid flow and heat transfer characteristic in oblique fin microchannel array. Int J Heat Mass Transfer (submitted)

- 23. Lee YJ, Lee PS, Chou SK (2012) Enhanced thermal transport in microchannel using oblique fins. J Heat Transfer 134:101901. doi:10.1115/1.4006843
- 24. Qu W (2004) Transport phenomena in single-phase and two-phase micro-channel heat sinks. Ph.D. Thesis, School of Mechanical Engineering, Purdue University, West Lafayette
- 25. Todreas NE, Kazimu MS (1990) Nuclear system I. Hemisphere, New York, NY
- Lyman AC, Stephan RA, Thole KA, Zhang LW, Memory SB (2002) Scaling of heat transfer coefficients along louvered fins. Exp Therm Fluid Sci 26:547–563
- Rosaguti NR, Fletcher DF, Haynes BS (2006) Laminar flow and heat transfer in a periodic serpentine channel with semi-circular cross-section. Int J Heat Mass Tranfer 49:2912–2923
- 28. Sui Y, Teo CJ, Lee PS, Chew YT, Shu C (2010) Fluid flow and heat transfer in wavy microchannels. Int J Heat Mass Tranfer 53:2760–2772
- Joshi HM, Webb RL (1987) Heat transfer and friction in the offset strip-fin heat exchanger. Int J Heat Mass Transfer 30:69–84
- Kandlikar SG, Colin S, Peles Y, Garimella S, Pease RF, Brandner JJ, Tuckerman DB (2013)
 Heat transfer in microchannels: 2012 status and research needs. J Heat Transfer 135:091001.
 doi:10.1115/1.4024354
- 31. Bar-Cohen A, Arik M, Ohadi M (2006) Direct liquid cooling of high flux micro and nano electronic components. Proc IEEE 94:1549–1570
- 32. Lee YJ, Lee PS, Chou SK (2013) Hotspot mitigating with obliquely finned microchannel heat sink: an experimental study. IEEE Trans Compon Packag Manuf Tech 3:1332–1341. doi:10.1109/TCPMT.2013.2244164
- Zhang GQ, Graef M, Roosmalen FV (2006) The rationale and paradigm of "More than Moore". In: Proceedings of 56th electronic components and technology conference, San Diego. CA, pp 151–157. DOI: 10.1109/ECTC.2006.1645639



http://www.springer.com/978-3-319-09646-9

Thermal Transport in Oblique Finned Micro/Minichannels Fan, Y.; Lee, P.S.; Singh, P.K.; Lee, Y.J. 2015, XIII, 130 p. 95 illus., 80 illus. in color., Softcover ISBN: 978-3-319-09646-9